ABSTRACT

Title of Dissertation: HUNTING INFLATIONARY FOSSILS IN PRIMORDIAL INHOMOGENEITIES

Arushi R Bodas
Doctor of Philosophy, 2023

Dissertation Directed by: Professor Raman Sundrum
Department of Physics

Cosmological observables such as the Cosmic Microwave Background (CMB) allow us to probe the early universe at extremely high energies far beyond the reach of any particle collider on Earth. In the inflationary paradigm, small perturbations in the energy distribution across space can be directly linked to the quantum fluctuations of an "inflaton" field that drives inflation. Using these perturbations, it is, therefore, possible to learn about physics at energies as high as 10^{13} GeV. In this thesis, we exploit this powerful connection and explore novel mechanisms to hunt for previously unexplored inflationary dynamics.

During inflation, particles with masses larger than the inflationary Hubble scale $H_{\rm inf}$ are produced due to an accelerating spacetime. If coupled to the inflaton, these particles could imprint distinct oscillatory features in higher moments of the density perturbations. Since $H_{\rm inf}$ can be as high as 5×10^{13} GeV, these oscillatory features present a unique opportunity to directly detect very heavy particles with masses $\sim H_{\rm inf}$. In Chapter 2, we explore a mechanism that can boost spin-0 particle production by mining the kinetic energy of the inflaton. This leads to an enhancement

of the oscillatory features, which can bring heavier particles with masses up to $60H_{\rm inf}$ within the reach of observations.

In the final part of the thesis, spanning chapters 3 and 4, we explore the viability of gravitational wave backgrounds (GWB) as novel data sources for unexplored inflationary physics. It was recently shown that a GWB from a first-order phase transition must exhibit fluctuations, much like the CMB. Despite the close analogy, it is possible for fluctuations of the GWB to differ significantly in their detailed pattern from those of the CMB, which would imply the existence of a second light field during inflation in addition to the inflaton. Such a GWB could thus unlock a wealth of new information about multi-field inflation. In Chapter 3, we elaborate on this point with an example. We show that there may exist signals that cannot be extracted using standard cosmological probes such as the CMB and galaxy surveys, but can in principle be detected within GWB with upcoming and proposed gravitational wave experiments. Lastly, in Chapter 4, we focus on the detectability of GWB itself. We discuss a cosmological mechanism that can enhance the strength of the gravitational wave signal from phase transitions, thereby increasing their detection prospects significantly.

Hunting Inflationary Fossils in Primordial Inhomogeneities

by

Arushi R. Bodas

Dissertation submitted to the Faculty of the Graduate School of the
University of Maryland, College Park in partial fulfillment
of the requirements for the degree of
Doctor of Philosophy
2023

Advisory Committee:
Professor Raman Sundrum, Chair/Advisor
Professor Zackaria Chacko
Professor Anson Hook
Professor Peter Shawhan
Professor Richard Wentworth

© Copyright by
Arushi R. Bodas
2023

Dedication

To my Aai, Neha Bodas.

Acknowledgments

First of all, I thank my advisor Raman Sundrum. It has truly been a joy to work with him and to discover the beauty of physics through our countless hours of discussion. From him I have learned a sense of aesthetics grounded by pragmatism that has made me a better researcher and will continue to guide me throughout my career.

Next I would like to thank all of my collaborators at UMD and beyond. I thank Soubhik Kumar, Manuel Buen-Abad, Anson Hook, Edward Broadberry, Rupert Coy, and Simon King. It has been a pleasure working with you all, and I hope to continue collaborating with you!

The UMD ecosystem, and specifically MCFP, are special places that will always feel like home to me. The support of all the people here has made my PhD a very happy and rewarding experience. I would like to thank faculty members Zackaria Chacko, Kaustubh Agashe, Rabindra Mohapatra, and Ted Jacobson, as well as postdocs Gustavo Marques-Tavares, Jae Hyeok Chang, Lorenzo Ricci, Yuhsin Tsai, and Zhen Liu. I want to thank Peter Shawhan and Richard Wentworth for being on my thesis committee and taking the time to review my dissertation. Last but not least, I would like to thank the MCFP and Physics administrators Melanie Knouse, Heather Markle, Josiland Chambers and Donna Hammer who made my PhD go smoothly.

I have had a lot of fun learning and discussing physics with my fellow graduate students at UMD. I thank Majid, Peizhi, Abhish, Kaustubh, Saurav, Deepak, Batoul, Alireza, Reza, Stefano, Dawid, Clayton, Sanket, Sagar, and Saurabh. This list would not be complete if I did not

include conversation buddies at physics parties, Wade, Artur, Landry, Gautam, Spandan, Keshav, Liz, Tristan, Reuben, and Sergio. Grad school has been a time of growth not just professionally but also personally. Sharing in my journey were my amazing housemates, Sohitri, Arghya, Anshuman, Ketki, Yogesh, Saikanth, Julia, Yingue, and Joy.

I want to thank some very special friends with whom I have spent many an evening chatting, playing board games, and feasting on home-cooked meals that only got better over the years. I thank Naren, Navya, Xiaozhen, Prakhar, Subhayan, Papia, Jaideep, Sasha, and Kaustubh. I love you all and will forever cherish the fun times we had!

My journey began well before 2017 and there are some important people who supported me through the years. I give special thanks to Sourabh Dube and Arijit Bhattacharyay, my mentors from IISER Pune. Of course, I cannot forget about my beautiful besties from school and IISER with whom I have shared all my joys and sorrows. Pooja, Leena, Indrayani, Shruti, Prajakta, Divya, and Mithila, you are the best!

My family has stood by my side every minute of the way. I thank my brother Saurabh, whose fighting spirit and positive attitude I have always admired. I thank Baba for teaching me how to be carefree and lighthearted when life gets tough. Aditi, with her curious mind, adventurous spirit, and decidedly rebellious streak, has rubbed off on me just a little and saved me from being too boring! My gratitude towards my Aai cannot be written in a few lines. Everything I am is because of her. And there's the matter of my goofball Aniruddha. You have brought into my life so much love, joy, humour, adventure, ... the list goes on. I cannot imagine my life without you.

Lastly, I would like to thank National Science Foundation for supporting the work done in this thesis through grants PHY-1914731 and PHY-2210361.

Table of Contents

Dedication ii

Acknowledgements iii

Table of Contents v

List of Tables vii

List of Figures viii

Citations to Previously Published Work xi

Chapter 1: Introduction 1
- 1.1 Background . . . 1
  - 1.1.1 Cosmic Inflation . . . 1
  - 1.1.2 Primordial fluctuations . . . 6
- 1.2 Primordial non-Gaussianity and signatures of heavy fields . . . 10
- 1.3 In pursuit of new maps: Gravitational Wave Backgrounds . . . 13
  - 1.3.1 Motivation for new maps . . . 13
  - 1.3.2 Cosmological gravitational wave backgrounds . . . 14

Chapter 2: The Scalar Chemical Potential in Cosmological Collider Physics 16
- 2.1 Introduction . . . 16
- 2.2 Preliminaries . . . 24
- 2.3 A minimal model . . . 27
  - 2.3.1 Chemical potential for a complex scalar with U(1) symmetry breaking . . . 27
  - 2.3.2 Realizing a chemical potential via inflaton couplings . . . 29
  - 2.3.3 Analysis of the spatially homogeneous background of the complex scalar 30
  - 2.3.4 Quantization and mode functions of the complex scalar . . . 34
  - 2.3.5 Interactions of the complex scalar with the inflaton . . . 38
- 2.4 Approximate calculation of the bispectrum in the squeezed limit . . . 39
  - 2.4.1 Dominant contribution: I_{+-} diagrams . . . 42
  - 2.4.2 Constraints . . . 48
  - 2.4.3 Central results . . . 49
  - 2.4.4 Sub-dominant contribution: I_{++} diagrams . . . 54
  - 2.4.5 Symmetry breaking mass term . . . 56
- 2.5 Inferring effective mass from the bispectrum . . . 61

2.6 Conclusions . . . 64

Chapter 3: Primordial Clocks within Gravitational Wave Anisotropies 66
3.1 Introduction . . . 66
3.2 Primordial clocks in single-field inflation . . . 69
3.3 Primordial clocks in gravitational waves with isocurvature . . . 73
3.3.1 A simple model of isocurvature GWB . . . 74
3.4 Observational aspects of primordial clocks in gravitational waves . . . 77
3.4.1 Benchmarks . . . 80
3.4.2 Broader analysis of the parameter space . . . 84
3.5 Primordial clocks from a polynomial potential . . . 86
3.6 Conclusion . . . 89

Chapter 4: Large Primordial Fluctuations in Gravitational Waves from Phase Transitions 91
4.1 Introduction . . . 91
4.2 Recap: isocurvature GWB in the radiation-dominated model . . . 94
4.2.1 Strength of GWB and its anisotropies . . . 96
4.3 Isocurvature GWB with an era of early matter dominance (eMD) . . . 99
4.3.1 Strength of GW and anisotropies . . . 101
4.3.2 Peak frequency of GWB . . . 103
4.4 Gravitational crosstalk . . . 104
4.4.1 Modes that are superhorizon prior to $t_{\rm dec}$ . . . 104
4.4.2 Modes that have re-entered the horizon prior to $t_{\rm dec}$ . . . 107
4.5 Benchmarks and Observability . . . 121
4.6 Discussion . . . 125

Chapter 5: Conclusion 127
5.1 Summary and future directions . . . 127
5.2 Final remarks . . . 128

Appendix A: Appendices to Chapter 2 130
A.1 Important integrals involving Hankel functions . . . 130
A.2 Full calculation of the bispectrum . . . 133
A.2.1 Full analytic calculation of $I_{+-/-+}$ diagrams . . . 133
A.2.2 Full analytic calculation of $I_{++/--}$ diagrams . . . 135

Appendix B: Appendix to Chapter 4 137
B.1 $f_{\rm PT}^2$ suppression in $\Omega_{\rm GW}$ in the radiation-dominated model . . . 137

Bibliography 142

List of Tables

4.1 Benchmarks showing the strength of GWB and its inhomogeneities in the pure radiation-dominance model of [1] and our eMD model. We take them to saturate the CMB bound in Eq. (4.5) (that is, $\zeta_\chi f_{\rm PT} = 4.5 \times 10^{-5}$). For a scale-invariant spectrum, they are consistent with the constraints from PBH production discussed in section 4.4.2.2, except for benchmark 4, which would require significantly red-tilted spectrum for χ to evade constraints on small scales (high-k). 122

List of Figures

1.1 A schematic showing the evolution of comoving horizon, which decreases during inflation and increases after the end of inflation taken to be at $\eta \approx 0$. We can see that the comoving length scales that were causally connected in the beginning become disconnected during inflation. They come into causal contact again only when the horizon has increased sufficiently. 4

1.2 A schematic showing the slow roll potential of the inflaton, its fluctuations, and the reheating at the end of inflation. 5

1.3 An example of a Feynman diagram in the in-in formalism, where the interaction is mediated by the exchange of a heavy particle. 10

2.1 Representation of the dominant tree-level contributions from I_{+-} and I_{++} diagrams to the bispectrum. For the convenience of notation, the time ordered part of the diagram is shown below the $\eta \approx 0$ line with time running upwards, while the anti-time ordered part is shown above with time running downwards. An incoming (outgoing) arrow at a vertex denotes injection (extraction) of energy. This makes it plausible that the I_{+-} contribution is enhanced compared to the I_{++} contribution, since for the former the "resonant" particle production through energy injection is efficient at *both* the vertices. Further explanations can be found in the text. 43

2.2 Comparison of $|f_{\rm oscil}|$ as a function of $M_{\rm eff}$ using stationary phase (dashed) and the full analytic form (solid) for two different values of the chemical potential $\lambda = 20H_{\rm inf}$ (yellow) and $\lambda = 40H_{\rm inf}$ (green), at $c = 0.5$ for $\alpha/\Lambda = 0.1\lambda$. The parametric dependence matches for $\mu < \lambda$ as expected with a difference of an $\mathcal{O}(1)$ factor. This mismatch can be attributed to contributions from other vertices which we did not consider in the stationary phase approximation above just for simplicity. Note the full calculation also smooths out the naive divergence in the stationary phase estimate as $\mu \approx \lambda$ since for such μ the approximation made in our stationary phase estimate breaks down. 51

2.3 Amplitude of the non-analytic contribution $|f_{\rm oscil}|$ from the full calculation in Appendix A.2, plotted against the physical mass $M_{\rm eff}$ of the complex scalar in Hubble units for $c = 0.5$ and various values of the chemical potential $\lambda = 10H_{\rm inf}$ (blue), $20H_{\rm inf}$ (yellow), $40H_{\rm inf}$ (green), and $60H_{\rm inf}$ (red). We take $\alpha/\Lambda = 0.1\lambda$. The expression for NG has a subdominant dependence on the parameter c, and hence we only show a representative plot for a generic value $c = 0.5$. Note that the range $0 < M_{\rm eff} \lesssim \lambda$ corresponds to $-\lambda^2/2 < M^2 \lesssim \lambda^2/2$ for the "bare" mass. The tachyonic regime for M (as opposed to $M_{\rm eff}$), $M^2 < 0$, corresponds to a post-inflationary instability to generating a significant σ background. During inflation, this instability is absent in the regime of non-tachyonic de Sitter mass $M_{\rm eff}$ plotted. No fine-tuning of parameters is needed to obtain the large signals shown. 53
2.4 The oscillatory signal as a function of the momentum ratio k_1/k_3 for $M = 5H_{\rm inf}$ and $\lambda = 40H_{\rm inf}$. The two different curves correspond to $c = 0.5$ or $M_{\rm eff} \simeq 28.7H_{\rm inf}$ (purple) and $c = 1$ or $M_{\rm eff} = 5H_{\rm inf}$ (blue). 54
2.5 Loop-level contribution to the bispectrum from $m^2\tilde{\sigma}^2$-type symmetry breaking. The solid lines correspond to inflaton propagators, while dashed lines to complex scalar propagators. 60
2.6 Comparison of the full analytic form evaluated in Appendix A.2 (blue) to the large λ approximation (yellow) and large p approximation (green) for $M_{\rm eff} = 5H_{\rm inf}$ and $\lambda = 40H_{\rm inf}$, using (a) the oscillatory form of the dimensionless NG function F and (b) the non-analytic exponent E. We clearly see that as the degree of squeezing is changed the full bispectrum switches between the above two approximations. 63

3.1 A schematic of the model with modified post-inflationary history showing energy densities in various sectors as a function of the scale factor (time). 74
3.2 Primordial spectrum $C_\ell^{\rm GW}$ with the PC feature using two sets of benchmark parameters from section 3.4.1. Figures (a) and (b) correspond to benchmark (1) with $\tilde{\alpha} = 0.31$, $M = 10H_{\rm inf}$, $\ell_d = 100$, while figures (c) and (d) correspond to benchmark (2) with $\tilde{\alpha} = 0.31$, $M = 5H_{\rm inf}$, $\ell_d = 20$. The yellow line shows the expected signal and the green dots incorporate a realization of cosmic variance. Figures (a) and (c) show unbinned GW power spectra, while figures (b) and (d) show corresponding binned values with $\Delta\ell = 6$ and $\Delta\ell = 7$, respectively. 81
3.3 Analysis of the $\alpha - M$ parameter space showing excluded regions from following considerations: binned cosmic variance (blue), CMB constraints from contribution to $\Delta\mathcal{P}_\gamma$ (yellow) and $f_{\rm NL}$ (green). The dashed lines show contours of PC signal strength $\delta\Omega_{\rm GW}^{PC}h^2(\ell_d)$ as given in Eq. (3.23) such that the parameter regions above these lines can be probed with corresponding experimental sensitivities. The analysis is carried out for (a) $\ell_d = 100$, as in the benchmark (1), and (b) $\ell_d = 20$, as in benchamark (2). See the text for more details. 85
3.4 The classical dynamics of σ field after the tachyonic transition at t_0 (blue) and the minimum $M_\sigma(t)/\sqrt{2\lambda}$ (yellow). The full dynamics shows oscillations about the minimum. 88

3.5 The PC feature in $\mathcal{P}_{\mathcal{S}_\chi}$ in the model with polynomial potential. The blue dots correspond to the numerical evaluation of $\Delta\mathcal{P}_{\mathcal{S}_\chi}$, where the overall shift is the result of $\langle\,\sigma\,\rangle \neq 0$. For reference, the yellow dashed line shows a matching signal from a simplified scenario where σ is instead excited suddenly, resulting in a PC with constant amplitude $\alpha \approx 0.125$ and mass $M \approx 14.8 H_{\rm inf}$. 89

4.1 A schematic of the modified eMD model discussed in section 4.3 showing energy densities in various sectors as a function of the scale factor (time). While the decay products of the ALP χ are always radiation dominated, one of the massive particles (reheaton) in the decay products of the inflaton leads to a period of early matter domination. 99

4.2 $\Phi(k)$ as a function of the conformal time η for a co-moving mode k that re-enters sufficiently after the end of eMD. We have taken a benchmark, $\zeta_\chi \approx 10^{-3}$, $\zeta_\phi \approx 3.5\times10^{-5}$, $f_{\rm PT} \approx 10^{-2}$, and $\epsilon = 1/2$. Conformal times denoting boundaries of different eras are $(\eta_{\rm m}/\eta_{\chi{\rm reh}}) \sim (\eta_{\rm md}/\eta_{\chi{\rm reh}}) \sim 100$ and $(\eta_{\rm dec}/\eta_{\chi{\rm reh}}) \sim 2000$. . . 105

4.3 (a) Fraction of DM energy density in PBH per logarithmic interval as a function of PBH mass in units of solar mass $M_\odot$. (b) Relevant constraints on monochromatic PBH mass functions from CMB distortions and microlensing (taken from [2, 3]). In (a), we show PBH mass distributions for two benchmarks in our eMD model: $\zeta_\chi \approx 5\times10^{-3}$, $f_{\rm PT} \approx 9\times10^{-3}$, $T_{\rm SM}(t_{\rm dec}) = 100$ GeV in purple, and $\zeta_\chi \approx 10^{-2}$, $f_{\rm PT} \approx 4.5\times10^{-3}$, $T_{\rm SM}(t_{\rm dec}) = 300$ GeV in orange. Noting the roughly monochromatic shape of these distributions, we have also shown their monochromatic best fits in (b) for an intuitive comparison with the constraints. . . 116

4.4 Strength of the GWB from phase transition (orange) occurring at $T_{\rm PT}(t_{\rm PT}) \sim 100$ TeV and that induced from curvature perturbations at second order (brown), compared with the power-law integrated sensitivities of LISA, BBO, and DECIGO (taken from [4]). The GWBs are computed for the benchmark that saturates PBH constraint (see discussion in section 4.4.2.2) with $\zeta_\chi = 10^{-2}$, $f_{\rm PT} = 4.5\times10^{-3}$, and $T_{\rm SM}(t_{\rm dec}) = 300$ GeV. 119

4.5 Comparison of benchmarks 1 (red), 3 (orange), and 4 (yellow) from table. 4.1 with the (a) sensitivities of upcoming space-based experiments like LISA, BBO, and DECIGO, and (b) noise power spectra N_ℓ as computed in [5]. Solid lines correspond to our modified eMD model while the dotted lines correspond the radiation-dominance scenario of [1]. In (a), the GWB spectra are evaluated for a phase transition occurring at $T_{\rm PT}(t_{\rm PT}) \sim 100$ TeV in a single-sector scenario, and contribution from bubble collisions is taken to be the dominant source of gravitational waves. In (b), all benchmarks for the eMD model lie on the same line at $\approx 5\times10^{-25}$ and are together represented by a black line. 126

Citations to previously published work

Much of this dissertation appeared in papers already published. Here we outline those publications.

- Chapter 2: "The Scalar Chemical Potential in Cosmological Collider Physics", A. Bodas, S. Kumar and R. Sundrum, JHEP 02, 079 (2021)

- Chapter 3: "Primordial clocks within stochastic gravitational wave anisotropies", A. Bodas and R. Sundrum, JCAP 10, 012 (2022)

- Chapter 4: "Large primordial fluctuations in gravitational waves from phase transitions", A. Bodas and R. Sundrum, JHEP 06, 029 (2023)

Chapter 1: Introduction

1.1 Background

The energy reach of the largest particle collider on Earth is $\sim 10^4$ GeV, which is modest compared to the highest energy scale in particle physics, the Planck scale ($\sim 10^{19}$ GeV). The early universe, however, is host to a rich tapestry of highly energetic processes, whose imprints can be found even today in observables such as the Cosmic Microwave Background (CMB) and galaxy surveys. For instance, during inflation, which is the earliest era of our universe, the typical energy scale could have been as high as 10^{13} GeV. If we could decode the imprints of inflationary physics in the cosmological observables of today, it would allow us to surpass our terrestrial limitations and access particle physics at these ultrahigh energies. Motivated by these exciting prospects, this thesis explores novel ways to probe the physics of inflation.

1.1.1 Cosmic Inflation

Our universe is very homogeneous and isotropic on large scales. This is evident in the temperature distribution of the CMB, which is uniform across the sky to approximately one part in 10^5. But a closer look reveals a problem with this uniformity. Due to the finite speed of light, faraway regions have been causally disconnected from each other from the Big Bang to

the time of the release of CMB photons that we are seeing today. These initially isolated regions should have started with very different initial conditions and thus evolved to look very different. The fact that the temperatures of CMB photons coming from these isolated regions are not $O(1)$ different, but similar at the level of 10^{-5}, therefore suggests the existence of a causal mechanism that enforces this uniformity. This puzzle can be solved by postulating the existence of an era that modifies Big Bang cosmology, and in which space expanded so rapidly that initially causally connected regions became disconnected by the end. In other words, the cosmic horizon shrank during this era instead of increasing. Therefore, despite these regions evolving independently afterwards, this initial causal contact explains their similarity at the time when the CMB photons that we're now seeing were emitted. Due to the rapid expansion of space, this era is aptly named "cosmic inflation".

Below, we briefly review the simplest realization of inflation. A more comprehensive review can be found in Ref. [6]. In $3+1$ dimensions, homogeneous and isotropic space-times can be uniquely described by the Friedmann–Lemaître–Robertson–Walker metric

$$ds^2 = -dt^2 + a(t)^2 d\vec{x}^2 = a(t(\eta))^2(-d\eta^2 + d\vec{x}^2). \tag{1.1}$$

We have adopted the metric signature $(-,+,+,+)$. The scale factor $a(t)$ tracks the relative size of space-like hypersurfaces at different times. The Hubble parameter captures the rate of expansion and also gives the typical time scale during that era. It is defined as

$$H \equiv \frac{\dot{a}}{a}, \tag{1.2}$$

where the overdot denotes derivative with respect to proper time t. As the proper distance in expanding space keeps changing, it is more natural to use comoving coordinates $\vec{x}$ in which the comoving distance between two points moving only under Hubble expansion remains constant. Translation invariance is manifest in these coordinates and the conjugate (comoving) momenta k are conserved. In the last expression in Eq. (1.1), we have switched to the conformal coordinates, which will be useful in many of the calculations in this thesis. The differential of the conformal time $d\eta$ is defined as a simple rescaling of dt,

$$d\eta = \frac{dt}{a(t)}\,, \tag{1.3}$$

such that the null geodesics of light are at 45^0 in $\eta - |x|$ plane. Therefore, the comoving distance travelled by any particle $|dx| < d\eta$, meaning η captures the comoving horizon.

Inflation can be well approximated by a de Sitter (dS) spacetime. It is a homogeneous and isotropic solution to Einstein's equation dominated by a positive cosmological constant Λ_c. The Hubble parameter $H \sim \Lambda_c$ is constant during dS phase and the scale factor increases exponentially as

$$a(t) = e^{Ht}. \tag{1.4}$$

The conformal time can be expressed via integration of Eq. (1.3) as

$$\eta = -\frac{1}{aH}, \tag{1.5}$$

where we have fixed the boundary condition $\eta \to 0$ as $t \to \infty$ in the dS phase. Notice that the

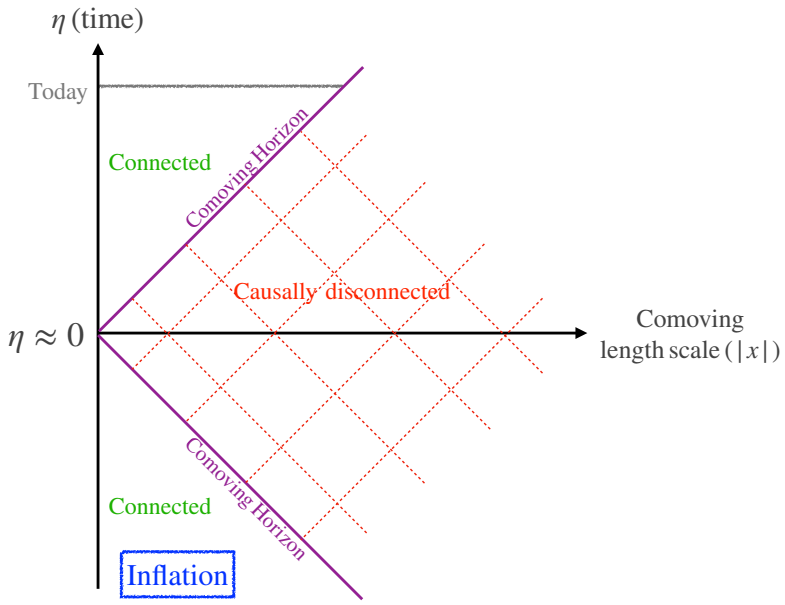

Figure 1.1: A schematic showing the evolution of comoving horizon, which decreases during inflation and increases after the end of inflation taken to be at $\eta \approx 0$. We can see that the comoving length scales that were causally connected in the beginning become disconnected during inflation. They come into causal contact again only when the horizon has increased sufficiently.

cosmic horizon at any time in dS phase is given by $\eta(t \to \infty) - \eta(t) = |\eta(t)|$. From Eq. (1.5), we can see that the cosmic horizon *decreases* as time (or $a(t)$) increases. The shrinking cosmic horizon is precisely the condition we needed for inflation. The evolution of the horizon throughout its cosmic history is shown in figure 1.1. We can see that the regions that are disconnected post-inflation were in fact causally connected at the beginning of inflation.

Now we need a model that starts with an inflationary phase and later transitions to the known cosmology of the post-Big-Bang universe. The most elegant formulation utilizes the classical dynamics of a scalar field called the inflaton ϕ. During inflation, we assume the energy density of the homogeneous inflaton background $\phi_0(t)$ to dominate the total energy density of the universe. The coupled equations for ϕ_0 dynamics and the inflationary Hubble parameter $H_{\rm inf}$

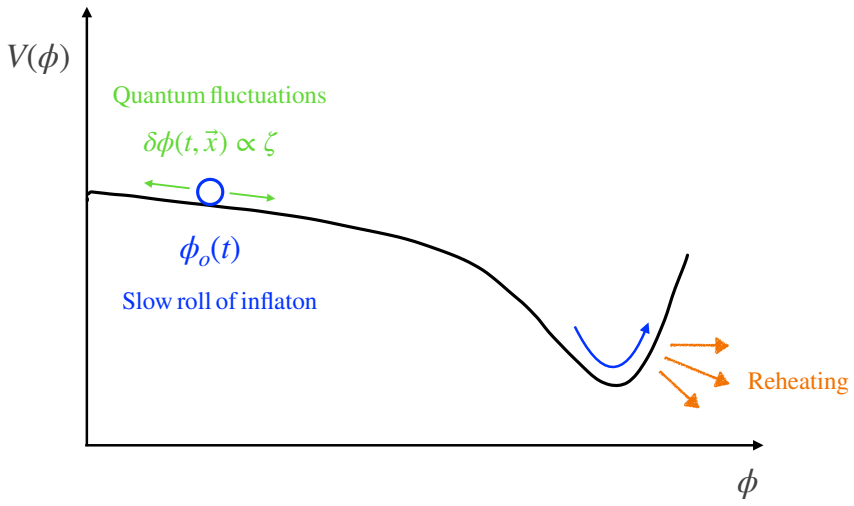

Figure 1.2: A schematic showing the slow roll potential of the inflaton, its fluctuations, and the reheating at the end of inflation.

are then given by

$$\ddot{\phi}_0 + 3H_{\rm inf}\dot{\phi}_0 + \frac{\partial V(\phi_0)}{\partial \phi_0} = 0$$
$$H^2_{\rm inf} = \frac{(\dot{\phi}^2 + V(\phi_0))}{3M^2_{\rm Pl}}. \tag{1.6}$$

Here, $M_{\rm Pl}$ is the reduced Planck scale. As shown in figure 1.2, if the inflaton potential is sufficiently flat, ϕ_0 rolls very slowly down the slope. The above equations can then be solved self-consistently by neglecting the acceleration term $\ddot{\phi}_0$ and taking $\dot{\phi}_0^2 \ll V(\phi_0)$, giving approximately constant $\dot{\phi}_0$ and $H_{\rm inf}$,

$$\dot{\phi}_0 \approx \frac{1}{3H_{\rm inf}}\frac{\partial V(\phi_0)}{\partial \phi_0}$$
$$H^2_{\rm inf} \approx \frac{V(\phi_0)}{3M^2_{\rm Pl}}. \tag{1.7}$$

The approximately constant $V(\phi_0)$ while the inflaton is rolling on the plateau is equivalent to a

positive cosmological constant, which gives rise to the approximately dS phase. Long periods of inflation can be realized by making the potential sufficiently flat and terminated by violating slow roll conditions. In figure 1.2, this occurs when the inflaton drops into the valley at the end. The inflaton can later decay through its coupling to lighter species such as Standard Model (SM) particles and/or dark matter (DM), which creates a primordial plasma of lighter particles. This process of transferring the inflaton's energy to the primordial plasma is called "reheating".

In summary, we see that a simple observation of large scale homogeneity leads us to intricate classical dynamics of a new (inflaton) field, which could be playing out at energies as high as $H_{\rm inf} \lesssim 10^{13}$ GeV [7]. Naturally, it would be very exciting if we could learn more about other physics at those energies. These phenomena would necessarily manifest as subdominant effects on top of the dominant inflaton dynamics. To detect these, we need a more sensitive probe, which turns out to be the *quantum* fluctuation of the inflaton.

1.1.2 Primordial fluctuations

While the universe is predominantly homogeneous, there are small perturbations in the distribution of energy density across space. These are reflected in the temperature fluctuations of the CMB in different directions on the sky. The density perturbations can be naturally explained within the inflationary paradigm. While the homogeneous background of the inflaton drives inflation, its quantum fluctuations, stretched to macroscopic scales due to inflation, can seed density perturbations. The statistical correlations in the density perturbations, which can be studied through various cosmological datasets, are therefore linked to quantum correlations of the inflaton field. In this way, any new physics that alters the correlations of the inflaton can in

principle be probed through density perturbations.

To appreciate the robustness of this connection, let us study the nature of quantum fluctuations during inflation. The inflaton field can be separated into a large classical background, which is homogeneous, and small quantum fluctuations on top of it as shown in figure 1.2,

$$\phi(t,\vec{x}) = \phi_0(t) + \delta\phi(t,\vec{x}). \tag{1.8}$$

The isotropy of the dominant part makes momentum space the natural basis. As mentioned before, the physical momentum k_{phy} of a fluctuation keeps red-shifting due to spacetime expansion. We therefore use the comoving momentum $k = a\,k_{phy}$ instead, which factors out the red-shift and hence remains constant. In second quantized form, the fluctuations can be written as

$$\delta\phi(\eta,\vec{x}) = \int \frac{d^3k}{(2\pi)^3}\left[\overline{u}_k(\eta)c_{-\vec{k}} + u_k(\eta)c^\dagger_{\vec{k}}\right] e^{i\vec{k}\cdot\vec{x}}\,, \tag{1.9}$$

where $u_k(\eta)$ is the Fourier mode of $\delta\phi$ and the ladder operators follow the commutation relation $[c_{\vec{k}}, c^\dagger_{\vec{k}'}] = (2\pi)^3\delta^3(\vec{k}-\vec{k}')$. $\overline{u}_k$ is simply the complex conjugate of u_k. During slow roll on the flat region of the inflaton potential, $\delta\phi$ is massless. The field equation of a massless scalar during dS phase is then

$$u_k(\eta)'' - \frac{2}{\eta}u_k(\eta)' + k^2u_k(\eta) = 0\,, \tag{1.10}$$

where the prime denotes $\partial/\partial\eta$. The normalization is fixed using $(\overline{u}_k(\eta)u_k'(\eta) - \overline{u}_k'(\eta)u_k(\eta)) = i\eta^2$. The notion of energy, and therefore vacuum, is ill-defined in dS spacetime, a consequence of the non-trivial time-dependence in Eq. (1.10). At early times $\eta \to -\infty$, however, the equation

reduces to $u_k(\eta)'' + k^2 u_k(\eta) = 0$, which is simply the field equation in Minkowski space. We therefore choose a positive frequency solution at early times $\lim_{\eta\to-\infty} u_k(\eta) \propto e^{ik\eta}$ such that the initial state $|\Omega\rangle$ matches the Minkowski vacuum, i.e. $c_{\vec{k}}\,|\Omega\rangle = 0$. This choice of initial state is called the Bunch-Davies (BD) state.[1] The above procedure fixes the time-dependence of the fluctuations as

$$u_k(\eta) = \frac{(1 - ik\eta)\, e^{ik\eta}}{\sqrt{2\,k^3}}. \tag{1.11}$$

Notice that when $|\eta| < 1/k$, the mode k becomes "super-horizon", that is, the comoving horizon $|\eta|$ becomes smaller than the comoving wavelength k^{-1} of the fluctuation. The mode therefore ceases to evolve, with the late-time amplitude $u_k(\eta) \xrightarrow{\eta\to 0} 1/\sqrt{2k^3}$. The mode remains frozen at this amplitude until the horizon starts expanding again after inflation and becomes comparable to the wavelength of the mode at a much later time. Since no local physics can alter the super-horizon frozen modes, inflationary perturbations are preserved robustly through unknown processes that may have taken place after inflation. In this way, mode-freezing "fossilizes" high energy processes that may be occurring during inflation. These inflationary fossils buried within the density perturbations can therefore create a faithful picture of the inflationary era.

We have been imprecise in using $\delta\phi$ for inflationary perturbations, since it is not invariant under diffeomorphisms. However, a closely related quantity that is invariant is the curvature perturbation ζ, which we will use instead. In a spatially flat gauge [8, 9], $\zeta = -(H_{\rm inf}/\dot{\phi}_0)\,\delta\phi$. The correlations of the curvature perturbation at the end of inflation, $\langle\, \zeta(\vec{k}_1)\cdots\zeta(\vec{k}_n)\,\rangle|_{\eta\to 0}$, can be matched to the moments of the observed density perturbations. These correlations can be calcu-

[1] Any initial occupation of the excited state would be quickly diluted away by inflation. It is therefore robust to choose the empty BD state as the initial state at early time.

lated using the 'in-in' formalism [10–12]. This is very similar in spirit to the 'in-out' formalism used for the calculation of transition amplitudes in particle scattering. The difference is that here, we are interested in the expectation values instead. The expansion of spacetime imparts a time-dependence to the Hamiltonian $\mathrm{H}(t)$. Therefore, in the Schrödinger picture, the state $|\Omega\rangle$ at early times $t_i \to -\infty$ evolves unitarily to $U(t_f, t_i)|\Omega\rangle$ at some later time t_f, where

$$U(t_f, t_i) = T e^{-i\int_{t_i}^{t_f} dt\, \mathrm{H}(t)}. \tag{1.12}$$

The expectation of any operator $\hat{O}$ at time t_f is then given by $\langle\Omega|U(t_f,t_i)^\dagger \hat{O} U(t_f,t_i)\rangle$. We can use the standard methods of field theory to go to the interaction picture where the late-time expectation can be written as

$$\langle \hat{O} \rangle|_{t_f} = \langle 0|\overline{T} e^{+i\int_{-\infty(1+i\epsilon)}^{t_f} dt_2 \mathrm{H}^I_{\mathrm{int}}(t_2)}\ \hat{O}^I(t_f)\ T e^{-i\int_{-\infty(1-i\epsilon)}^{t_f} dt_1 \mathrm{H}^I_{\mathrm{int}}(t_1)}|0\rangle. \tag{1.13}$$

Here, a small deformation of the integration contour into complex time projects the free BD state $|0\rangle$ onto the interacting BD state $|\Omega\rangle$. The superscript I denotes the interaction-picture operators, and $\mathrm{H}_{\mathrm{int}}$ is the interaction part of the full Hamiltonian. By expanding the exponential and making $\hat{O}$ out of curvature perturbations at $t_f \to \infty$, we can evaluate curvature correlations perturbatively in $\mathrm{H}_{\mathrm{int}}$. The calculation follows as usual by expanding in products of Wick contractions and using in-in propagators. These can be depicted as Feynman diagrams by drawing a vertex for each $\mathrm{H}_{\mathrm{int}}$. An example is shown in figure 1.3, where the interaction is mediated by a heavy particle, leading to a 3-point correlation function at late time.

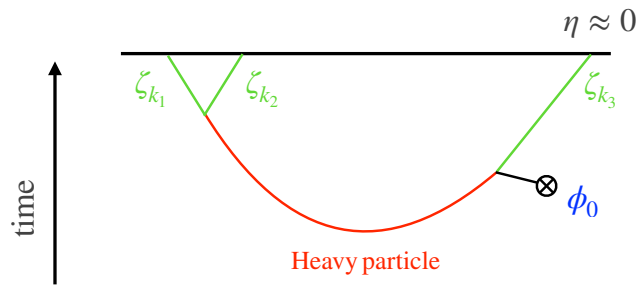

Figure 1.3: An example of a Feynman diagram in the in-in formalism, where the interaction is mediated by the exchange of a heavy particle.

1.2 Primordial non-Gaussianity and signatures of heavy fields

Eq. (1.13) shows us that interactions of the inflaton give rise to connected n-point correlations $\langle\zeta(\vec{k}_1)\zeta(\vec{k}_2)\cdots\zeta(\vec{k}_n)\rangle$. These higher-point functions appear as non-trivial higher moments in the density perturbations, a property we refer to as non-Gaussianity (NG).[2] Unfortunately, the density perturbations we have observed so far have been Gaussian and no (primordial) NG has been detected. However, the experimental precision is expected to improve in near future. Especially with upcoming large-scale structure (LSS) surveys [13, 14] and possible intensity mapping of 21-cm hydrogen line [15, 16], we might be able to detect very small deviations from Gaussianity. This motivates us to explore what new physics may be revealed within these future datasets.

Heavy particles with masses $M \gtrsim H_{\rm inf}$ are particularly interesting, in that they can be produced *on-shell* during inflation. Remember that in an expanding spacetime, a state which is initially empty (the Minkowski vacuum) does not remain so at late time. In dS space, a comov-

[2]NG can also develop after inflation when the modes resume causal evolution. These are induced by the non-linear gravitational interactions. In this thesis, however, we assume that these late-time NG can be subtracted, and only focus on the *primordial* NG induced during inflation.

ing observer perceives the BD state to contain a thermal distribution of particles at the Hawking temperature $T_{\text{Hawking}} = H_{\text{inf}}/2\pi$ (see e.g. [17]). If these produced particles interact with the inflaton, they can later decay into inflaton fluctuations, mediating a non-zero higher-point correlation function of the inflaton [18].

The on-shell propagation of heavy particles leaves a unique non-local feature in the 3-point function of ζ, also known as the bispectrum. When expressed in co-moving momentum space, this spacetime non-locality appears as momentum non-analyticity in the so-called squeezed limit, where one of the momenta is soft, $k_1 \sim k_2 \gg k_3$. A Feynman diagram contributing to the bispectrum in this way is shown in figure 1.3. Typically [19, 20],

$$\frac{\langle\, \zeta_{\vec{k}_1}\zeta_{\vec{k}_2}\zeta_{\vec{k}_3}\,\rangle}{\langle\, \zeta\zeta\,\rangle_{k_1}\langle\, \zeta\zeta\,\rangle_{k_3}} \propto e^{-\pi\mu}\left(\frac{k_3}{k_1}\right)^{3/2\pm i\mu} P_s(\cos\theta) + \cdots \quad \text{where} \quad \mu = \sqrt{\frac{M^2}{H^2} - \frac{9}{4}}. \tag{1.14}$$

Here s is the spin of the heavy particle and θ is the angle between $\vec{k}_1$ and $\vec{k}_3$. We see that the non-analytic dependence on the momentum ratio k_1/k_3, which is either oscillatory ($M > 3H/2$) or a non-standard power law ($M \lesssim 3H/2$), and the angular dependence can be used to do *spectroscopy* of the mass and the spin of the heavy particle. This presents a rare opportunity to *directly* probe particles at extremely high energies $H_{\text{inf}} \lesssim 10^{13}$ GeV, orders of magnitude beyond the scope of any terrestrial collider. This program of research have therefore been dubbed "cosmological collider physics" [19, 20].

While this is a very exciting program, a significant hurdle to fully exploit the reach of the "cosmological collider" is that the non-analytic signal gets exponentially smaller ($\sim e^{-\pi M/H_{\text{inf}}}$) for $M \gg H_{\text{inf}}$ as seen in Eq. (1.14). Intuitively, this is a "Boltzmann suppression" factor due to the thermal-like nature of particle production at the Hawking temperature $T_{\text{Hawking}} = H_{\text{inf}}/2\pi$.

The bispectrum gives the amplitude for particle production, $\propto e^{-M/2T_{\text{Hawking}}}$, corresponding to the standard Boltzmann probability $e^{-M/T_{\text{Hawking}}}$. On the other hand, for small masses $M \ll H_{\text{inf}}$, the non-analytic factor in k_1/k_3 becomes approximately analytic and difficult to disentangle from other NG sources such as inflaton self-interactions.

Based on the previous argument, it would seem that observable masses are restricted to a small range around H_{inf}. In Chapter 2, we investigate whether this is really the case. Given the "thermal" nature of particle production, we ask if a term akin to the chemical potential can be incorporated such that particles at energies beyond the temperature $\sim H_{\text{inf}}$ can be produced. It is indeed possible to do so, and such mechanisms have been previously explored in the context of particles with non-zero spins [21–30]. We extend the chemical potential mechanism to the case of heavy spin-0 particles. Unlike spinful particles, the NG can appear at tree level for spinless particles, making the calculation analytically more tractable. Our mechanism can extend the range of observable masses by approximately two orders of magnitude beyond H_{inf}.

Until now, we have discussed *quantum* production of heavy particles. Interestingly, heavy fields can also be excited *classically* during inflation if there is a sudden change in their potential along the field trajectory. This leads to coherent oscillations of the heavy field background, which can be imprinted as an oscillatory feature in the *two-point* correlation function if the heavy field decays to inflaton fluctuations. Such signals have been searched for in the CMB data from the Planck experiment, but no statistically significant detection has been made [7, 11, 31]. As the sensitivity of CMB data is reaching the fundamental error limit from cosmic variance[3] in certain regions, we ask if the signatures of excited heavy fields can instead be detected with new

[3]As said before, the quantum averages of inflationary fluctuations can be linked to the statistical averages of density perturbations. However, in a single realization that is our universe, we can only make a finite number of measurements for these statistical averages. This introduces a fundamental uncertainty in matching our observations to the theory, which is called the cosmic variance.

cosmological datasets. The reader may wonder what these new datasets are. This is precisely the topic of discussion in the next section.

1.3 In pursuit of new maps: Gravitational Wave Backgrounds

1.3.1 Motivation for new maps

Current observations tell us that the perturbations in all the SM species and DM are completely correlated [7]. These correlated "adiabatic" perturbations suggest a single, common source of underlying fluctuations (for example, the inflaton). Essentially, despite having multiple datasets, we are probing the same inflationary fluctuation. Particles that are weakly interacting with the inflaton are therefore hard to probe as they may not give strong enough signals in any of the known observables. This motivates us to explore alternative data sources that break into these isolated sectors of inflationary fields.

For example, consider an axion-like particle (ALP), which is a well-motivated light field that could have existed during inflation in addition to the inflaton. Such an ALP could be easily misaligned from its minimum. If the mass of the ALP is much smaller than $H_{\rm inf}$, it would also undergo a slow roll similar to that of the inflaton and would not move significantly away from its initial misalignment during inflation. The energy density in the ALP could be subdominant to that of the inflaton such that it does not take part in driving inflation. Its quantum fluctuations, however, would also stretch and freeze-out, similar to those of the inflaton. After the end of inflation, if the ALP decays to some "hidden sector" that does not interact with the SM and DM plasma reheated by the inflaton, its fluctuations can be transferred and retained as the density perturbations of the hidden sector. The fluctuations of the ALP, and hence the hidden sector, are

uncorrelated from those of the inflaton, a property known as isocurvature. Any observable that can track these isocurvature perturbations would then give us a new map of ALP fluctuations.

What might be a good tracker of isocurvature perturbations, just as the CMB photons track adiabatic perturbations? To preserve isocurvature, the tracker species must be weakly interacting with the SM and DM such that it does not thermalize with them after production. It should also be relativistic (or must decay to some form of radiation at a later point) and free-streaming such that it can travel in straight lines over cosmological distances. And lastly, we should be able to detect it. These are strong requirements, but there is at least one candidate that satisfies all of them: gravitational waves.

1.3.2 Cosmological gravitational wave backgrounds

Any cosmological process that produces gravitational waves creates a (stochastic) gravitational wave background (GWB). Gravitational waves (GW) free-stream from the time of their production, and are therefore able to preserve isocurvature perturbations within their fluctuations. They can be produced copiously even by hidden sectors, unlike the SM radiation. On the experimental front, there has been a lot of excitement in gravitational wave detection with various active projects, such as LIGO [32], Virgo [33], and pulsar timing arrays [34], as well as several proposed projects including Cosmic Explorer [35], Einstein telescope [36], LISA [37], TianQin [38], Taiji [39], BBO [40], and DECIGO [41]. Most of these have the potential to go beyond point-like astrophysical sources and detect diffuse stochastic GWBs from the early universe[4]. The theoretical advantage of GW together with the imminent advances on the experimental front

[4]The NANOGrav collaboration, which targets nano-Hz gravitational waves using pulsar timing arrays, recently announced a detection of a stochastic gravitational wave background [42].

makes GW an important prospective cosmological dataset.

While there are various possible sources of GWB in the early universe, it is well-known that first-order phase transitions (PT) tend to produce some of the strongest signals. Therefore, we focus on GWBs produced such phase transitions. If the hidden sector reheated by the ALP undergoes a first-order phase transition, the GWB created by it naturally inherits the isocurvature perturbations of the ALP. A complete model, starting from the ALP field during inflation to the isocurvature GWB fluctuations today, was first described in Ref. [1]. In Chapter 3, we will review their model and use it for the creation of an isocurvature GWB. We will then explore what new physics from the inflationary era might be revealed in the GWB fluctuations. As suggested at the end of section 1.2, we will show that the GWB may contain distinct signatures of classical excitations of heavy fields during inflation, which are otherwise absent in the current maps of adiabatic perturbations. While GW are theoretically ideal, there are significant challenges to their detection, such as astrophysical foreground, detector sensitivity, and angular resolution. Therefore, it is important to explore mechanisms that can enhance the overall strength of GWB. In the model of Ref. [1], it was observed that the strength of a high-isocurvature GWB is suppressed due to the constraints from CMB. In Chapter 4, we propose a modification that can alleviate part of the suppression seen in that model and therefore significantly improve the detection prospects of a high-isocurvature GWB.

Chapter 2: The Scalar Chemical Potential in Cosmological Collider Physics

2.1 Introduction

In Chapter 1, we saw that the paradigm of cosmic inflation gives a robust mechanism for the high degree of homogeneity and isotropy of the universe on very large scales. This is a result of the exponential spacetime expansion driven by the classical background of the inflaton. Furthermore, quantum fluctuations in this paradigm lead to a structure of tiny inhomogeneities, beautifully consistent with the observed Cosmic Microwave Background (CMB). Minimally, these fluctuations can identified with those of the inflaton itself. As reviewed in section 1.1.2, interactions can give rise to small, non-trivial n-point correlations of the inflaton field, which translates into non-Gaussianity (NG) of the density perturbations (for reviews see [43, 44]). Current data suggests that primordial fluctuations are Gaussian to a good precision, indicating that the interactions of the inflaton are weak. However, with the expected improvement in experimental precision in the near future, especially with large-scale structure (LSS) data [13, 14], we can hope to detect small NG, which would reveal subdominant interactions of the inflaton with itself or other fields. In this way, the properties of these other fields during inflation could be revealed through primordial NG observables.[1]

[1] This is true provided the NG induced by gravitational interactions in the late-time Universe can be modeled accurately and separated out. Keeping that in mind, in what follows we will focus exclusively on *primordial* NG sourced during the inflationary era.

In this chapter, we will be interested in the interactions of the inflaton with fields that are heavier than the inflationary Hubble scale $H_{\rm inf}$. The inflating background acts as a source of energy of the order of $H_{\rm inf}$, which can produce particles with masses $M \sim H_{\rm inf}$ on-shell. The propagation of heavy particles followed by their decay to inflaton fluctuations imprint a unique non-analytic signature in the 3-point correlation of curvature perturbations ζ, also called the bispectrum. The distinctive form of this signature allows us to infer the mass and spin of the heavy particle, granting this area of research its name, "cosmological collider physics". The intuition behind this phenomenon is laid out in section 1.2. Here, we summarise a few key points that will be useful for the rest of the discussion. The non-analytic signature becomes apparent in the so-called squeezed limit, where one of the momenta is soft, $k_1 \sim k_2 \gg k_3$. In this limit, the (normalised) bispectrum typically has the form

$$\frac{\langle\, \zeta_{\vec{k}_1} \zeta_{\vec{k}_2} \zeta_{\vec{k}_3} \,\rangle}{\langle\, \zeta_{\vec{k}_1} \zeta_{-\vec{k}_1} \,\rangle \langle\, \zeta_{\vec{k}_3} \zeta_{\vec{k}_3} \,\rangle} \propto e^{-\pi\mu} \left(\frac{k_3}{k_1}\right)^{3/2 \pm i\mu} P_s(\cos\theta) + \cdots \,, \tag{2.1}$$

where $\mu = (M^2/H_{\rm inf}^2 - 9/4)^{1/2}$ and s is the spin of the heavy particle. The spin-dependent angular dependence is captured by the Legendre polynomial $P_s(\cos\theta)$ where θ is the angle between the hard and the soft momenta. The dependence of the bispectrum on the momentum ratio k_1/k_3, which is oscillatory $e^{i\mu \log(k_1/k_3)}$ when μ is real and non-standard power law when μ is imaginary, reveals the mass of the heavy particle. For $M > 3H_{\rm inf}/2$, the bispectrum is exponentially suppressed $e^{-\pi\mu}$ as can be seen in Eq. (2.1). This is referred to as the "Boltzmann" suppression since it is a consequence of the thermal-like nature of particle production at Hawking temperature $T_{\rm Hawking} = H_{\rm inf}/2\pi$. The Boltzmann suppression hinders our ability to probe particles far above $H_{\rm inf}$, restricting the reach of cosmological collider.

Of course, in addition to the production amplitude for new heavy particles, the strength of NG depends on the couplings to the inflaton, which we now consider. Radiative stability of the inflaton potential strongly suggests that it should have derivative couplings predominantly, schematically of the form

$$\frac{1}{\Lambda^{2n+dim(\mathcal{O}_{\rm heavy})-4}}(\partial\phi)^n\mathcal{O}_{\rm heavy}, \tag{2.2}$$

where $\mathcal{O}_{\rm heavy}$ is made from the heavy fields and Λ is the scale at which the non-renormalizable effective field theory (EFT) description breaks down. While the exact cutoff depends on the assumptions about the nature of the UV-physics, plausibly it should be at least as big as the scale of inflaton kinetic energy in slow-roll inflation [45],

$$\Lambda > \sqrt{\dot{\phi}_0} \gtrsim 60H, \tag{2.3}$$

where $\phi_0(t)$ denotes the classical inflaton field trajectory, and where we have used the fact that the CMB temperature power spectrum amplitude implies $H^4/\dot{\phi}_0^2 \approx 10^{-7}$ [7]. It therefore seems that the typical (dimensionless) couplings cannot offset Boltzmann suppression, since they are at best $\lesssim \mathcal{O}(1)$ when some of the inflaton fields are evaluated at the classical expectations $\dot{\phi}_0$, or are significantly suppressed.

The case $n = 1$ in Eq. (2.2) is exceptional however, with the inflaton coupling to a current made of heavy fields, $\partial_\mu\phi J^\mu_{\rm heavy}/\Lambda$. This has been studied in the context of heavy fermionic matter [23, 25–28, 46] and heavy spin-1 bosons [21–24]. Here we will study the simple but interesting case of heavy scalar matter, and show that there are dramatic new features enhancing

the mass reach of cosmological collider physics in a controlled and robust manner. The case of a single real heavy scalar, σ, is however trivial since the unique coupling is given by

$$\mathcal{L}_{\rm int} \supset \frac{g^{\mu\nu}(\partial_\mu\phi)(\partial_\nu\sigma)\sigma}{\Lambda}. \tag{2.4}$$

Integrating by parts and replacing the resulting $\Box\phi$ by $-V'(\phi)$ using the inflaton equation of motion, this only makes a mass contribution to σ modulo small slow-roll corrections. For the case of two real scalars, $\sigma_1,\ \sigma_2$, on the other hand, Eq. (2.4) generalizes to

$$\mathcal{L}_{\rm int} \supset \left(\frac{1}{\Lambda_1}g^{\mu\nu}(\partial_\mu\phi)(\partial_\nu\sigma_1)\sigma_2 - \frac{1}{\Lambda_2}g^{\mu\nu}(\partial_\mu\phi)(\partial_\nu\sigma_2)\sigma_1\right). \tag{2.5}$$

For generic values of Λ_1 and Λ_2, these operators cannot be eliminated by integration by parts. Inserting the time-dependent inflaton background generates a quadratic mixing between the two scalars,

$$\lambda_1\dot{\sigma}_1\sigma_2 - \lambda_2\dot{\sigma}_2\sigma_1, \tag{2.6}$$

where $\lambda_1 = \dot{\phi}_0/\Lambda_1$ and $\lambda_2 = \dot{\phi}_0/\Lambda_2$ are constant in time up to slow-roll corrections. This form is reminiscent of the chemical potential for a complex scalar $\sigma = \sigma_1 + i\sigma_2$.

Indeed, for the special case $\lambda_2 = \lambda_1 = \lambda$ and equal masses $M_1 = M_2$, Eq. (2.6) is the chemical potential $\sim \lambda J^0$, where J is the Noether current associated to σ phase rotations, $J^0 = \dot{\sigma}_1\sigma_2 - \dot{\sigma}_2\sigma_1$. We know that the presence of a chemical potential in standard thermal equilibrium can lead to occupation of excited states with energy greater than the temperature, thereby overcoming Boltzmann suppression. Applying this intuition to the thermal-like nature

of particle production in dS spacetime, we expect particles with masses $M \lesssim \lambda$ to be produced efficiently.[2] Let us estimate the value of chemical potential in our case. From Eq. (2.3), we see that $\lambda \simeq \dot{\phi}_0/\Lambda \lesssim \dot{\phi}_0^{1/2} \approx 60H$, which is $\gg T_{\text{Hawking}}$. That is, we can expect that particles much heavier than H can be produced without the dS analog of Boltzmann suppression, greatly widening the window of observable masses in the cosmological collider physics program.

In this chapter, we demonstrate that the above expectations of non-Boltzmann-suppressed NG mediated by heavy scalars $H \ll M \lesssim \lambda$ can indeed be realized. The simplest way to see how this works is to first note that the "chemical potential" coupling can be thought of as σ being charged under a "gauge" field which is pure gauge in form, $A_\mu \equiv \partial_\mu \phi/\Lambda$. It can therefore be removed by doing a gauge transformation on σ. However, this will induce gauge transform phase factors in any other gauge-non-invariant masses or couplings in the theory:

$$\mathcal{L} \supset \mathcal{O}(\sigma, \sigma^\dagger) + \text{c.c.} \to \mathcal{O}(\sigma, \sigma^\dagger)\, e^{iq\phi/\Lambda} + \text{c.c.}, \tag{2.7}$$

where $\mathcal{O}$ is an interaction/mass in σ violating the fake "gauge invariance" by q units (that is, there are q more powers of σ than $\sigma^\dagger$). Given the slow-roll approximation, $\phi_0 \approx \dot{\phi}_0 t$, we see that we get effective high-frequency couplings of the heavy fields.

$$\mathcal{L} \supset \mathcal{O}(\sigma, \sigma^\dagger)\, e^{iq\lambda t} + \text{c.c.}, \tag{2.8}$$

For example, if we depart from our assumption of equal heavy masses, or from $\lambda_2 = \lambda_1$, there are effectively $\sigma\sigma$-type symmetry-breaking mass corrections accompanying the chemical potential,

[2] More precisely, the inflationary couplings may contribute to the mass during inflation, in which case the condition for efficient production is effective mass, $M_{\text{eff}} \lesssim \lambda$.

which will be multiplied by $e^{2i\lambda t}$ after the field redefinition. In general, in this way we get time-dependent σ couplings and mass terms with frequencies of order λ. These couplings can then naturally result in efficient particle production for masses up to $\lambda \gg H$.[3] We will study the case of $\mathcal{O}(\sigma, \sigma^\dagger)$ with $q = 1$ and show that it can lead to striking NG signatures of the heavy scalars, the largest and the most theoretically tractable occurring via tree-level exchanges with the inflaton. These can be readily observable in upcoming LSS experiments [13, 47–49] and future 21-cm cosmology [15, 50]. We will also briefly study the case $q = 2$, which is mostly closely analogous to the fermionic case. In general, both $q = 1$ and $q = 2$ can co-exist, but for simplicity, we pursue them separately.

There are some qualitative differences between the heavy scalar case here and the earlier studies of heavy fields with non-zero spin s. In these previous studies [21–23, 23–28], the chemical potential modifies the dispersion relation with a term linear in momentum using a coupling $\propto \vec{k} \cdot \vec{s}$. The modified frequency $\omega(t)$ violates the adiabaticity condition, i.e. $\dot{\omega}/\omega^2 \gg 1$, at a certain time during the evolution of mode functions, leading to particle production. Of course a similar effect is impossible for spin-0 fields. While these spin dependent effects are absent for scalar fields, a chemical potential can still manifest as an explicit time-dependence in mass corrections and couplings as seen in Eq. (2.8), which is the source of particle production. Ref. [23] surveyed different chemical potential possibilities, but concluded that there was no effect for complex scalars as given by Eq. (2.5). In this chapter, we will show that there is indeed a strong effect within theoretical control.

Our main focus will be on $q = 1$ case with $\mathcal{O} = \sigma$, which has the advantage that the

[3] It may be surprising to the reader that the chemical potential only overcomes dS Boltzmann suppression when the related charge is *not* conserved. However, in ordinary thermal equilibrium there is an analogous feature, in that it is crucial that the subsystem under study can gain/lose charge to the external thermal bath. If the subsystem charge is exactly conserved, then here too the chemical potential would have no effect.

contribution of the inflaton-scalar coupling to the bispectrum occurs at *tree-level*. This removes the loop-suppression seen in gauge boson and fermion cases, gives a robustly large mass reach up to $\dot{\phi}_0^{1/2} \approx 60H$, while allowing an analytically tractable calculation. Note this is significantly higher than the chemical potential reach for fermions $\simeq \dot{\phi}_0^{1/4} H^{1/2} \approx 10H$. While the spin-1 chemical potential reach is as high as the scalar case $M \simeq \dot{\phi}_0^{1/2} \approx 60H$, getting a viable signal requires a period of exponential growth in particle production [21], in turn needing a very close coincidence of the mass and chemical potential scales in order to stop in time. By contrast in the scalar case, no exponential growth or coincidences are necessary. The meaning of mass is obscured in the presence of large chemical potential due to its breaking of Lorentz invariance. But we will carefully identify the physical mass after the field rotation which removes the chemical potential, as in Eq. (2.7), and show that strong signals can be obtained for physical masses $\gg H$ without any fine-tuning of parameters.

The field redefinition leading to the form of Lagrangian, Eq. (2.7), demonstrates that the scalar chemical potential is equivalent to a special form of particle production due to non-derivative couplings to the inflaton, similar in spirit to [51]. However there are some significant differences. Generally, non-derivative couplings will induce radiative corrections to the inflationary effective potential upon integrating out the heavy matter, of concern given the fragility of slow-roll inflation. Furthermore, non-derivative couplings of (nearly) massless scalars ordinarily yield divergent late-time correlators. However, in our case the non-derivative couplings to the inflaton do not break the shift symmetry under which $\phi \to \phi + c$ when it is accompanied by the phase rotation $\sigma \to e^{-ic/\Lambda}\sigma$. This means that at the level of the inflationary effective potential, radiative corrections from integrating out matter must respect ϕ shift symmetry, and hence vanish. This matches the obvious conclusion from the original form of interaction, Eq. (2.5), where the

derivative couplings of ϕ cannot generate an effective ϕ potential. Similarly, the manifest derivative couplings in Eq. (2.5) ensure that all late-time divergences cancel when the correlators are computed using Eq. (2.7) (which however is more useful in computing the effects of the chemical potential). Finally, it may appear worrying that the non-derivative couplings in Eq. (2.7) can be Taylor expanded in powers of ϕ/Λ even though the ϕ field transit is much greater than Λ. In general, non-derivative couplings containing $(\phi/\Lambda)^n$ would not have a controlled expansion. But here the symmetry requirement that the inflaton factor non-linearly carries "charge" q uniquely gives the re-summed form $e^{iq\phi/\Lambda}$, thus matching the manifest EFT control in Eq. (2.2).

As seen in Eq. (2.8), the particle production resulting from the chemical potential is continuous and approximately constant during inflation, given by a steady frequency of the effective couplings/masses, as opposed to a more time-dependent or punctuated particle production. Relatedly, the shift symmetry gives us an approximate time translation invariance, which combined with dS isometries implies that approximate scale invariance of our correlators is maintained. This structure of correlators is useful in doing the spectroscopy of the heavy particles from the bispectrum in a simple way.

The rest of the chapter is organized as follows: we describe the relevant observables and fix the notation in section 2.2. Then in section 2.3, we present our model that illustrates the mechanism of chemical potential in the context of heavy complex scalars. Section 2.4 contains the main results of this chapter where we calculate the bispectrum in the squeezed limit and analyze the strength of NG in various regions of the parameter space. There we also give a simple and intuitive estimate of the bispectrum using the method of stationary phase while a full calculation is carried out in section A.2 using the results from section A.1. After discussing in section 2.5 a novel procedure to infer the effective mass of the heavy particle during inflation

from the momentum dependence of the bispectrum, we conclude in section 2.6.

Note that in this chapter, we have set $H_{\rm inf} = 1$ for the ease of calculation, unless it is explicitly written. Factors of $H_{\rm inf}$ can be restored by dimensional analysis.

2.2 Preliminaries

Let us start with the definitions and the notation that we will used throughout the chapter. The (approximate) dS metric during inflation is given by

$$ds^2_{\rm dS} = -dt^2 + e^{2H_{\rm inf}t}\, d\vec{x}^2 \tag{2.9}$$

$$= \frac{-d\eta^2 + d\vec{x}^2}{(\eta H_{\rm inf})^2}, \tag{2.10}$$

where $\eta H_{\rm inf} = -e^{-H_{\rm inf}t}$. The inflaton is separated into the dominant homogeneous background $\phi_0(t)$ and the subdominant fluctuations $\delta\phi(t,\vec{x})$. In the spatially flat gauge [8], the fluctuations are related to the gauge-invariant comoving curvature perturbation ζ (for a review and original references see e.g. [9]) as

$$\zeta = -\frac{\delta\phi}{\dot{\phi}_0}\,. \tag{2.11}$$

The observations require the primordial power spectrum $P_\zeta(k)$ to be (almost) scale invariant,

$$P_\zeta(k) \equiv \langle\, \zeta_{\vec{k}}\zeta_{-\vec{k}}\,\rangle' = \frac{1}{\dot{\phi}_0^2}\langle\, \delta\phi_{\vec{k}}\delta\phi_{-\vec{k}}\,\rangle' = \frac{1}{\dot{\phi}_0^2}\frac{(k/k_*)^{n_s-1}}{2k^3}\,, \tag{2.12}$$

where $n_s \approx 0.96$, $k_* = 0.05$ Mpc^{-1} is the pivot scale, and $\dot{\phi}_0^{1/2} \approx 60 H_{\rm inf}$ [7]. Here and below, the $\langle \cdots \rangle'$ denotes the convention that momentum conserving factors have been taken out,

$$\langle\, \zeta_{\vec{k}_1} \cdots \zeta_{\vec{k}_n} \,\rangle \equiv (2\pi)^3 \delta^3(\vec{k}_1 + \cdots + \vec{k}_n)\, \langle\, \zeta_{\vec{k}_1} \cdots \zeta_{\vec{k}_n} \,\rangle' \,. \tag{2.13}$$

The primordial non-gaussianity (NG) corresponds to having connected non-zero $n-$point correlation functions of ζ. More specifically, the bispectrum is the 3-point function in momentum space denoted by $B(k_1, k_2, k_3)$,

$$B(k_1, k_2, k_3) = \langle\, \zeta_{\vec{k}_1} \zeta_{\vec{k}_2} \zeta_{\vec{k}_3} \,\rangle' \,. \tag{2.14}$$

It is a convention to denote the bispectrum by $F(k_1, k_2, k_3)$, which can be thought of as the bispectrum appropriately normalized by the power spectrum

$$F(k_1, k_2, k_3) = \frac{5}{6} \frac{B(k_1, k_2, k_3)}{(P_\zeta(k_1)\, P_\zeta(k_3) + P_\zeta(k_1)\, P_\zeta(k_2) + P_\zeta(k_2)\, P_\zeta(k_3))} \,. \tag{2.15}$$

In our analysis, we will be mostly interested in the squeezed limit, i.e., when $k_1 \approx k_2 \gg k_3$. Using Eq. (2.11) and Eq. (2.12), the expression for F can be simplified in this limit as

$$F_{\rm squeezed} \approx \frac{5}{12} \dot{\phi}_0 \frac{\langle\, \delta\phi_{\vec{k}_2} \delta\phi_{\vec{k}_3} \delta\phi_{\vec{k}_1} \,\rangle'}{\langle\, \delta\phi_{\vec{k}_1} \delta\phi_{-\vec{k}_1} \,\rangle' \langle\, \delta\phi_{\vec{k}_3} \delta\phi_{-\vec{k}_3} \,\rangle'} . \tag{2.16}$$

It is customary to typify the strength of NG by a single number, $f_{\rm NL}$, at the "equilateral" config-

uration where all the momenta have the same magnitude,

$$f_{\rm NL} \equiv F(k,k,k) = \frac{5}{18}\frac{B(k,k,k)}{P_\zeta(k)^2} \ . \tag{2.17}$$

This definition is consistent with the convention for local NG ($f_{\rm NL}^{\rm local}$) at the equilateral point. Using Eq. (2.11) and Eq. (2.12), this can be written in terms of inflaton correlation functions,

$$f_{\rm NL} = \frac{5}{18}\,\dot\phi_0\,\frac{\langle\, \delta\phi_{\vec k_1}\delta\phi_{\vec k_2}\delta\phi_{\vec k_3}\,\rangle}{\langle\, \delta\phi_{\vec k}\delta\phi_{-\vec k}\,\rangle^2} \ , \tag{2.18}$$

where $|\vec k_{1,2,3}| = |\vec k|$.

The constraints on $f_{\rm NL}$ vary depending on the shape of the bispectrum. The latest Planck analysis sets the bounds as $|f_{\rm NL}| \sim \mathcal{O}(5-50)$ depending on the shape of NG [52]. In the near future, LSS observations (see e.g. [13]) are expected to probe $\delta f_{\rm NL} \sim \mathcal{O}(1)$ — bringing several of our benchmark scenarios under the LSS reach, as we will see later. More futuristic cosmic variance limited 21-cm cosmology experiments can reach even better sensitivities with $\delta f_{\rm NL} \sim \mathcal{O}(10^{-2})$ or even smaller [15, 16].

We use the in-in formalism to evaluate the bispectrum. A quick overview of this formalism is presented in section 1.1.2. The reader may refer to [53] for a more comprehensive review. Using this formalism, the expectation value of an operator $\hat O$ at any single time t can be perturbatively computed using,

$$\langle\hat O\rangle|_t = \langle 0|\left(\bar T e^{i\int_{-\infty(1+i\epsilon)}^{t}{\rm H}_{\rm int}^I\,dt}\right)\hat O^I(t)\left(T e^{-i\int_{-\infty(1-i\epsilon)}^{t}{\rm H}_{\rm int}^I\,dt}\right)|0\rangle \ , \tag{2.19}$$

where we can expand in powers of the interaction Hamiltonian ${\rm H}_{\rm int}^I$ to any desired order. Here

we see the appearance of both time- and anti-time ordered exponentials, respectively denoted by T and $\bar{T}$ operators. The state $|0\rangle$ is the free Bunch-Davies vacuum but the $i\epsilon$ prescription projects it onto the interacting vacuum $|\Omega\rangle$. The superscript I denotes fields in the interaction picture. The bispectrum is the 3-point correlation function evaluated at the end of inflation, i.e., $\hat{O}(t) \to (\delta\phi_{\vec{k}_1}\delta\phi_{\vec{k}_2}\delta\phi_{\vec{k}_3})|_{\eta\approx 0}$ in Eq. (2.19).

2.3 A minimal model

2.3.1 Chemical potential for a complex scalar with U(1) symmetry breaking

Before getting into our actual models, let us consider a simple case of a complex scalar field σ charged under a global $U(1)$, where we introduce an explicit chemical potential by hand. The conserved current $J_\mu = -i(\sigma\partial_\mu\sigma^\dagger - \sigma^\dagger\partial_\mu\sigma)$ can be used to introduce a non-zero chemical potential, λ, by shifting the Hamiltonian density as $\mathcal{H} \to \mathcal{H} - \lambda J_0$. Integrating out the canonical momentum in the partition function, $\mathcal{Z} \sim \int D\sigma\, D\Pi\, \exp[-\int d^4x\,(\mathcal{H} - \lambda J_0)]$, gives the corresponding Lagrangian, $\mathcal{Z} \sim \int D\sigma\, \exp[-\int d^4x\, \mathcal{L}_\sigma]$ [54],

$$\begin{aligned}\mathcal{L}_\sigma \supset\ & -|\partial\sigma|^2 - M^2|\sigma|^2 + i\lambda(\dot{\sigma}^\dagger\sigma - \dot{\sigma}\sigma^\dagger) + \lambda^2|\sigma|^2 \\ =\ & [(\partial_t + i\lambda)\sigma]\,[(\partial_t - i\lambda)\sigma^\dagger] - |\partial_i\sigma|^2 - M^2|\sigma|^2\,. \end{aligned} \tag{2.20}$$

Note that adding a chemical potential in the Hamiltonian is equivalent to introducing coupling of the complex field to an external gauge potential A_μ with a non-zero time component A_0. Then $A_0(\equiv \lambda)$ is the chemical potential. It is important to clearly identify the physical mass in terms of the various mass parameters in the Lagrangian, since it is obscured by the Lorentz-violating

nature of the chemical potential. We will address this question shortly.

In the standard thermodynamic setting, the subsystem under consideration can gain or lose charges to the heat bath, which is key to chemical potential having physical effect. In the inflationary setting on the other hand, the subsystem is the entirety of space and hence, the charge conservation is exact. This can be easily seen by noting that any non-trivial effect of the chemical potential can be eliminated by a suitable field rotation, $\sigma \to e^{-i\lambda t}\tilde{\sigma}$.[4] Nevertheless, non-conservation due to the heat bath can be replaced here by small explicit breaking of the $U(1)$ symmetry. Consider the simplest case of adding a linear symmetry-breaking term as follows,

$$\mathcal{L}_\sigma \supset [(\partial_t + i\lambda)\sigma]\,[(\partial_t - i\lambda)\sigma^\dagger] - |\partial_i\sigma|^2 - M^2|\sigma|^2 - \alpha\,(\sigma + \sigma^\dagger)\,. \tag{2.21}$$

After the field rotation as before $\sigma \to e^{-i\lambda t}\tilde{\sigma}$, we see that the symmetry-breaking term retains the effect of chemical potential in the form of a time-dependent phase,

$$\mathcal{L}_{\tilde{\sigma}} \supset -|\partial\tilde{\sigma}|^2 - M^2|\tilde{\sigma}|^2 - \alpha\,(\tilde{\sigma}e^{-i\lambda t} + \tilde{\sigma}^\dagger e^{+i\lambda t})\,. \tag{2.22}$$

For two independent real scalar fields $(\sigma_1,\ \sigma_2)$ as in Eq. (2.5), such symmetry-breaking terms are naturally present when written in terms of $\sigma = \sigma_1 + i\sigma_2$.

In our full model, we will realize such a residual time-dependence with frequency λ, coupled to inflaton fluctuations, capable of producing heavy particles in association with inflatons at energies of order λ. But we can already identify the physical mass, having eliminated the chemical potential in favor of the time-dependent α coupling. Treating the linear term in Eq. (2.22)

[4]When the subsystem is coupled to a thermal bath, the non-zero time-component of the gauge field can not be rotated away due to periodic boundary conditions on the fields in the subsystem.

as a perturbation for small α, we see that the physical mass is nothing but M (e.g., M^2 term is the standard dS-invariant if we are expanding around dS-spacetime). We will generalize this approach to identifying the physical mass after field re-definition and computing the NG signals as a function of it in what follows.

2.3.2 Realizing a chemical potential via inflaton couplings

Coming to the case of inflation, the chemical potential can be implemented with derivative coupling of inflaton with the complex scalar current J^μ. Consider the Lagrangian,

$$\mathcal{L} = \sqrt{-g}\Bigg\{ -\frac{1}{2}(\partial\phi)^2 - V(\phi) - |\partial\sigma|^2 - M^2|\sigma|^2 \\ -\frac{i\partial_\mu\phi}{\Lambda}\left(\sigma\partial^\mu\sigma^\dagger - \sigma^\dagger\partial^\mu\sigma\right) - \frac{c\,(\partial\phi)^2}{\Lambda^2}|\sigma|^2 + \alpha\left(\sigma+\sigma^\dagger\right)\Bigg\}\,. \tag{2.23}$$

Here $V(\phi)$ is some suitable inflationary potential whose details we do not need to specify. The second line describes the interactions, out of which the first term is the coupling of the inflaton to the current. In the slow-roll approximation, the inflaton gets a homogeneous background such that $\dot{\phi}_0 \simeq (60H_{\rm inf})^2$ is a constant to a good approximation. This generates a chemical potential,

$$-\frac{1}{\Lambda}\partial_\mu\phi J^\mu \supset \frac{\dot{\phi}_0}{\Lambda}J_0 = \lambda J_0, \tag{2.24}$$

where $\lambda \equiv \dot{\phi}_0/\Lambda$. It is evident from the discussion above that we must also include a small explicit symmetry-breaking term, which is the last term on the second line in Eq. (2.23). The second term, with the coefficient c, should be naturally present as it is consistent with the shift symmetry of inflaton as well as the $U(1)$ symmetry of the complex scalar. The coefficient of this

term gets modified as it is also generated from the kinetic term for σ after the field redefinition that removes the dimension-5 inflaton-current coupling,

$$\sigma = e^{-i\phi/\Lambda}\,\tilde{\sigma}\ . \tag{2.25}$$

Then Eq. (2.23) can be written as

$$\mathcal{L} = \sqrt{-g}\Big\{\ -\frac{1}{2}(\partial\phi)^2 - V(\phi) - |\partial\tilde{\sigma}|^2 - M^2|\tilde{\sigma}|^2 \\ +(1-c)\,\frac{(\partial\phi)^2}{\Lambda^2}|\tilde{\sigma}|^2 + \alpha\left(\tilde{\sigma}e^{-i\phi/\Lambda} + \tilde{\sigma}^\dagger e^{+i\phi/\Lambda}\right)\Big\}\ . \tag{2.26}$$

In the new field variable $\tilde{\sigma}$, the chemical potential gets translated into a non-trivial phase in the symmetry-breaking term. Another advantage of this step is that the Lagrangian in Eq. (2.26) no longer has interactions with time-derivatives $\partial_0\tilde{\sigma}$. It is then straightforward to get the interaction Hamiltonian starting from the Lagrangian density using $\mathcal{H}_{\rm int} = -\mathcal{L}_{\rm int}$.[5] For simplicity and perturbative control, we restrict the coefficient $|c| \leq 1$. Note that $c = 1$ is a case that corresponds to the addition of chemical potential without affecting the mass, as seen in Eq. (2.20). Here, we keep this coefficient arbitrary.

2.3.3 Analysis of the spatially homogeneous background of the complex scalar

In the following, we will restrict our attention to the parameter space where interactions in Eq. (2.26) are perturbative such that the inflaton dynamics is not altered at leading order in perturbation theory. Therefore we can treat the homogeneous part of the inflaton as ϕ_0 where

[5] It can be shown that the additional terms with $(\partial\phi)^2$ give rise to extra interaction terms only at fourth-order in perturbation or higher [55]. Since we are only looking at diagrams at tree level, this will not affect our analysis.

$\dot{\phi}_0 \approx (60 H_{\rm inf})^2$. This perturbativity is ensured by taking $\Lambda(\alpha)$ sufficiently large(small), as discussed in more detail in section 2.4.2. The term linear in $\tilde{\sigma}$ in Eq. (2.26) breaks the $U(1)$ symmetry explicitly and gives a *time-dependent* background $\tilde{\sigma}_0$ which we estimate now.

From Eq. (2.26), the Lagrangian terms involving $\tilde{\sigma}$ are

$$\begin{aligned}\mathcal{L}_{\tilde{\sigma}} \supset \sqrt{-g}\Big\{ -|\partial\tilde{\sigma}|^2 - \left(M_{\rm eff}^2 + \mathcal{O}(\delta\phi)\right)|\tilde{\sigma}|^2 + \underbrace{\alpha\left(\tilde{\sigma}\, e^{-i(\phi_0+\delta\phi)}/\Lambda + \text{h.c.}\right)}\Big\} \\ \alpha\left(\tilde{\sigma}\, e^{-i\lambda t}\left(1+\mathcal{O}(\delta\phi)\right) + \text{h.c.}\right)\,,\end{aligned} \tag{2.27}$$

where we have expanded the inflaton field around its background with $\delta\phi$ denoting the inflaton fluctuations. In the second line, we have used the fact that $\dot{\phi}_0 \approx \text{constant}$ during inflation in the slow-roll approximation, and hence, we can write

$$\frac{\phi_0}{\Lambda} \approx \frac{\dot{\phi}_0}{\Lambda}(t-t_i) = \lambda\,(t-t_i)\,. \tag{2.28}$$

Here, t_i depends on the initial value of ϕ_0. Its exact value will not affect our final results as it only appears as an unimportant overall phase (hence, not shown in Eq. (2.27)). The effective mass of the heavy field can be written as

$$M_{\rm eff}^2 = M^2 + (1-c)\,\lambda^2. \tag{2.29}$$

Following the discussion in section 2.3.1, the physical (approximately) dS-invariant mass is most readily identified in $\tilde{\sigma}$ variable, where the chemical potential term is redefined away. In the limit where α perturbation is switched off, $M_{\rm eff}$ is clearly the physical mass during inflation. For $\alpha = 0$, the heavy particle production is Boltzmann suppressed by $e^{-\pi M_{\rm eff}/H_{\rm inf}}$ for $M_{\rm eff} \gg H_{\rm inf}$ in standard

fashion, whereas it is produced (in association with inflatons) without any such suppression in the presence of non-zero α for $\lambda \gtrsim M_{\rm eff} > H_{\rm inf}$, due to the high λ-frequency time-dependence of the α coupling. In particular, no fine-tuned cancellation between various parameters in $M_{\rm eff}$ is needed to obtain an unsuppressed signal.

The parameter c controls the contribution of chemical potential to the effective mass, as well as symmetry-preserving couplings of the heavy particle to the inflaton. As mentioned before, $c = 1$ is a case where the coupling of inflaton to the current only generates a chemical potential and does not affect the physical mass, i.e., $M_{\rm eff} = M$. For any value of c, we expect the range of values $-(1-c)\lambda^2 < M^2 < c\lambda^2$, corresponding to $H_{\rm inf} < M_{\rm eff} < \lambda$, to give unsuppressed signal (we will see this explicitly later). Note that this range includes tachyonic $M^2 < 0$ for $c < 1$. However, it does not lead to instability as long the physical mass $M_{\rm eff}^2 > 0$. The meaning of tachyonic M is only seen after inflation ends, and ϕ decays and lies at the minimum of its potential today, $\dot{\phi} \propto \lambda = 0$, so M represents the post-inflation physical mass. Being tachyonic, $M^2 < 0$, indicates only that σ will be unstable to acquiring a post-inflation background value. But this does not affect our inflationary analysis of NG produced.

Due to the time-dependent phase in the term linear in $\tilde{\sigma}$, the standard procedure of shifting the field by a constant value will not get rid of this linear term completely. We instead solve the equation of motion (EOM) of $\tilde{\sigma}_0$ following from Eq. (2.27). Let us write the high-frequency phase in α-coupling using conformal time as

$$e^{\pm i\lambda(t-t_i)} = e^{\pm i\lambda \log(\eta/\eta_i)} \,, \tag{2.30}$$

From Eq. (2.27), the EOM for the complex scalar field (in the dS limit of inflationary spacetime)

is

$$\left[\partial_\eta^2 \, - \frac{2}{\eta}\,\partial_\eta + \left(-\nabla^2 + \frac{M_{\rm eff}^2}{\eta^2}\right)\right]\tilde{\sigma}(\vec{x},\eta) \;=\; +\alpha\,\frac{(\eta/\eta_i)^{-i\,\lambda}}{\eta^2}\;. \tag{2.31}$$

This is a standard EOM for a massive scalar field in the inflationary background with an extra time-dependent piece on the right hand side coming from the linear term. This extra piece sources spatially homogeneous part, i.e., $\vec{k} = 0$ mode. We write $\tilde{\sigma} \to \tilde{\sigma}_0(\eta) + \delta\tilde{\sigma}(\vec{x},\eta)$, where $\tilde{\sigma}_0$ is the time-dependent homogeneous background, and $\delta\tilde{\sigma}(\vec{x},\eta)$ is the fluctuation. Putting $\nabla^2\tilde{\sigma}_0 = 0$ in Eq. (2.31), we get the equation for the homogeneous part,

$$\left[\partial_\eta^2 \, - \frac{2}{\eta}\,\partial_\eta + \frac{M_{\rm eff}^2}{\eta^2}\right]\tilde{\sigma}_0(\eta) \;=\; +\alpha\,\frac{(\eta/\eta_i)^{-i\,\lambda}}{\eta^2}\;. \tag{2.32}$$

The general solution can be written as,

$$\tilde{\sigma}_0(\eta) = C_\pm\,(-\eta)^{3/2\,\pm\,i\,\mu} \;+\; \alpha\,\frac{(\eta/\eta_i)^{-i\,\lambda}}{(M_{\rm eff}^2 - \lambda^2 + 3i\lambda)}\;, \tag{2.33}$$

where $\mu = \sqrt{M_{\rm eff}^2 - 9/4}$. The first term corresponds to oscillations of the massive field given by its mass $\sim \mu$, and the usual $1/\sqrt{\rm volume}$ dilution of mode functions. Due to the dilution, this term quickly becomes negligible. On the other hand, the second term exhibits a forced-oscillator type behaviour coming from the linear $\tilde{\sigma}$-term in Eq. (2.27), which gives time-dependence to the background $\tilde{\sigma}_0$. This term does not dilute (nor diverge) in late time and vanishes at the end of

inflation as $\dot{\phi}_0 \to 0$. Thus, the homogeneous part of the complex field can be written as

$$\tilde{\sigma}_0(\eta) \;\approx\; \frac{\alpha\,(-\eta)^{-i\,\lambda}\,e^{i\theta}}{\sqrt{(M_{\rm eff}^2-\lambda^2)^2+9\lambda^2}} \equiv \kappa^\dagger(-\eta)^{-i\,\lambda}\;, \tag{2.34}$$

where $\theta = \tan^{-1}(-3\lambda/(M_{\rm eff}^2-\lambda^2)+\lambda\ln(-\eta_i))$ is a constant phase. Notice that the amplitude of the oscillating background in Eq. (2.34) depends on the detuning between the natural frequency $M_{\rm eff}$ and the external frequency λ, just like the case of a forced oscillator. The damping comes from the Hubble friction $\sim \frac{1}{\eta}\partial_\eta\tilde{\sigma}$ in Eq. (2.31).

An important consequence of the time-dependent background for the heavy complex scalar is that the leading NG will now be at *tree-level*, which means we no longer pay the $\sim 1/(16\pi^2)$ loop suppression, and the calculation is a lot more tractable as compared to the loop-level calculations in scenarios involving chemical potential for fermions and gauge bosons.

2.3.4 Quantization and mode functions of the complex scalar

After doing the analysis for the homogeneous solution, let us move on to discuss the fluctuations. Taking a Fourier transform in Eq. (2.31), we get the equation for the $\vec{k}$-th mode ($\vec{k}\neq 0$) as

$$\left[\partial_\eta^2 \;-\frac{2}{\eta}\,\partial_\eta + \left(k^2+\frac{M_{\rm eff}^2}{\eta^2}\right)\right]\delta\tilde{\sigma}(\vec{k},\eta) \;=\; 0\;. \tag{2.35}$$

Here, we have ignored a quadratic mixing between $\delta\tilde{\sigma}$ and $\delta\phi$. We will later take this into account perturbatively in the insertion approximation. The right hand side in Eq. (2.31) is purely spatially homogeneous and does not affect $\vec{k}\neq 0$. The equation for $\delta\tilde{\sigma}(\vec{k},\eta)$ is the standard EOM for

a massive scalar field in the dS limit of inflationary spacetime. In terms of the redefined field $\tilde{\sigma}$, the effect of the chemical potential is solely on the time-dependent background $\tilde{\sigma}_0$, while the fluctuations follow the same dynamics as a free massive scalar field. The general solution is

$$\delta\tilde{\sigma}(\vec{k},\eta) = c_1\,(-\eta)^{3/2}H^{(1)}_{i\mu}(-k\eta) \;+\; c_2\,(-\eta)^{3/2}H^{(2)}_{i\mu}(-k\eta)\;. \tag{2.36}$$

Here, $H^{(1\text{ or }2)}_{i\mu}$ are the Hankel functions. The quantized field can be taken to have the following form,

$$\delta\tilde{\sigma}(\vec{k},\eta) = \bar{g}_k(\eta)\,a_{-\vec{k}} + f_k(\eta)\,b^\dagger_{\vec{k}}\;, \tag{2.37}$$

where $a_{\vec{k}}\,(a^\dagger_{\vec{k}})$ and $b_{\vec{k}}\,(b^\dagger_{\vec{k}})$ are the destruction (creation) operators for particle and anti-particle excitations, respectively, i.e. $a_{\vec{k}}|0\,\rangle = b_{\vec{k}}|0\,\rangle = 0$, where $|0\,\rangle$ is the Bunch-Davies (BD) vacuum. Imposing canonical quantization, using the conjugate momentum $\pi(\vec{x},\eta)$, $[\delta\tilde{\sigma}(\vec{x},\eta),\pi(\vec{x},\eta)] = +i\,\delta^3(\vec{x}-\vec{y})$ translates into standard commutation relations $[a_{\vec{k}},a^\dagger_{\vec{k}'}] = (2\pi)^3\delta^3(\vec{k}-\vec{k'})$ and $[b_{\vec{k}},b^\dagger_{\vec{k}'}] = (2\pi)^3\delta^3(\vec{k}-\vec{k'})$, given that the mode functions satisfy the Wronskian condition

$$\bar{g}_k g'_k - f_k\bar{f}'_k = i\eta^2\;, \tag{2.38}$$

where $'$s denote derivatives with respect to conformal time η.

Treating all the interactions perturbatively, the quadratic part of the Lagrangian for fluctuations corresponds to a free complex scalar in dS space-time. Thus, minimization of Hamiltonian requires choosing appropriate positive frequency mode at early time, i.e., $f_k, g_k \propto e^{ik\eta}$ at $\eta \to -\infty$. These initial condition and the Wronskian condition fix the form of the mode

functions g_k, f_k to be

$$\begin{aligned} \bar{g}_k &= N_g^*(-\eta)^{3/2} H_{i\mu}^{(1)}(-k\eta) \\ f_k &= N_f(-\eta)^{3/2} H_{i\mu}^{(2)}(-k\eta) \ , \end{aligned} \tag{2.39}$$

where $N_f = \frac{\sqrt{\pi}}{2} e^{\pi\mu/2} e^{-i\pi/4}$ and $N_g^* = \frac{\sqrt{\pi}}{2} e^{-\pi\mu/2} e^{+i\pi/4}$. It can be checked that $g_k = f_k$. Furthermore,

$$\begin{aligned} \bar{g}_k(\eta \to -\infty) &= \frac{1}{\sqrt{2k}}(-\eta) e^{-ik\eta} \\ f_k(\eta \to -\infty) &= \frac{1}{\sqrt{2k}}(-\eta) e^{ik\eta}, \end{aligned} \tag{2.40}$$

as required by imposing BD initial conditions.

Assuming the validity of perturbative analysis (discussed in section 2.4.2), we can then take the standard $M \to 0$ limit for inflaton. Quantizing inflaton fluctuation as

$$\delta\phi(\vec{k}, \eta) = \bar{u}_k c_{-\vec{k}} + u_k c_{\vec{k}}^\dagger, \tag{2.41}$$

we get the mode functions by setting $\mu = 3i/2$ in Eq. (2.39),

$$\begin{aligned} u_k(\eta) &= \frac{(1 - ik\eta)\, e^{ik\eta}}{\sqrt{2\, k^3}} \\ \bar{u}_k(\eta) &= \frac{(1 + ik\eta)\, e^{-ik\eta}}{\sqrt{2\, k^3}} \ . \end{aligned} \tag{2.42}$$

2.3.4.1 Boltzmann-like suppression for fields with no chemical potential

Having studied the mode functions, let us take a detour to understand the origin of the Boltzmann suppression in the absence of chemical potential. For this exercise, it is sufficient to consider only one real scalar σ_1 out of σ. Let us take this field to have the dS mass M. The

free field EOM is the same as in Eq. (2.35). The scalar field is then quantized using BD initial condition as,

$$\sigma_1 = \bar{f}_k a_{-\vec{k}} + f_k a^\dagger_{\vec{k}} \qquad \text{where} \quad \bar{f}_k = N_f^*(-\eta)^{3/2} H^{(1)}_{i\mu}(-k\eta)\,; \quad \mu = \sqrt{M^2 - 9/4}\,. \tag{2.43}$$

The BD initial condition means that at early time, the modes were deep into the horizon and hence look like Minkowski modes in the appropriate time variable. This is reflected in the early time limit of the mode functions,

$$\bar{f}_k \xrightarrow{\eta\to-\infty} \bar{f}_k(in) = \frac{1}{\sqrt{2k}}(-\eta)e^{-ik\eta}, \tag{2.44}$$

where the *positive* frequency solution is chosen as it minimizes the Hamiltonian at early times. In a time-dependent space-time, the same mode may not be the *local* positive frequency mode at late times. This point becomes apparent in the late time limit where (up to some unimportant phases)

$$\begin{aligned}\bar{f}_k \xrightarrow{\eta\to0} \bar{f}_k(out) &\simeq \frac{(-\eta)^{3/2}}{2\sqrt{\pi}}\left(\Gamma(-i\mu)(-k\eta/2)^{i\mu}e^{\pi\mu/2} + \Gamma(i\mu)(-k\eta/2)^{-i\mu}e^{-\pi\mu/2}\right) \\ &\xrightarrow{M\gg H} \frac{(-\eta)^{3/2}}{\sqrt{2\mu}}\left((-k\eta/2)^{i\mu} + e^{-\pi\mu}(-k\eta/2)^{-i\mu}\right),\end{aligned} \tag{2.45}$$

where in the second line, we have used

$$|\Gamma(i\mu)| \sim \sqrt{2\pi}|\mu|^{-1/2}e^{-\pi|\mu|/2}. \tag{2.46}$$

Notice that a small *negative* frequency part, $(-\eta)^{-i\mu} \sim e^{i\mu t}$, has developed, with a relative amplitude $e^{-\pi\mu}$, which corresponds to 'cosmological particle production'. Then the probability of particle production is $\sim e^{-2\pi\mu}$, which is approximately $e^{-M/T_{\rm Hawking}}$, where the cosmological Hawking Temperature is given by $T_{\rm Hawking} = H_{\rm inf}/(2\pi)$. The non-analytic signature in the bispectrum comes from the 'on-shell' production and propagation of heavy particles, which is always accompanied by this exponential suppression unless there is another energy source of particle production. In our model, we create just such a source by harnessing the kinetic energy of the inflaton through its coupling to the complex current. This introduces an additional explicit time-dependence with frequency $\lambda \gg H_{\rm inf}$, and hence produces heavy fields more efficiently.

2.3.5 Interactions of the complex scalar with the inflaton

We focus on the interactions contributing to the bispectrum at tree-level, which is the dominant contribution in our model. These include terms that mix the complex scalar field with inflaton fluctuations, $\mathcal{H}_{\rm mix}$, and 3-point interactions, $\mathcal{H}_3$. The relevant terms in the Lagrangian can be obtained from Eq. (2.26) after expanding the phase of $\tilde{\sigma}$,

$$e^{i\,\phi/\Lambda} \;=\; e^{i\,(\phi_0+\delta\phi)/\Lambda} \;\approx\; e^{-i\lambda\log\,(\eta/\eta_i)}\left(1 + i\frac{\delta\phi}{\Lambda} + ...\right)\,, \tag{2.47}$$

and using the background of $\tilde{\sigma}$ from Eq. (2.34). The quadratic mixing terms are

$$\mathcal{H}_{\rm mix} = -\mathcal{L}_{\rm mix} = \beta_1\,(-\eta)^{i\lambda}\,(\dot{\delta\phi})\,\delta\tilde{\sigma} \;+\; \beta_2\,(-\eta)^{i\lambda}\,\delta\phi\,\delta\tilde{\sigma} + \text{h.c.}\,, \tag{2.48}$$

where

$$\beta_1 = +\frac{2(1-c)\dot{\phi}_0\kappa}{\Lambda^2}, \qquad \beta_2 = i\frac{\alpha}{\Lambda}. \tag{2.49}$$

The relevant 3-point interaction terms are given by,

$$\mathcal{H}_3 = -\mathcal{L}_3 = \rho_1 (-\eta)^{i\lambda} (\partial\delta\phi)^2 \delta\tilde{\sigma} + \rho_2 (-\eta)^{i\lambda} (\delta\phi)^2 \delta\tilde{\sigma} + \text{h.c.}\,, \tag{2.50}$$

where

$$\rho_1 = -\frac{(1-c)\kappa}{\Lambda^2}, \qquad \rho_2 = \frac{\alpha}{2\Lambda^2}\,. \tag{2.51}$$

Here we have read off the interaction terms directly from the Lagrangian using $\mathcal{H}_{\text{int}} = -\mathcal{L}_{\text{int}}$, which holds at third order in fluctuations (as explained after Eq. (2.26)). The extra time dependence $(-\eta)^{\pm i\lambda}$ in the vertices is the most important consequence of the chemical potential. It effectively injects (removes) energy of order λ at each vertex, making the production of fields in the entire range $H_{\text{inf}} < M_{\text{eff}} \lesssim \lambda$ possible without the dS Boltzmann suppression.

2.4 Approximate calculation of the bispectrum in the squeezed limit

Having worked out the interaction terms, we now evaluate the bispectrum following Eq. (2.19),

$$\langle\, \delta\phi_{\vec{k_1}} \delta\phi_{\vec{k_2}} \delta\phi_{\vec{k_3}} \,\rangle'|_{\eta\to 0} = \langle 0| \left(\bar{T} e^{i\int_{-\infty(1+i\epsilon)}^{0} \mathrm{H}^I_{\text{int}}\, d\eta_1}\right) \delta\phi_{0,\vec{k_1}} \delta\phi_{0,\vec{k_2}} \delta\phi_{0,\vec{k_3}} \left(T e^{-i\int_{-\infty(1-i\epsilon)}^{0} \mathrm{H}^I_{\text{int}}\, d\eta_2}\right) |0\rangle\,, \tag{2.52}$$

where $\delta\phi_{0,\vec{k}}$ is the inflaton fluctuation with comoving momentum $\vec{k}$ at $\eta \to 0$. By expanding the exponential operator, it is easy to see that the bispectrum vanishes at zeroth order and the leading contribution comes from tree diagrams. While in general, the bispectrum contains both analytic and the non-analytic pieces, it is the latter that encode distinctive on-shell effects of the massive particle. Hence, for the purposes of this work, we will compute only the non-analytic parts, keeping in mind that for a complete analysis one would also need to take into account the analytic contributions. However, the analytic contributions can be estimated to be comparable to our non-analytic estimates below in the regime of mild squeezing, i.e., analytic and non-analytic contributions to $f_{\rm NL}$ are comparable. The general form can be written as,

$$\begin{aligned}
&\langle\ \delta\phi_{\vec{k_1}}\delta\phi_{\vec{k_2}}\delta\phi_{\vec{k_3}}\ \rangle'|_{\eta\to 0} = I_{++} + I_{+-} + I_{-+} + I_{--},\\
&I_{\pm\pm} \propto (\mp i)(\mp i)\int \frac{d\eta_1}{\eta_1^4}\int \frac{d\eta_2}{\eta_2^4}\, h(\eta_1,\eta_2)\, \tilde{d}_{\pm}(k_1,k_2;\eta_1)\, d_{\pm}(k_3;\eta_2)\times\\
&\qquad\qquad \{G_{\pm\pm}(k_3;\eta_1,\eta_2) + F_{\pm\pm}(k_3;\eta_1,\eta_2)\}\ . \qquad (2.53)
\end{aligned}$$

The '$+$' indicates that the vertex that comes from $e^{-i\int \mathrm{H_{int}} d\eta}$ with time ordering, while '$-$' comes from $e^{+i\int \mathrm{H_{int}} d\eta}$ with anti-time ordering. Note that the first sign on $I_{\pm\pm}$ corresponds to the cubic interaction vertex, and the second sign corresponds to the inflaton-scalar mixing vertex. The function $h(\eta_1,\eta_2)$ captures the explicit time-dependence of the form $(-\eta)^{\pm i\lambda}$ in the vertex coefficients in eqs. (2.48) and (2.50). The functions $d_{\pm}$, $\tilde{d}_{\pm}$ are the inflaton bulk-boundary propagators,

and they can be evaluated using Eq. (2.42) as

$$d_+(k_3;\eta_2) \equiv \langle\delta\phi(\eta_0)\delta\phi(k_3,\eta_2)\rangle|_{\eta_0\to 0} = \frac{1}{2k_3^3}(1-ik_3\eta_2)e^{ik_3\eta_2}$$
$$\tilde{d}_+(k_1,k_2;\eta_1) \equiv \langle\delta\phi(\eta_0)\delta\phi(\eta_0)\delta\phi(\eta_1,k_1)\delta\phi(\eta_1,k_2)\rangle|_{\eta_0\to 0} = \frac{1}{4k_1^3k_2^3}(1-ik_1\eta_1)(1-ik_2\eta_1)e^{ik_{12}\eta_1}, \tag{2.54}$$

where $d_-(\tilde{d}_-)$ is the conjugate of $d_+(\tilde{d}_+)$, and $k_{12} = k_1 + k_2$. $G_{\pm\pm}$ and $F_{\pm\pm}$ are bulk-bulk propagators for the complex scalar field. These can be evaluated using Eq. (2.37) as

$$\begin{aligned}
G_{++}(k;\eta_1,\eta_2) &= \langle\,\delta\tilde{\sigma}(\eta_1)\delta\tilde{\sigma}^\dagger(\eta_2)\,\rangle_{++} = \bar{f}_k(\eta_2)f_k(\eta_1)\theta(\eta_2-\eta_1) + \bar{g}_k(\eta_1)g_k(\eta_2)\theta(\eta_1-\eta_2),\\
G_{+-}(k;\eta_1,\eta_2) &= \langle\,\delta\tilde{\sigma}(\eta_2)\delta\tilde{\sigma}^\dagger(\eta_1)\,\rangle_{+-} = \bar{g}_k(\eta_2)g_k(\eta_1),\\
F_{++}(k;\eta_1,\eta_2) &= \langle\,\delta\tilde{\sigma}^\dagger(\eta_1)\delta\tilde{\sigma}(\eta_2)\,\rangle_{++} = \bar{f}_k(\eta_1)f_k(\eta_2)\theta(\eta_1-\eta_2) + \bar{g}_k(\eta_2)g_k(\eta_1)\theta(\eta_2-\eta_1),\\
F_{+-}(k;\eta_1,\eta_2) &= \langle\,\delta\tilde{\sigma}^\dagger(\eta_2)\delta\tilde{\sigma}(\eta_1)\,\rangle_{+-} = \bar{f}_k(\eta_2)f_k(\eta_1)\ .
\end{aligned} \tag{2.55}$$

The remaining propagators can be related to these using relations,

$$G_{--} = (G_{++})^*\ , \quad G_{-+} = (G_{+-})^*\ , \quad F_{--} = (F_{++})^*\ , \quad F_{-+} = (F_{+-})^*. \tag{2.56}$$

We will fix the proportionality factors in the above by using the relevant coupling parameters in a moment. I_{-+} and I_{--} are complex conjugates of I_{+-} and I_{++}, respectively. Thus, we only evaluate I_{+-} and I_{++} explicitly.

We compute the full analytic form of these contributions in Eq. (A.2), however next we show the same calculation using the stationary phase method, which is more transparent in terms of demonstrating particle production through chemical potential. It also proves to be a good approximation in the parameter regime of our interest, $\lambda \gg M_{\rm eff} > H_{\rm inf}$, as we will see in

figure 2.2.

2.4.1 Dominant contribution: I_{+-} diagrams

Let us start with the evaluation of I_{+-} diagram. For the purpose of illustrating the mechanism, we focus on the sub-diagram consisting of vertices with larger coefficients, i.e., β_2 and ρ_2. We will see later that the NG estimate thus obtained matches the full analytic calculation very well.

Using the form of vertices in eqs. (2.48) and (2.50), and Eq. (2.53) the sub-diagram has the form

$$I_{+-} \supset (-i)(+i) \int \frac{d\eta_1}{\eta_1^4} \int \frac{d\eta_2}{\eta_2^4} \tilde{d}_+(k_1, k_2; \eta_1) d_-(k_3; \eta_2) \times \\ \left\{ \beta_2 \rho_2^* \left(\frac{\eta_2}{\eta_1}\right)^{i\lambda} G_{+-}(k_3; \eta_1, \eta_2) + \beta_2^* \rho_2 \left(\frac{\eta_2}{\eta_1}\right)^{-i\lambda} F_{+-}(k_3; \eta_1, \eta_2) \right\} . \tag{2.57}$$

Looking at Eq. (2.55), we see that the first term on the second line corresponds to the contraction $\langle\, \delta\tilde{\sigma}\delta\tilde{\sigma}^\dagger \,\rangle$, describing particle propagation, while the second corresponds to $\langle\, \delta\tilde{\sigma}^\dagger\delta\tilde{\sigma} \,\rangle$, describing anti-particle propagation. Without loss of generality, let us take $\lambda > 0$ in the following analysis. We will see that with this choice, the contribution from the term with F_{+-} propagator dominates. It will become clear that if $\lambda < 0$, the analysis for F_{+-} and G_{+-} is simply switched, but our conclusions remain unchanged.

Let us start with the second term with F_{+-} propagator, which is represented diagramatically in figure 2.1 (a). There are two integrals, the one with soft inflaton leg (k_3) coming from anti-time

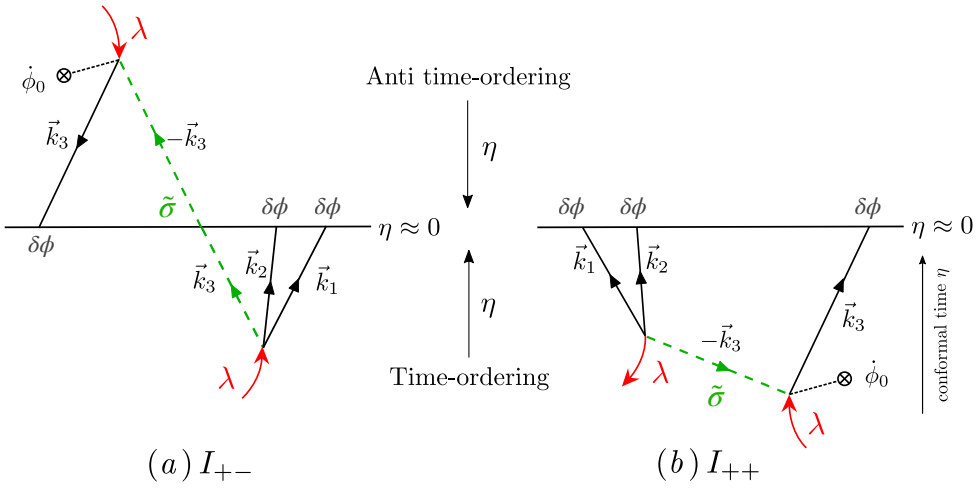

Figure 2.1: Representation of the dominant tree-level contributions from I_{+-} and I_{++} diagrams to the bispectrum. For the convenience of notation, the time ordered part of the diagram is shown below the $\eta \approx 0$ line with time running upwards, while the anti-time ordered part is shown above with time running downwards. An incoming (outgoing) arrow at a vertex denotes injection (extraction) of energy. This makes it plausible that the I_{+-} contribution is enhanced compared to the I_{++} contribution, since for the former the "resonant" particle production through energy injection is efficient at *both* the vertices. Further explanations can be found in the text.

ordering, while the other with hard momenta $(k_{1/2})$ coming from time ordering.

$$I_{+-} \supset \beta_2^* \rho_2 \int \frac{d\eta_1}{\eta_1^4} \int \frac{d\eta_2}{\eta_2^4} \left(\frac{\eta_2}{\eta_1}\right)^{-i\lambda} \tilde{d}_+(k_1, k_2; \eta_1) d_-(k_3; \eta_2)\, F_{+-}(k_3; \eta_1, \eta_2) = \beta_2^*\, \rho_2\, I_{k_3}^{(-)} I_{k_{12}}^{(+)}\,, \tag{2.58}$$

where $I_{k_3}^{(-)}$ is the η_2-integral at the mixing vertex from the anti-time ordered part, while $I_{12}^{(+)}$ is the η_1-integral from the time-ordered part with cubic interaction. Using mode functions for the inflaton and complex scalar from eqs. (2.39) and (2.42), we get

$$I_{k_3}^{(-)} = \int_{-\infty}^{0} \frac{d\eta_2}{\eta_2^4} \left(\frac{(1 + ik_3\eta_2)e^{-ik_3\eta_2}}{2k_3^3}\right) (-\eta_2)^{-i\lambda} \times \underbrace{\left(N_f^*\, (-\eta_2)^{3/2} H_{i\mu}^{(1)}(-k_3\eta_2)\right)}_{\bar{f}_{k_3}(\eta_2)}\,. \tag{2.59}$$

For fields with mass greater than the Hubble scale, the rate of expansion of space-time is much

smaller as compared to their natural frequency, i.e., $\dot{\omega}/\omega^2 \ll 1$. Thus, the dynamics of the mode functions can be effectively captured by the adiabatic modes. For the ease of calculation, let us make the substitution $x = -k_3\eta_2$. Then the full mode function can be approximated by the adiabatic mode as,

$$N_f^* \, x^{1/2} H_{i\mu}^{(1)}(x) \underset{\mu \gg H}{\sim} \left. \frac{e^{-i\int \omega(\eta) d\eta}}{\sqrt{2\omega(\eta)}} \right|_{x=-k\eta} = \frac{e^{i\int \sqrt{1+\frac{\mu^2}{x^2}} dx}}{\sqrt{2}\left(1+\frac{\mu^2}{x^2}\right)^{1/4}} \, . \tag{2.60}$$

The integrand then separates into a slowly-varying polynomial function and a highly oscillatory phase $g(x)$,

$$I_{k_3}^{(-)} \sim \frac{1}{2\sqrt{2}k_3^{3/2-i\lambda}} \int_0^\infty dx \, \frac{x^{-5/2}(1-ix)}{(x^2+\mu^2)^{1/4}} \, e^{ig(x)} \, , \tag{2.61}$$

$$\text{where} \qquad g(x) = -\lambda \log(x) + x + \int_{x_0}^{x} \sqrt{1+\frac{\mu^2}{x^2}} dx \, . \tag{2.62}$$

Here, x_0 corresponds to the time at the start of inflation. The dominant contribution comes from the stationary points where $g'(x_*) = 0$, i.e., $-\frac{\lambda}{x_*} + 1 + \sqrt{1+\frac{\mu^2}{x_*^2}} = 0$. In this case, there is only one stationary point at $x_* = (\lambda^2 - \mu^2)/(2\lambda)$. Using this, we get $g''(x_*) = 4\lambda^3/(\lambda^4 - \mu^4)$ for $\lambda > \mu$. The integration can then be evaluated as

$$\begin{aligned} I_{k_3}^{(-)} &\sim \frac{1}{2\sqrt{2}k_3^{3/2-i\lambda}} \frac{x_*^{-5/2}(1-ix_*)}{(x_*^2+\mu^2)^{1/4}} e^{ig(x_*)} \sqrt{\frac{2\pi}{g''(x_*)}} \\ &\sim \frac{\sqrt{\pi}}{k_3^{3/2-i\lambda}} e^{i\delta(\lambda,\mu)} \lambda^{1/2} (\lambda^2-\mu^2)^{-1}. \end{aligned} \tag{2.63}$$

Here we have used the fact that $x_* \gg 1$, true for most of the parameter space we are interested in. The phase factor $\delta(\lambda, \mu) = g(x_*) - \pi/2$ is independent of k_3. The additional phase coming

from the choice of initial point x_0 is arbitrary, but it cancels with the phase from $I^{(+)}_{k_{12}}$ integral.

The role of the chemical potential is now apparent. The existence of stationary phase indicates on-shell production of particles. The phase $(-\eta)^{-i\lambda}$ coming from the chemical potential can be thought of as *providing* energy $\sim \lambda$ into the vertex, which is converted to produce inflaton and complex scalar fluctuations at time x_*. If $\lambda < \mu$, there is no stationary point and we will get an exponential suppression[6]

$$I_{+-} \propto e^{-\pi(\mu-\lambda)}, \tag{2.64}$$

which as $\lambda \to 0$, becomes the usual Boltzmann-like suppression $e^{-\pi\mu}$ for heavy fields.

Doing a similar calculation for $I^{(+)}_{k_{12}}$ yields,

$$\begin{aligned} I^{(+)}_{k_{12}} &= \frac{1}{4k_1^3k_2^3}\int_{-\infty}^{0}\frac{d\eta_1}{\eta_1^4}\left((1-ik_1\eta_1)(1-ik_2\eta_1)e^{ik_{12}\eta_1}\right)(-\eta_1)^{+i\lambda}\times\underbrace{\left(N_f\,(-\eta_1)^{3/2}H^{(2)}_{i\mu}(-k_3\eta_1)\right)}_{f_{k_3}(\eta_1)} \\ &\xrightarrow{x=-k_3\eta_1} \frac{1}{4\sqrt{2}k_1^3k_2^3k_3^{-3/2+i\lambda}}\int_0^\infty dx\frac{x^{-5/2}(1+ipx/2)^2}{(x^2+\mu^2)^{1/4}}\,e^{ih(x)}\,, \end{aligned} \tag{2.65}$$

where

$$h(x) = \lambda\log(x) - px - \int_{x_0}^{x}\sqrt{1+\frac{\mu^2}{x^2}}dx\,. \tag{2.66}$$

Stationary phase occurs when $\frac{\lambda}{x_*} - p - \sqrt{1+\frac{\mu^2}{x_*^2}} = 0$. Then in the large p limit, for $\lambda > \mu$,

[6] In the absence of a stationary point for $\lambda < \mu$, we can perform a Wick rotation $x \to ix$, and carry out the integration in Eq. (2.61) explicitly to see the $e^{-\pi(\mu-\lambda)}$ factor. For more details, refer to a similar calculation within the I_{++} contributions in section 2.4.4, where such suppression is always present.

$x_* \approx \frac{\lambda-\mu}{p}$, and $h''(x_*) \approx -\frac{p^2}{\lambda-\mu}$. This gives,

$$I^{(+)}_{k_{12}} \sim \frac{1}{4\sqrt{2}k_1^3 k_2^3 k_3^{-3/2+i\lambda}} \frac{x_*^{-5/2}(1+ipx_*/2)^2}{(x_*^2+\mu^2)^{1/4}} e^{ih(x_*)} \sqrt{\frac{2\pi}{h''(x_*)}} \,. \tag{2.67}$$

Since x_* depends on p, we get a p-dependent phase from $e^{ih(x_*)}$,

$$h(x_*) = \left[\underline{\lambda \log(x)} - px - \left\{ \sqrt{x^2+\mu^2} + \underline{\mu \log(x)} - \mu \log\left(\mu^2 + \mu\sqrt{x^2+\mu^2}\right) \right\} \Big|_{x_0}^{x} \right]_{x_* \approx \frac{\lambda-\mu}{p}} . \tag{2.68}$$

In the above, we have taken a squeezed limit $p \gg \lambda/\mu \sim 1$, where this expression can be simplified to separate out the momentum-dependent phase. The underlined terms in the above expression result in a non-analytic momentum dependence of the form $p^{i(\mu-\lambda)}$,

$$e^{ih(x_*)} \underset{p\gg 1}{\to} e^{i\delta'(\lambda,\mu)} p^{i(\mu-\lambda)}, \tag{2.69}$$

where $\delta'(\lambda,\mu)$ is a p-independent phase. The integral can be written as

$$I^{(+)}_{k_{12}} \sim \frac{-\sqrt{\pi}}{16 k_1^3 k_2^3 k_3^{-3/2+i\lambda}} e^{i\delta'(\lambda,\mu)} \mu^{-1/2} p^{3/2+i(\mu-\lambda)} \,. \tag{2.70}$$

Putting together eqs. (2.63) and (2.70), we get

$$I_{+-} \supset \beta_2^* \rho_2 I^{(+)}_{k_3} I^{(-)}_{k_{12}} \sim \frac{\pi \beta_2^* \rho_2}{16 k_1^3 k_2^3} \mu^{-1/2} \lambda^{1/2} (\lambda^2-\mu^2)^{-1} p^{3/2+i(\mu-\lambda)} \,, \tag{2.71}$$

up to a constant phase.

Going back to the first term in Eq. (2.57) with G_{+-}, we observe that the calculation can be repeated with the replacement $\lambda \to -\lambda$. However, it can be checked that in this case, the stationary point does not exist for either of the two integrals, and the integrand is highly oscillatory in the entire domain of integration $\eta \in (-\infty, 0)$. This gives an exponentially suppressed contribution, and hence can be ignored in our estimate.[7]

From this analysis, it becomes clear that the correct way to think of I_{+-} diagrams is figure 2.1 (a). In the figure, we represent anti-time ordered part above the line denoting the end of inflation ($\eta \approx 0$) with time running downwards. This is simply a convenient notation to differentiate between $I_{+-/-+}$ and $I_{++/--}$ diagrams. The interaction Hamiltonian evolves the initial Bunch-Davies vacuum into a superposition of excited states $|p_i ... p_{n_{\delta\phi}}; q_j ... q_{n_{\tilde{\sigma}}}\rangle$ where $n_{\delta\phi}$ is the number of inflaton excitations while $n_{\tilde{\sigma}}$ is the number of excitations of the heavy field. The correlation functions essentially picks the amplitude of the state $|k_3; k_3\rangle$ from the 'bra' and the amplitude of $|k_1, k_2; k_3\rangle$ from the 'ket'.

The direction of the arrow for chemical potential λ in figure 2.1 depends on the phase. For the vertices from time ordered part, $(-\eta)^{i\lambda}$ corresponds to 'injection' of energy into the vertex, while $(-\eta)^{-i\lambda}$ corresponds to 'removal' of energy. This is exactly opposite for the anti-time ordered part. This will also help us understand why I_{++}/I_{--} contribution is sub-dominant.

The I_{++} diagram is different than I_{+-} in the sense that the produced heavy particle decays into inflaton at a later time as seen in figure 2.1 (b). This means that while the energy of order λ is injected at one vertex to boost particle production, similar amount of energy is removed at the other vertex. If $\lambda > \mu$, the production of massive particle at k_3 vertex is efficient, i.e. stationary point exists for the oscillating integrand. But the decay of the produced particle into

[7] For $\lambda < 0$, G_{+-} gives the dominant contribution while F_{+-} contribution is exponentially suppressed.

inflatons at k_{12} vertex is suppressed as the particle has to decay not only into inflatons but also give away energy of order λ which is greater than its own energy $\sim \mu$. This can be seen by the absence of a stationary point for the integral at this vertex, resulting in the suppression of the form $e^{-\pi(\lambda-\mu)}$. On the other hand, if $\mu > \lambda$, the reverse is true, that is, decay at k_{12} will be efficient, but production at k_3 will be suppressed as $e^{-\pi(\mu-\lambda)}$. All in all, we expect I_{++} to at least have the suppression of the form $e^{-\pi|\lambda-\mu|}$.

We postpone the calculation of the sub-dominant I_{++} diagram to section 2.4.4 (the full analytic treatment can be found in section A.2.2), and instead discuss some of our main results in the following sections.

2.4.2 Constraints

Before looking at the strength of the non-analytic signal, we determine the constraints on various parameters of our model in Eq. (2.26). To ensure a controlled derivative expansion in $(\partial\phi)^2/\Lambda^4$, we require $\Lambda > \dot{\phi}_0^{1/2}$. From the Planck data [7], $H_{\rm inf}^4/\dot{\phi}_0^2 = 8.25 \times 10^{-8}$ at $k_* = 0.05$ Mpc^{-1} for slow-roll inflation. This gives $\dot{\phi}_0 \approx (60H_{\rm inf})^2$ implying the chemical potential $\lambda \lesssim 60H_{\rm inf}$. Thus λ can be much larger than the typical energy of the expanding space-time during inflation $\sim H_{\rm inf}$ while ensuring EFT control.

We must also ensure that the standard inflaton dynamics is not affected to first order and we have perturbative control over the interactions. The background of the complex scalar in Eq. (2.34) modifies the kinetic energy of the inflaton as $(\partial\phi)^2 \to [1 - 2(1-c)|\tilde{\sigma}_0|^2/\Lambda^2]\,(\partial\phi)^2$.

This gives a constraint on the amplitude of the background as

$$\frac{|\kappa|^2}{\Lambda^2} \ll 1 \ . \tag{2.72}$$

We also require the correction to the power spectrum from the interaction Hamiltonian to be sub-leading. The dominant corrections come from the symmetry-breaking term $\mathcal{H}_{\rm int} \supset \alpha\tilde{\sigma}e^{-i\phi/\Lambda} \sim -\alpha\kappa^\dagger(\delta\phi/\Lambda)^2 - i\alpha e^{-i\phi_0/\Lambda}\delta\tilde{\sigma}(\delta\phi/\Lambda) + \text{c.c.}$. These two contributions are comparable, and can be estimated to be $\Delta P_\zeta/P_\zeta \sim \alpha|\kappa|/\Lambda^2$, which should be $\ll 1$. For $\lambda > M_{\rm eff}$, $\kappa \sim \alpha/\lambda^2$. Then it is then easy to see than this constraint is stronger than Eq. (2.72), and the overall constraint is simply $\alpha/\Lambda \ll \lambda$. In order to have only a percent level correction to the power spectrum [7], we take a more conservative value for the coefficient of the symmetry-breaking term,

$$\frac{\alpha}{\Lambda} = 0.1\,\lambda \tag{2.73}$$

We will use this value of α while evaluating the strength of NG in the next section.

2.4.3 Central results

With the technical calculation out of the way, we are now in a position to explore the strength of the non-gaussian signal in different parameter regimes. In this subsection, we present the central results of this chapter.

Let us estimate the size and the shape of the bispectrum in the squeezed limit using Eq. (2.16),

$$F_{\rm squeezed} \approx \frac{5}{12}\dot{\phi}_0 \frac{\langle\, \delta\phi_{\vec{k}_1}\delta\phi_{\vec{k}_2}\delta\phi_{\vec{k}_3}\,\rangle'}{\langle\, \delta\phi_{\vec{k}_1}\delta\phi_{-\vec{k}_1}\,\rangle'\langle\, \delta\phi_{\vec{k}_3}\delta\phi_{-\vec{k}_3}\,\rangle'}, \tag{2.74}$$

where we take

$$\langle\, \delta\phi_{\vec{k}_2}\delta\phi_{\vec{k}_3}\delta\phi_{\vec{k}_1}\,\rangle' \simeq I_{+-} + I_{-+}, \tag{2.75}$$

since the dominant contribution comes from I_{+-} and I_{-+}, as seen previously in section 2.4.1. From Eq. (2.71) and Eq. (2.12), we get [8]

$$F_{\text{squeezed}} \approx \frac{5}{12}\dot{\phi}_0(4k_1^3k_3^3)\frac{2\pi\beta_2^*\rho_2}{16k_1^3k_2^3}\,\mu^{-1/2}\lambda^{1/2}(\lambda^2-\mu^2)^{-1}\,p^{3/2+i(\mu-\lambda)} + \text{c.c.}. \tag{2.76}$$

Here, we have included the symmetry factor of 2 from k_{12} vertex. Inserting values for β_2, ρ_2 from eqs. (2.49) and (2.51), we get the parametric form of NG in squeezed limit $k_1 \approx k_2 \gg k_3$,

$$F_{\text{squeezed}} \simeq \frac{5\pi}{12\sqrt{2}}\frac{\dot{\phi}_0}{\Lambda}\left(\frac{\alpha}{\Lambda}\right)^2\left(\frac{\lambda}{\mu}\right)^{1/2}(\lambda^2-\mu^2)^{-1}\left(\frac{p}{2}\right)^{-3/2+i(\mu-\lambda)} + \text{c.c.}. \tag{2.77}$$

We saturate the constraint on α given in Eq. (2.73) and use $\lambda \equiv \dot{\phi}_0/\Lambda$ to get the approximate form of NG in the squeezed limit as

$$F_{\text{squeezed}} \simeq \frac{5\pi}{12\sqrt{2}} \times 10^{-2} \times \frac{\lambda^{7/2}}{\mu^{1/2}\,(\lambda^2-\mu^2)}\left(\frac{p}{2}\right)^{-3/2+i(\mu-\lambda)} + \text{c.c.}. \tag{2.78}$$

Let us denote the amplitude of the non-analytic signal in the bispectrum by f_{oscil} such that,

$$F_{\text{squeezed}} \approx |f_{\text{oscil}}(\mu,\lambda)|\left(\left(\frac{p}{2}\right)^{-3/2+i(\mu-\lambda)} + \text{c.c.}\right), \tag{2.79}$$

[8] We will drop some $p-$independent phases, since here we will be interested in the magnitude of NG, f_{oscil} defined below.

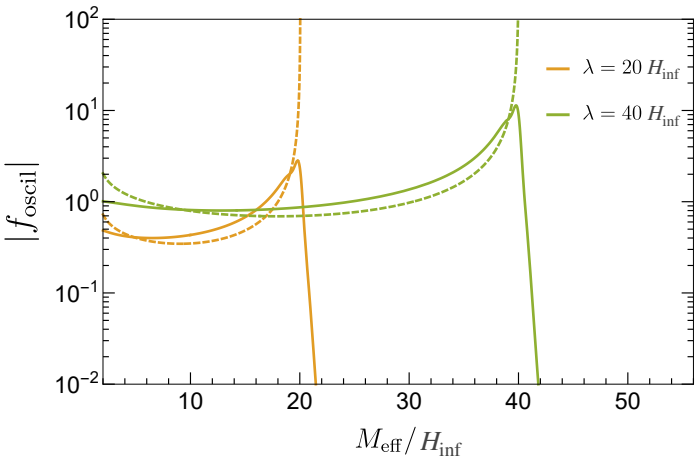

Figure 2.2: Comparison of $|f_{\rm oscil}|$ as a function of $M_{\rm eff}$ using stationary phase (dashed) and the full analytic form (solid) for two different values of the chemical potential $\lambda = 20H_{\rm inf}$ (yellow) and $\lambda = 40H_{\rm inf}$ (green), at $c = 0.5$ for $\alpha/\Lambda = 0.1\lambda$. The parametric dependence matches for $\mu < \lambda$ as expected with a difference of an $\mathcal{O}(1)$ factor. This mismatch can be attributed to contributions from other vertices which we did not consider in the stationary phase approximation above just for simplicity. Note the full calculation also smooths out the naive divergence in the stationary phase estimate as $\mu \approx \lambda$ since for such μ the approximation made in our stationary phase estimate breaks down.

Then,

$$|f_{\rm oscil}(\mu,\lambda)| = \frac{5\pi}{12\sqrt{2}} \times 10^{-2} \frac{\lambda^{7/2}}{\mu^{1/2}\,(\lambda^2-\mu^2)}. \tag{2.80}$$

From here onward, we will use $|f_{\rm oscil}|$ to characterize the size of NG.

In figure 2.2, we compare above expression from the approximate calculation with the exact calculation from Appendix A.2 for a generic value of $c = 0.5$ and $\lambda = 20,\ 40$. We see that in the region where the approximations are valid, i.e., $\lambda > \mu$, the parametric form of the non-analytic contribution from the stationary phase analysis is in good agreement with the full analytic form. The small discrepancy can be traced to the contributions from other vertices that we did not take into account, especially the mixing vertex with coefficient β_1.

Having confirmed the validity of our approach, we now study the size of NG for various values of λ as shown in figure 2.3. The NG is plotted for a generic value of $c = 0.5$, as the plots for other values look similar due to the subdominant dependence of NG on parameter c. Some notable features in this plot are:

- The most important result is that we obtain an observable NG for a large range of physical masses with a high reach, $H_{\text{inf}} < M_{\text{eff}} \lesssim \lambda$ ($\lesssim 60 H_{\text{inf}}$).[9] Note that this corresponds to an equally large range in "bare" mass parameter M^2 (which dominates after inflation), where for any value of c, an usuppressed signal can be obtained for $-(1-c)\lambda^2 < M^2 < c\lambda^2$.

- The non-analytic component of NG has a weak dependence on M_{eff}, which gives a plateau-like behavior in $|f_{\text{oscil}}|$ for $M_{\text{eff}} < \lambda$. The signal peaks at $M_{\text{eff}} \simeq \lambda$ due to the resonance behaviour. After that, the exponential suppression kicks in, Eq. (2.64), and the signal drops as $|f_{\text{oscil}}| \sim e^{-\pi(\mu-\lambda)}$.

It is useful to understand how our results for the scalar chemical potential compare to a chemical potential for a heavy fermionic field (see e.g. [26]). The analogy is closest when we restrict to $c = 0$ and $M^2 > 0$, in which case, $M_{\text{eff}} = \sqrt{M^2 + \lambda^2} > \lambda$ so that the signal is always exponentially suppressed. We can approximate the suppression factor of Eq. (2.64) for small M as $e^{-\pi(\mu-\lambda)} \approx e^{-\pi M^2/2\lambda}$, as appears in the case of fermionic chemical potential. We then see that in this regime, the mass range is limited to $0 < M \simeq \sqrt{\lambda}$.

We also demonstrate the oscillatory behavior of the NG signal for benchmark points: $\lambda = 40 H_{\text{inf}}$ and $M_{\text{eff}} = 5 H_{\text{inf}}, 28.7 H_{\text{inf}}$ in figure 2.4. The parameter c affects the frequency of oscillation by modifying M_{eff} as expected. Also, notice that the amplitude of the oscillations

[9] By observable, we mean $f_{\text{NL}} \gtrsim O(0.01)$, as explained in section 2.2.

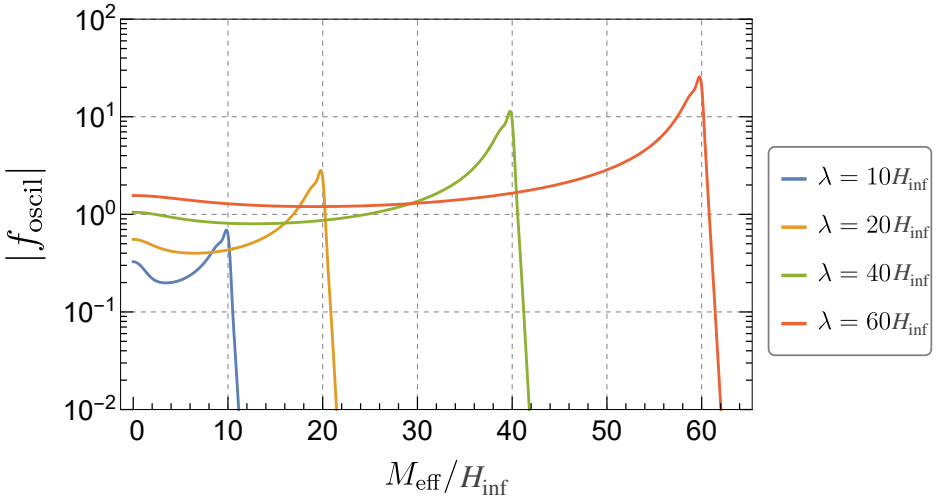

Figure 2.3: Amplitude of the non-analytic contribution $|f_{\rm oscil}|$ from the full calculation in Appendix A.2, plotted against the physical mass $M_{\rm eff}$ of the complex scalar in Hubble units for $c = 0.5$ and various values of the chemical potential $\lambda = 10H_{\rm inf}$ (blue), $20H_{\rm inf}$ (yellow), $40H_{\rm inf}$ (green), and $60H_{\rm inf}$ (red). We take $\alpha/\Lambda = 0.1\lambda$. The expression for NG has a subdominant dependence on the parameter c, and hence we only show a representative plot for a generic value $c = 0.5$. Note that the range $0 < M_{\rm eff} \lesssim \lambda$ corresponds to $-\lambda^2/2 < M^2 \lesssim \lambda^2/2$ for the "bare" mass. The tachyonic regime for M (as opposed to $M_{\rm eff}$), $M^2 < 0$, corresponds to a post-inflationary instability to generating a significant σ background. During inflation, this instability is absent in the regime of non-tachyonic de Sitter mass $M_{\rm eff}$ plotted. No fine-tuning of parameters is needed to obtain the large signals shown.

has a small dependence on the ratio k_1/k_3, which can be used to infer $M_{\rm eff}$, as we will see in section 2.5.

In conclusion, we have demonstrated an enhanced NG signal for heavy complex scalar fields with chemical potential for a wide range of parameter space as seen in figure 2.3. The NG is at tree level and hence, the calculation is robust and much simpler than the loop-level processes previously considered in the context of chemical potentials. In figure 2.4, we see that the signal has a distinct oscillatory signature with many observable oscillations before the $p^{-3/2}$ dilution takes over (this dilution is however factored out on the vertical axis in figure 2.4).

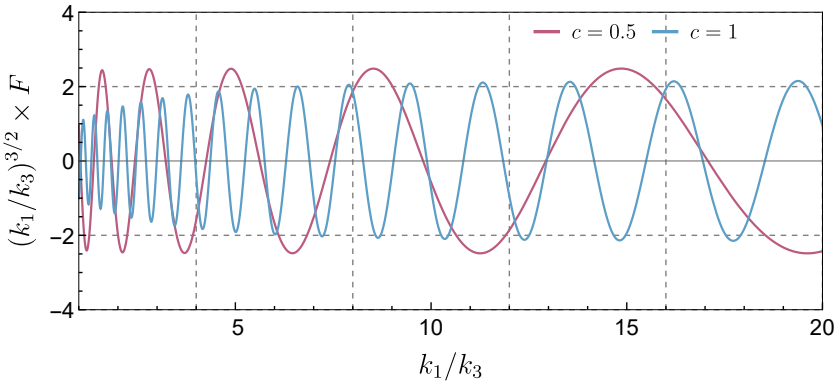

Figure 2.4: The oscillatory signal as a function of the momentum ratio k_1/k_3 for $M = 5H_{\rm inf}$ and $\lambda = 40H_{\rm inf}$. The two different curves correspond to $c = 0.5$ or $M_{\rm eff} \simeq 28.7H_{\rm inf}$ (purple) and $c = 1$ or $M_{\rm eff} = 5H_{\rm inf}$ (blue).

2.4.4 Sub-dominant contribution: I_{++} diagrams

In this section, we go through the calculation of I_{++} diagram to convince the reader that it is indeed exponentially suppressed. Taking the same vertices as for the I_{+-} diagram in section 2.4.1, we write the I_{++} contribution

$$I_{++} \supset (-i)(-i)\int \frac{d\eta_1}{\eta_1^4}\int \frac{d\eta_2}{\eta_2^4}\,\tilde{d}_+(k_1,k_2;\eta_1)d_+(k_3;\eta_2)\times \\ \left\{\beta_2\rho_2^*\left(\frac{\eta_2}{\eta_1}\right)^{i\lambda}F_{++}(k_3;\eta_1,\eta_2)+\beta_2^*\rho_2\left(\frac{\eta_2}{\eta_1}\right)^{-i\lambda}G_{++}(k_3;\eta_1,\eta_2)\right\}. \tag{2.81}$$

There is a time-ordering issue in I_{++}/I_{--} diagrams. But the time scales of the dominant contribution are well separated and thus the integrals can be extended to the entire domain of integration. From the previous calculation of I_{+-} diagrams (we will check for consistency later in the calculation), the integral at k_3 is dominated by earlier time as compared to the integral at k_{12}. This simplifies the time ordering. We focus on the part with F_{++} propagator which corresponds

to figure 2.1 (b).

$$I_{++} \supset -\beta_2\,\rho_2^*\,\langle\,\delta\phi_0^3\cdot\left\{\int_{\eta_1=0}^{\infty}(\delta\phi)^2\,\delta\tilde{\sigma}^\dagger(-\eta_1)^{-i\lambda}\int_{\eta_2=0}^{\infty}\delta\phi\delta\tilde{\sigma}(-\eta_2)^{i\lambda})\right\}\rangle$$
$$\sim -\beta_2\,\rho_2^*\,\tilde{I}^{(+)}_{k_{12}}\tilde{I}^{(+)}_{k_3}, \tag{2.82}$$

where tilde denotes integrals in I_{++}/I_{--} diagrams. $\tilde{I}^{(+)}_{k_3}$ is dominated by the contribution from stationary point at $-k_3\eta_2 \equiv x_* \sim (\lambda^2-\mu^2)/(2\lambda)$, and it can be evaluated using a similar procedure used to get Eq. (2.63),

$$\tilde{I}^{(+)}_{k_3} \sim \frac{\sqrt{\pi}}{k_3^{3/2+i\lambda}}e^{-i\delta(\lambda,\mu)}\lambda^{1/2}(\lambda^2-\mu^2)^{-1}. \tag{2.83}$$

The integral at k_{12} vertex on the other hand does not have a stationary point in the domain of integration for $\lambda > \mu$.

$$\tilde{I}^{(+)}_{k_{12}} \sim \frac{1}{4\sqrt{2}k_1^3k_2^3k_3^{-3/2-i\lambda}}\int_0^\infty dx\frac{x^{-5/2}(1+ipx/2)^2}{(x^2+\mu^2)^{1/4}}\,e^{i\tilde{h}(x)} \tag{2.84}$$

$$\text{where}\quad \tilde{h}(x) = -\lambda\log(x) - px + \int^x\sqrt{1+\frac{\mu^2}{x^2}}dx. \tag{2.85}$$

Then $\tilde{h}'(x) = -\frac{\lambda}{x} - p + \sqrt{1+\frac{\mu^2}{x^2}}$ is never zero for $x > 0$ and $\lambda > \mu$. To evaluate this integral, we instead perform a Wick rotation $x \to -ix$. Then the phase factor e^{-ipx} becomes an exponential e^{-px} which gives contribution in the region $x < 1/p$. This justifies the time-ordering. Since

$p > 1$, we can take the late time limit of the adiabatic mode function which goes as $x^{i\mu}$,

$$\begin{aligned}\tilde{I}^{(+)}_{k_{12}} &\sim \frac{(-i)^{-3/2}}{4\sqrt{2}k_1^3k_2^3k_3^{-3/2+i\lambda}}\mu^{-1/2}(-i)^{-i(\lambda-\mu)}\int_0^\infty dx x^{-5/2}\left(1-\frac{px}{2}\right)^2 x^{-i(\lambda-\mu)}e^{-px} \\ &\sim \frac{(-i)^{-3/2}}{4\sqrt{2}k_1^3k_2^3k_3^{-3/2+i\lambda}}\left(\frac{p}{2}\right)^2\mu^{-1/2}e^{-\pi(\lambda-\mu)/2}\,\Gamma\left(\frac{1}{2}-i(\lambda-\mu)\right)p^{-1/2+i(\lambda-\mu)}. \end{aligned} \tag{2.86}$$

Here we have only kept the largest contribution. Taking asymptotic expression for gamma function, $\Gamma(x+iy) \xrightarrow{y\to\infty} \sqrt{2\pi}|y|^{x-1/2}e^{-\pi|y|/2}$, we simplify above expression

$$\tilde{I}^{(+)}_{k_{12}} \sim \frac{\sqrt{\pi}}{16k_1^3k_2^3k_3^{-3/2+i\lambda}}\mu^{-1/2}e^{-\pi(\lambda-\mu)}p^{3/2+i(\lambda-\mu)}. \tag{2.87}$$

Combining eqs. (2.83) and (2.87),

$$I_{++} \supset -\beta_2\,\rho_2^*\,\tilde{I}^{(+)}_{k_{12}}\tilde{I}^{(+)}_{k_3} \sim -\frac{\pi\beta_2\rho_2^*}{16k_1^3k_2^3}\,\mu^{-1/2}\lambda^{1/2}(\lambda^2-\mu^2)^{-1}\,e^{-\pi(\lambda-\mu)}\,p^{3/2+i(\mu-\lambda)}. \tag{2.88}$$

In the regime where $\lambda < \mu$, we still get the suppression $e^{-\pi|\mu-\lambda|}$ but from the k_3 vertex instead. We see that I_{++} is generally sub-dominant to I_{+-} by a factor of $e^{-\pi|\mu-\lambda|}$, and only contributes significantly in a small region when M_{eff} is close to λ.

2.4.5 Symmetry breaking mass term

Until now, we have considered a linear symmetry-breaking term for the complex scalar. However, we can consider a more general derivative coupling of the inflaton to the scalar fields as discussed in Eq. (2.5), which can be mapped to a quadratic $\sigma\sigma$-type mass correction. Starting

with the form in Eq. (2.6),

$$\mathcal{L}_{\text{int}} \supset -(\lambda_1 \dot{\sigma}_1 \sigma_2 - \lambda_2 \dot{\sigma}_2 \sigma_1), \tag{2.89}$$

let us write this in terms of a complex scalar $\sigma = \sigma_1 + i\sigma_2$,

$$\mathcal{L}_{\text{int}} \supset \left\{ \frac{i(\lambda_2 + \lambda_1)}{4} \left(\dot{\sigma}^\dagger \sigma - \dot{\sigma} \sigma^\dagger \right) + \frac{i(\lambda_2 - \lambda_1)}{4} \left(\dot{\sigma}^\dagger \sigma^\dagger - \dot{\sigma} \sigma \right) \right\}. \tag{2.90}$$

Notice that the first term is a chemical potential $\sim \lambda J^0$. The second term represents the extent of symmetry-breaking and is $\propto (\lambda_2 - \lambda_1)$ as expected. It can be simplified to a symmetry-breaking mass correction using integration by parts, and then rotating the complex field $\sigma \to e^{-i\pi/4}\sigma$ to get rid of the extra phase factors,

$$\mathcal{L}_{\text{int}} \supset \left\{ \frac{i(\lambda_2 + \lambda_1)}{4} \left(\dot{\sigma}^\dagger \sigma - \dot{\sigma} \sigma^\dagger \right) + \frac{3(\lambda_2 - \lambda_1)}{8} \left(\sigma^\dagger \sigma^\dagger + \sigma \sigma \right) \right\}. \tag{2.91}$$

In the presence of a Z_2-symmetry $\sigma \to -\sigma$, this constitutes the leading $U(1)$-breaking. It is also roughly analogous to the studies of chemical potential in fermions, which is another motivation to study its effects in greater detail.

The above considerations give rise to a Lagrangian similar to Eq. (2.23) but with a quadratic symmetry-breaking $m^2\sigma^2$ instead,

$$\begin{aligned} \mathcal{L}_\sigma = \sqrt{-g} \{ & -|\partial\sigma|^2 - M^2|\sigma|^2 \\ & - \frac{i\partial_\mu \phi}{\Lambda} \left(\sigma \partial^\mu \sigma^\dagger - \sigma^\dagger \partial^\mu \sigma \right) - \frac{c\,(\partial\phi)^2}{\Lambda^2} |\sigma|^2 - \frac{m^2}{2} \left(\sigma\sigma + \sigma^\dagger \sigma^\dagger \right) \Big\} \,. \end{aligned} \tag{2.92}$$

Then after the usual field redefinition $\sigma = e^{-i\phi/\Lambda}\tilde{\sigma}$, we get

$$\mathcal{L}_\sigma = \sqrt{-g}\Big\{ -|\partial\tilde{\sigma}|^2 - M^2|\tilde{\sigma}|^2 \\ +(1-c)\,\frac{(\partial\phi)^2}{\Lambda^2}|\tilde{\sigma}|^2 - \frac{m^2}{2}\left(\tilde{\sigma}\tilde{\sigma}\, e^{-2i\phi/\Lambda} + \tilde{\sigma}^\dagger\tilde{\sigma}^\dagger\, e^{2i\phi/\Lambda}\right)\Big\}. \tag{2.93}$$

We work in the regime $H_{\rm inf} < m \ll M_{\rm eff}$ ($M_{\rm eff} = \sqrt{M^2 + (1-c)\lambda^2}$) such that the symmetry-breaking does not lead to explosive particle production. The EOM can be written as,

$$\partial_\eta^2\,\tilde{\sigma} - \frac{2}{\eta}\,\partial_\eta\tilde{\sigma} + \left(k^2 + \frac{M_{\rm eff}^2}{\eta^2}\right)\tilde{\sigma} + \frac{m^2}{\eta^2}\tilde{\sigma}^\dagger(-\eta)^{-2i\lambda} \;=\; 0. \tag{2.94}$$

Notice that the EOM for σ and $\sigma^\dagger$ are coupled due to the symmetry-breaking mass correction. The diagonalization of non-derivative terms will involve a time-dependent unitary matrix with factors $\propto (-\eta)^{\pm i\lambda}$ from the symmetry-breaking mass correction. This will induce off-diagonal elements from the derivative terms in EOM. Invariably, factors of $(\eta)^{\pm i\lambda}$ can not be removed, which is the source for particle production.

Eq. (2.94) is similar to narrow parametric resonance with a high frequency mass correction. To get some intuition about the effect of m, consider a simplified EOM for some real scalar field $\overline{\sigma}$ motivated by Eq. (2.94),

$$\partial_\eta^2\,\overline{\sigma} - \frac{2}{\eta}\,\partial_\eta\overline{\sigma} + \left(k^2 + \frac{M_{\rm eff}^2}{\eta^2}\right)\overline{\sigma} + \frac{m^2}{\eta^2}\cos(2\lambda t)\overline{\sigma} \;=\; 0. \tag{2.95}$$

Given that we will focus on a regime $\lambda > M_{\rm eff} \gg m > H_{\rm inf}$, we will treat the expansion of spacetime adiabatically compared to particle production. We expect a resonance-like behavior

when the frequency of the source $\sim 2\lambda$ is twice the natural frequency of the complex scalar, i.e., when $\omega(\eta_*) \sim \lambda/\eta_*$ in conformal time. Then the condition for resonance is,

$$\sqrt{\frac{k^2}{a_{\rm res}^2} + M_{\rm eff}^2} = \lambda, \tag{2.96}$$

and it lasts for the duration when the frequency is inside a resonance band. We only consider the first resonance band, where the amplification is the largest [56]:

$$\lambda\left(1 - \frac{m^2}{2\lambda^2}\right) \leq \sqrt{k^2/a^2 + M_{\rm eff}^2} \leq \lambda\left(1 + \frac{m^2}{2\lambda^2}\right). \tag{2.97}$$

This gives time interval of resonance to be,

$$\delta t \sim \frac{m^2}{(\lambda^2 - M_{\rm eff}^2)}. \tag{2.98}$$

Then the amplification factor can be evaluated to be

$$e^{\frac{m^4}{\lambda(\lambda^2 - M_{\rm eff}^2)}} \sim 1 + \mathcal{O}(m^4/\lambda^3). \tag{2.99}$$

We see that the resonance occurs for a very short duration and hence the amplification is small $\sim \mathcal{O}(m^4/\lambda^3)$. This is expected since the physical momentum dilutes exponentially fast. Above analysis indicates that if we work in the regime where the amplification is small, i.e., $m^4/\lambda^3 \ll 1$, the symmetry-breaking term can be considered as a perturbation. We can then treat it as a Feynman vertex in the "insertion" approximation, while the propagators of the free fields are unchanged. In the following, we estimate its contribution to the bispectrum.

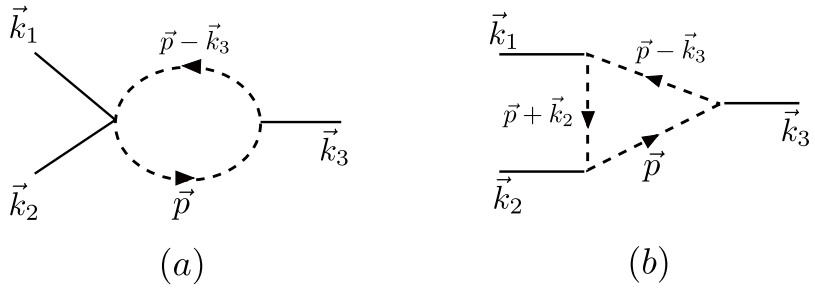

Figure 2.5: Loop-level contribution to the bispectrum from $m^2\tilde{\sigma}^2$-type symmetry breaking. The solid lines correspond to inflaton propagators, while dashed lines to complex scalar propagators.

The contributions to the bispectrum come from diagrams in figure 2.5. The full loop calculation is generally quite challenging, but it can be simplified in certain regimes. In the squeezed limit, the non-analytic signature is prominent when both $\tilde{\sigma}$-modes at the k_3 vertex are soft $\sim k_3$. Then the loop integral can be approximated as

$$\int d^3p \approx k_3^3. \tag{2.100}$$

With this simplification, the contribution to the bispectrum can be estimated using similar methods as in section 2.4.1 (except now we have two $\tilde{\sigma}$ modes at each vertex and an explicit time-dependence of the form $(-\eta)^{\pm 2i\lambda}$),

$$F_{\text{squeezed}} \sim \frac{1}{16\pi^2}\frac{\dot{\phi}_0}{\Lambda}\left(\frac{m^2}{\Lambda}\right)^2 \lambda\, \mu^{-1} p^{-3+2i(\mu-\lambda)}, \tag{2.101}$$

where we have included the loop factor $1/16\pi^2$. For $\Lambda, \mu \sim \mathcal{O}(\lambda)$, this expression can be simplified as

$$F_{\text{squeezed}} \sim \frac{1}{16\pi^2}\left(\frac{m^4}{\lambda^3}\right)\lambda^2\, p^{-3+2i(\mu-\lambda)}. \tag{2.102}$$

Notice that here the non-analytic signal dilutes faster $\sim p^{-3}$ as compared to the case of symmetry-breaking linear term, while the non-analytic exponent is twice as large. This is the feature of the contribution being at loop level. The interaction will also modify the power spectrum, which can be expected to be $\sim \mathcal{O}(m^4/\lambda^3)$. Then to ensure only a percent level correction to the power spectrum, we require $(m^4/\lambda^3) \lesssim 10^{-2}$. Using this constraint, $|f_{\rm oscil}|$ can be estimated as,

$$|f_{\rm oscil}| \sim 10^{-2}\frac{\lambda^2}{16\pi^2} \xrightarrow{\lambda\sim(10-60)H} \mathcal{O}(10^{-2}-10^{-1}). \tag{2.103}$$

We see that the non-analytic contribution from $m^2\sigma^2$-type symmetry breaking term is generically somewhat smaller compared to the case of linear symmetry-breaking model as discussed in section 2.4.3. While the contribution is small, it could still be within the sensitivity of future experiments. Also, this could be the sole contribution if an additional Z_2-symmetry is imposed on the complex scalar field. One may also consider the parameter regime where the amplification is large and must be included at leading order. We leave a more detailed study of this model to future work.

2.5 Inferring effective mass from the bispectrum

In the cosmological collider physics program, the non-analytic exponent of $p\,(=\,k_{12}/k_3)$ in the squeezed limit allows spectroscopy of heavy fields as seen in Eq. (2.1). In our case, the dominant contribution to NG has a non-analytic behavior of the form $\sim p^{-3/2\pm i(\mu-\lambda)}$ as seen in Eq. (2.78), which means an independent measurement of λ is needed to infer the effective mass of the heavy field. In this section, we outline one such procedure which can be used to effectively extract the effective mass and the chemical potential in a certain parameter regime by observing

the change in the non-analytic exponent as a function of the squeezing parameter p.

Till now, we have been taking the squeezed limit where $p \gg 1$, but there is another interesting region when $\lambda \gg p,\ \mu$. To get the parametric form of the bispectrum in this regime, we will have to use the following asymptotic form of the hypergeometric function [57],

$$ {}_2F_1\left(a+\gamma, b+\gamma, c+\gamma; z\right) \xrightarrow{\gamma\to\infty} \frac{\Gamma(c+\gamma)}{\Gamma(b+\gamma)}\left(\sum_{s=0}^{\infty} f_s(z)\,\frac{(b)_s}{\gamma^{c-b+s}}\right)(1-z)^{(c-a-b-\gamma)}. \tag{2.104} $$

Using this asymptotic form in the analytic expression for the bispectrum (see Appendix A.2 for details), we can get the non-analytic dependence on p in the large λ limit,

$$ {}_2F_1\left(\underbrace{r\pm i\mu}_{a}\pm i\lambda, \underbrace{r\mp i\mu}_{b}\pm i\lambda, \underbrace{r+1/2}_{c}\pm i\lambda; (1-p)/2\right) \overset{\lambda\to\infty}{\propto} \left(\frac{1+p}{2}\right)^{1/2-r\mp i\lambda}, \tag{2.105} $$

where r is some rational number that depends on the specific interaction. The takeaway is that the asymptotic form in the limit $\lambda \gg p,\ \mu$ is different than the squeezed limit, and the non-analyticity has the form $(1+p)^{\pm i\lambda}$.

This can also be seen from our approximate stationary phase analysis from earlier. For $\lambda > \mu p$, the production at k_{12} vertex occurs much earlier when the frequency of the complex scalar is dominated by the physical momentum rather than its mass. Hence, the non-analytic part can not capture the information about M_{eff}, and hence, it is expected to only depend on λ.

In summary, when $\lambda > \mu p$, we expect the non-analytic dependence $\sim (1+p)^{\pm i\lambda}$, and in large p limit, i.e., $\lambda < \mu p$, we expect the non-analyticity of the form $\sim p^{\pm i(\mu-\lambda)}$. In figure 2.6 (a), we see that the full analytic form (blue) agrees with the large λ approximation (yellow) for small values of p. In the squeezed limit on the other hand, the analytic form matches the large p

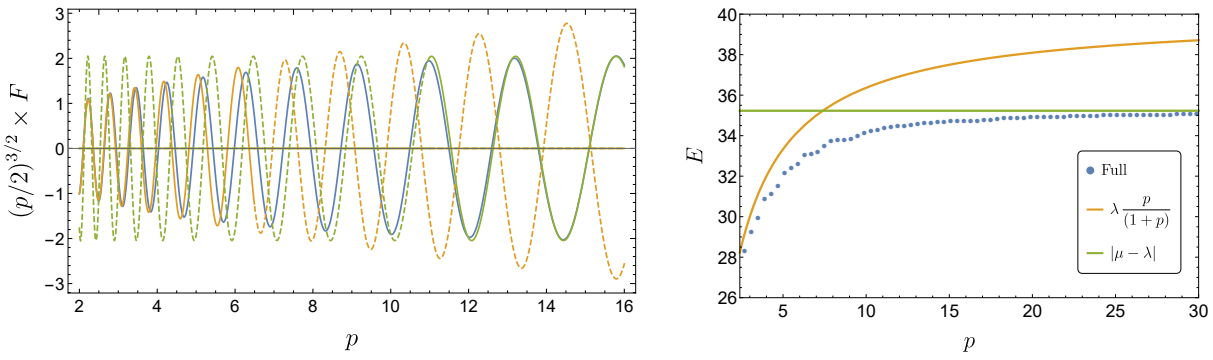

(a) (b)

Figure 2.6: Comparison of the full analytic form evaluated in Appendix A.2 (blue) to the large λ approximation (yellow) and large p approximation (green) for $M_{\text{eff}} = 5H_{\text{inf}}$ and $\lambda = 40H_{\text{inf}}$, using (a) the oscillatory form of the dimensionless NG function F and (b) the non-analytic exponent E. We clearly see that as the degree of squeezing is changed the full bispectrum switches between the above two approximations.

approximation (green). This corroborates our expectation from the previous discussion.

To extract the effective mass, we can look at the non-analytic exponent as a function of the degree of squeezing. For this purpose, we define a function E such that

$$E = \text{envelope of } (p)\partial_p \left(p^{3/2}F(k_1,k_2,k_3)\right) / \text{envelope of } \left(p^{3/2}F(k_1,k_2,k_3)\right) \tag{2.106}$$

$$= \begin{cases} \lambda \dfrac{p}{(1+p)} & \text{if } \lambda > \mu p \\ |\mu - \lambda| & \text{if } \lambda < \mu p. \end{cases} \tag{2.107}$$

Then E is effectively the non-analytic exponent. From figure 2.6 (b), we see that it also agrees well with our expectation. Using this feature, we can extract $\mu = \sqrt{M_{\text{eff}}^2 - 9/4}$ (and hence M_{eff}) as well as the chemical potential λ. This procedure is more efficient for c close to 1, i.e, the case of pure chemical potential. It becomes harder to extract the effective mass if $c \ll 1$, when $\mu \sim O(\lambda)$, and we are effectively always in the large p limit.

2.6 Conclusions

In this chapter, we have shown that a derivative coupling of the inflaton to heavy scalar fields of "chemical potential" type can lead to unsuppressed production of heavy particles and leave observable imprints in primordial non-Gaussianities. In particular, the chemical potential can overturn the Boltzmann suppression for masses far above the inflationary Hubble scale $H_{\rm inf}$, ordinarily present in cosmological particle production. This effect is quite general, requiring only two (or more) real scalar fields where the symmetry rotating one into the other is broken. In essence, the unsuppressed particle production above $H_{\rm inf}$ draws on the large kinetic energy of the inflaton background, $\dot{\phi}_0 \sim (60H_{\rm inf})^2$. A heavy mass reach up to $\sim 60H_{\rm inf}$ can thereby be accomplished while still remaining within a controlled derivative expansion for the inflationary effective field theory. Signatures of such heavy masses could be observed in the bispectrum with strength $f_{\rm NL} \sim \mathcal{O}(0.01 - 10)$, within the sensitivity of upcoming LSS and future 21-cm experiments.

The main results of our analysis are summarized in figure 2.3 and figure 2.4. In our model, the contribution to the bispectrum is at tree-level, which removes the loop-suppression seen in earlier spin-1/2 and spin-1 chemical potential examples. Importantly, it also makes the calculations analytically tractable and physically transparent. We outlined a procedure to infer the effective mass of the heavy field, which relies on the variation in the non-analytic exponent of the co-moving momentum ratio (degree of "squeezing") as in figure 2.6.

It is straightforward to generalize our mechanism to more than one heavy complex scalar, each with its own distinct chemical potential λ, thereby allowing us to explore multiple "channels". More non-trivially, our mechanism can be extended to massive complex fields with arbi-

trary non-zero spins. The mechanism can also be extended to the curvaton paradigm [58–60] for inflation, which can exhibit new features. We will take up these generalizations in future work.

Chapter 3: Primordial Clocks within Gravitational Wave Anisotropies

3.1 Introduction

In section 1.3 of Chapter 1, we emphasized the importance of new cosmological observables that can potentially probe previously unexplored physics from the inflationary era. Gravitational waves produced in the early universe could provide such novel data sources. It was shown in Ref. [1] that a cosmological GWB[1] would necessarily exhibit fluctuations, or 'anisotropies', across the sky, analogously to the CMB. It was also pointed out that GWB fluctuations, however, could look very different in their detailed pattern than CMB fluctuations if they originate from an independent inflationary source of density perturbations. GWB anisotropies could therefore provide complementary information about inflation compared to the known maps of adiabatic perturbations.

In addition to being a new cosmological dataset, anisotropies in GWB could also in principle provide a more pristine and precise map of the primordial fluctuations. This is because in CMB, subhorizon modes, $k > k_{\rm CMB} \sim 30 k_{\rm today}$[2], are strongly modified by causal physics such as baryon acoustic oscillations and Silk damping [61, 62], while the superhorizon modes, $k < k_{\rm CMB}$, suffer from cosmic variance $\propto (k_{\rm today}/k)^{1/2}$. In GWB however, the corresponding

[1] Note that a cosmological GWB would necessarily be *stochastic* in nature. Individual events of gravitational wave production in cosmological sources cannot be resolved. We would therefore receive an incoherent superposition of gravitational waves from many events, giving rise to a stochastic signal.

[2] $k_{\rm today}$ is the comoving mode that is re-entering the horizon today, and is therefore the smallest observable mode.

dividing line could be at a much larger multipole, $k_{\rm GW} \sim (T_c/T_{\rm CMB})\, k_{\rm CMB} \sim 10^{14} k_{\rm today}$ for a GW source at a $T_c \sim$ TeV, providing a large k-range that can simultaneously have small cosmic variance and be relatively unmodified by subhorizon physics.

Given these striking properties of GWB anisotropies, we can ask what new physics might be revealed within GWB maps. In this chapter as well as the next one, we specifically consider GWB sourced by a first order phase transition (PT). This is because many extensions of the Standard Model (SM) motivated by the Electroweak Hierarchy Problem have PTs with critical temperatures $T_c \sim (1-1000)$ TeV. The GW spectrum from such a PT would then be redshifted to frequencies $\sim 10^{-3} - 10^{0}$ Hz today, which fortuitously is the target frequency range of proposed GW experiments such as LISA [37], MAGIS [63], TianQin [38], Taiji [39], BBO [40], DECIGO [41]. We therefore consider a PT in one such SM extension as the source of our GWB.

Some previous works exploring the potential of GWB maps include [1, 64–67]. We take inspiration from the work in Chapter 2 and consider a possibility of detection of very heavy fields in GWB through their "cosmological collider" signature. While the cosmological collider signature is typically expected within non-Gaussianity (NG), it could also occur in the power spectrum if the heavy field is excited classically, instead of quantum mechanically. This can be understood intuitively by considering the symmetries of the inflationary spacetime. If the classical inflationary background has (approximate) de Sitter geometry,

$$ds^2 = -dt^2 + a^2(t)\, d\vec{x}^2\,; \quad a(t) = e^{H_{\rm inf} t}\,, \tag{3.1}$$

its isometries include "scale invariance", $\vec{x} \to \lambda \vec{x}, H_{\rm inf} t \to H_{\rm inf} t - \ln \lambda$, where $H_{\rm inf}$ is the inflationary Hubble scale. This relates heavy particle propagation during inflation to spatial cor-

relations at the end of inflation, $e^{-iM(t-t')} \rightarrow (k'/k)^{-i(M/H_{\rm inf})}$, where $\vec{k}$ and $\vec{k}'$ are co-moving wave-vectors. Such a striking non-analytic signature sensitive to a heavy mass M can only be seen within NG (greater than two-point) correlators, so that there are at least two independent wave-vectors given the spatial translation invariance.

However, the requirement of NG can be evaded if the classical background contains a small breaking of scale invariance, which can occur if the heavy field is excited classically, instead of quantum mechanically as above. Sudden excitation of the heavy field at time t_0 breaks scale invariance, and the subsequent decay of this field into light quanta allows these scale-invariance-breaking features to be imprinted in two-point correlators, with a single co-moving wave-vector [68]. The heavy oscillations then give $\sim e^{-iM(t-t_0)} \rightarrow (k_0/k)^{-i(M/H_{\rm inf})}$, where k_0 is related to the co-moving mode that is exiting the horizon at t_0. Furthermore, while quantum production of heavy particles in NG is typically "Boltzmann"-suppressed $\sim e^{-\pi(M/H_{\rm inf})}$ (with some special mechanisms that can mitigate this to a limited extent [24, 26, 69–74], one of which is discussed in Chapter 2), this is not the case for heavy classical excitations. Such an oscillating heavy field has been dubbed a "primordial clock" (PC) in the context of testing inflation and alternate scenarios [75]. Here, we will restrict to the inflationary paradigm (with $\approx$ de Sitter geometry).

Such PCs have not been detected in the precision measurements of CMB by Planck [7, 11, 31], constraining the couplings of heavy fields to adiabatic perturbations, almost saturating the theoretical lower limit from cosmic variance in the low-multipole regime. Future probes of CMB polarization, Large Scale Structure (LSS), and 21-cm tomography are expected to improve sensitivity only at high multipoles [31, 76, 77]. PC features in the isocurvature component of GWB anisotropies, however, could be much larger if the coupling of heavy field to isocurvature fields is significant. We will show that a GWB map would then provide a striking alternate

channel for detecting heavy field dynamics during inflation.

We note that measuring a high-precision GWB map faces significant practical challenges in terms of detector sensitivity, angular resolution, and subtraction of astrophysical foregrounds. Various strategies have been proposed to make progress on these fronts [78–87]. If the monopole moment of any GWB is discovered in relatively near-term detectors like LISA, there will be strong motivation to build next-generation detectors capable of extracting the *guaranteed* anisotropies. In this way, we thus foresee a multi-stage discovery of GWB anisotropies, analogous to the history of CMB exploration.

The rest of the chapter is organised as follows: section 3.2 gives a brief review of the effects of a PC field on adiabatic fluctuations in single-field inflation. The discussion is then extended to multi-field inflation in section 3.3, where we describe a non-minimal reheating scenario that may result in a sizeable PC feature in isocurvature GWB. In section 3.4, we discuss observability in the context of two interesting benchmarks, and perform a broader analysis of the parameter space. Finally, we give an example of a smoother polynomial potential in section 3.5 that could excite the PC field, which is more realistic compared to the simplified sudden excitation approximation employed in previous sections. We conclude in section 3.6.

3.2 Primordial clocks in single-field inflation

We first review the effects of a PC field σ on adiabatic density perturbations seeded by the quantum fluctuations $\delta\phi$ of the inflaton field, as proposed in [68]. The initial condition for the classical motion is that it is restricted to slow-roll in the ϕ direction of field space, while the massive σ field is stuck at its origin. It is assumed that there is a feature in the scalar potential

that leads to a sudden transfer of energy to excite σ at time t_0, after which ϕ, however, continues to slow-roll. The classical dynamics of σ after t_0 is governed by the homogeneous equation of motion,

$$\partial_t^2\sigma + 3H_{\rm inf}\,\partial_t\sigma + M^2\sigma = 0\,, \tag{3.2}$$

where M is the mass of the σ field. In the limit $M \gg H_{\rm inf}$, the solution has an oscillatory form,

$$\sigma_{\rm osc}(t) \simeq \theta(t-t_0)\,\sigma_0\left(\frac{a(t)}{a(t_0)}\right)^{-3/2}\cos[M(t-t_0)]\,. \tag{3.3}$$

The oscillating field energy in an inflationary background imparts a small oscillatory correction to the Hubble constant,

$$\Delta H_{\rm osc} \approx \theta(t-t_0)\frac{\sigma_0^2 M}{8M_{\rm Pl}^2}\left(\frac{a(t)}{a(t_0)}\right)^{-3}\cos[2M(t-t_0)]\,, \tag{3.4}$$

where $M_{\rm Pl}$ is the reduced Planck scale. This in turn imparts an oscillatory component to the slow-roll parameters, $\Delta\epsilon_{\rm osc} = -\partial_t(\Delta H_{\rm osc})/H_{\rm inf}^2$ and $\Delta\eta_{\rm osc} \approx \partial_t(\Delta\epsilon_{\rm osc})/(H_{\rm inf}\epsilon)$. Here $H_{\rm inf}$ and ϵ are the unperturbed parameters in the absence of σ oscillations.

These oscillatory components then introduce scale-invariance-breaking features in the power spectrum of adiabatic perturbations, $\mathcal{P}_{\zeta_\phi}$, defined as

$$\langle\,\zeta_\phi(\vec{k})\zeta_\phi(\vec{k}')\,\rangle \equiv (2\pi)^3\delta(\vec{k}+\vec{k}')\mathcal{P}_{\zeta_\phi}(k)\,, \tag{3.5}$$

where ζ_ϕ are the gauge-invariant perturbations capturing $\delta\phi$, as measured in the primordial fluctu-

ations of the CMB and LSS. If the features are small, the power spectrum can be broken down as $\mathcal{P}_{\zeta_\phi} = \mathcal{P}^{(0)}_{\zeta_\phi} + \Delta\mathcal{P}_{\zeta_\phi}$, where $\mathcal{P}^{(0)} \propto 1/k^3$ denotes the dominant unperturbed scale-invariant spectrum while $\Delta\mathcal{P}^{(0)}$ denotes the contribution from PC. This *irreducible* contribution from $\Delta H_{\rm osc}$ is predominantly given by

$$\frac{\left(\Delta\mathcal{P}_{\zeta_\phi}\right)_{\Delta H_{\rm osc}}}{\mathcal{P}^{(0)}_{\zeta_\phi}} \simeq \theta(k-k_g)\,\frac{\sqrt{\pi}}{2}\frac{(M^2\sigma_0^2)}{\dot\phi_0^2}\left(\frac{M}{H_{\rm inf}}\right)^{1/2}\left(\frac{k}{k_g}\right)^{-3}\cos\left[\frac{2M}{H_{\rm inf}}\log\frac{k}{k_g}\right]. \tag{3.6}$$

We can understand the key features of this calculation intuitively, by noting that ordinarily $\mathcal{P}_{\zeta_\phi} \propto 1/\epsilon$, so that we expect roughly $\Delta\mathcal{P}_{\zeta_\phi}/\mathcal{P}^{(0)}_{\zeta_\phi} \propto \Delta\epsilon_{\rm osc}/\epsilon$. Now, $\Delta\epsilon_{\rm osc}(t)$ represents a high-frequency ($2M$ by Eq. (3.4)) gravitational source for production of inflaton pairs, so their physical momentum on production, $ke^{-H_{\rm inf}t} \approx M$, by the local Minkowski energy conservation. The softest co-moving momentum k_g produced from this gravitational source is given by $k_g e^{-H_{\rm inf}t_0} \approx M$. Solving for t, t_0 in terms of k, k_g results in the dependence on the latter seen in Eq. (3.6).

Similarly, $\Delta\eta_{\rm osc}$ gives the dominant irreducible PC contribution to the 3-point correlators, which are typically written in the following normalized form:

$$F \equiv \frac{5}{6}\frac{\langle\,\zeta_\phi(\vec{k}_1)\zeta_\phi(\vec{k}_2)\zeta_\phi(\vec{k}_3)\,\rangle}{\mathcal{P}_{\zeta_\phi}(k_1)\mathcal{P}_{\zeta_\phi}(k_2) + (k_1\to k_3) + (k_2\to k_3)}\,. \tag{3.7}$$

In the equilateral triangle configuration $k_1 \sim k_2 \sim k_3$,

$$F_{\Delta H_{\rm osc}} \simeq \theta(K-2k_g)\,f_{\rm NL}^{\rm PC}\left(\frac{K}{2k_g}\right)^{-3}\cos\left[2\frac{M}{H_{\rm inf}}\log\frac{K}{2k_g}\right], \tag{3.8}$$

where $K = \sum_{i=1}^3 |\vec{k}_i|$, and the amplitude of NG is $f_{\rm NL}^{\rm PC} \sim \frac{10}{9}\frac{\sqrt{\pi}}{4}\frac{(M^2\sigma_0^2)}{\dot\phi_0^2}\left(\frac{M}{H_{\rm inf}}\right)^{5/2}$.

Apart from these irreducible contributions, the coherent σ field may also directly decay

to inflaton fluctuations. Consider the lowest dimensional interaction consistent with an (approximate) inflaton shift-symmetry, $\mathcal{L}_{\rm int} \sim (\sigma\, \partial_\mu\phi\partial^\mu\phi)/\Lambda_\phi$. The PC contribution to $\mathcal{P}_{\zeta_\phi}$ from the decay of $\sigma_{\rm osc}$ through this interaction can be evaluated using the in-in formalism [10–12], which is reviewed in 1.1.2. This gives

$$\frac{\left(\Delta\mathcal{P}_{\zeta_\phi}\right)_{\rm dec}}{\mathcal{P}^{(0)}_{\zeta_\phi}} \simeq \theta(k-k_d)\,\sqrt{2\pi}\,\frac{\sigma_0}{\Lambda_\phi}\left(\frac{M}{H_{\rm inf}}\right)^{1/2}\left(\frac{k}{k_d}\right)^{-3/2}\cos\left[\frac{M}{H_{\rm inf}}\log\frac{k}{k_d}\right]. \tag{3.9}$$

Here, $\sigma_{\rm osc}$ directly acts as a high-frequency (M from Eq. (3.3)) source for inflaton production instead of the irreducible gravitational source $\Delta H_{\rm osc}$. Therefore, the k-dependence can be obtained using a similar argument given for Eq. (3.6). With this source, a co-moving mode k is produced when $ke^{-H_{\rm inf}t} \approx M/2$. The softest such mode produced through direct decay is then $k_d e^{-H_{\rm inf}t_0} = M/2$. Since the interaction is linear in σ, the contribution in Eq. (3.9) matter-dilutes $\propto k^{-3/2}$, as compared to the $\propto k^{-3}$ dependence in Eq. (3.6).

Such PCs have been searched for in the Planck CMB data (see e.g. analysis in [11, 31]). While there are potential candidates, none are statistically significant. In the low to medium k-range, the constraints on the amplitudes of PC features in adiabatic perturbations are close to the ultimate cosmic variance limit, while the future probes are expected to improve sensitivity only at high k (small scales) [31, 76, 77]. The PCs could be undetectable if σ_0 is small, or, for the direct decay contribution, if Λ_ϕ is large. Considering the valuable information encoded in the PC features, we ask if they can be probed by other cosmological observables.[3]

[3]Refs. [88, 89] have also studied PC-like scale-invariance-breaking features in scalar-induced GWB. There are however important qualitative differences: 1) They consider features that appear at very small scales, which can not be probed by CMB as they are highly Silk-damped. In our work, PC occurs on scales at which the CMB is undamped, but are too small there for detection. 2) Their features appear in the *frequency* spectrum of GWB, unlike in the anisotropies in our case.

3.3 Primordial clocks in gravitational waves with isocurvature

In the following, we study one such possibility where the excited σ field decays dominantly to another light "spectator" field, χ, present during inflation. If $m_\chi^2 \ll H_{\rm inf}^2$, it will develop an (approximately) scale-invariant spectrum, $\mathcal{P}^{(0)}_{\mathcal{S}_\chi} \propto 1/k^3$, similar to that of the inflaton. Here, $\mathcal{S}_\chi \equiv \zeta_\chi - \zeta_\phi$ is the isocurvature perturbation of χ, independent of the fluctuations of ζ_ϕ when the energy density in isocurvature is subdominant. To naturally maintain the lightness of χ, we again consider a shift-symmetric effective interaction of the form $\mathcal{L}_{\rm int} \sim (\sigma\, \partial_\mu\chi\partial^\mu\chi)/\Lambda_\chi$, $\Lambda_\chi \ll \Lambda_\phi$. This gives a PC feature $\Delta P_{\mathcal{S}_\chi}$, completely analogous to Eq. (3.9),[4]

$$\frac{\Delta\mathcal{P}_{\mathcal{S}_\chi}}{\mathcal{P}^{(0)}_{\mathcal{S}_\chi}} \simeq \theta(k-k_d)\,\alpha\left(\frac{k}{k_d}\right)^{-3/2}\cos\left[\frac{M}{H_{\rm inf}}\log\frac{k}{k_d}\right]$$
$$\text{where}\quad \alpha = \sqrt{\frac{2\pi M}{H_{\rm inf}}}\frac{\sigma_0}{\Lambda_\chi}\,. \tag{3.10}$$

There are some constraints on Λ_χ to ensure effective field theory (EFT) control. We require $(\sigma_0/\Lambda_\chi) < 1$ to keep the correction to the kinetic energy of χ small, and $(\dot\chi_0/\Lambda_\chi^2)$, $M/\Lambda_\chi < 1$ to ensure that no energy scales exceed the scale of non-renormalizability at which the EFT must break down. Here, χ_0 is the initial misaligned value of χ. The perturbative control of the in-in diagrams requires the PC feature to be small compared to the scale-invariant spectrum, giving a constraint $\alpha < 1$. We see qualitatively that it is possible to have small σ_0 and large Λ_ϕ so that PC feature is small in $\mathcal{P}_{\zeta_\phi}$, while σ_0/Λ_χ gives a sizeable PC contribution in $\mathcal{P}_{\mathcal{S}_\chi}$.

[4]The contribution to $\mathcal{P}_{\mathcal{S}_\chi}$ from $\Delta H_{\rm osc}$ is small, $(\Delta\mathcal{P}_{\mathcal{S}_\chi}/\mathcal{P}^{(0)}_{\mathcal{S}_\chi}) \propto (M^2\sigma_0^2)/(H_{\rm inf}^2 M_{\rm Pl}^2)$, and hence we only focus on the direct decay of σ to $\delta\chi$.

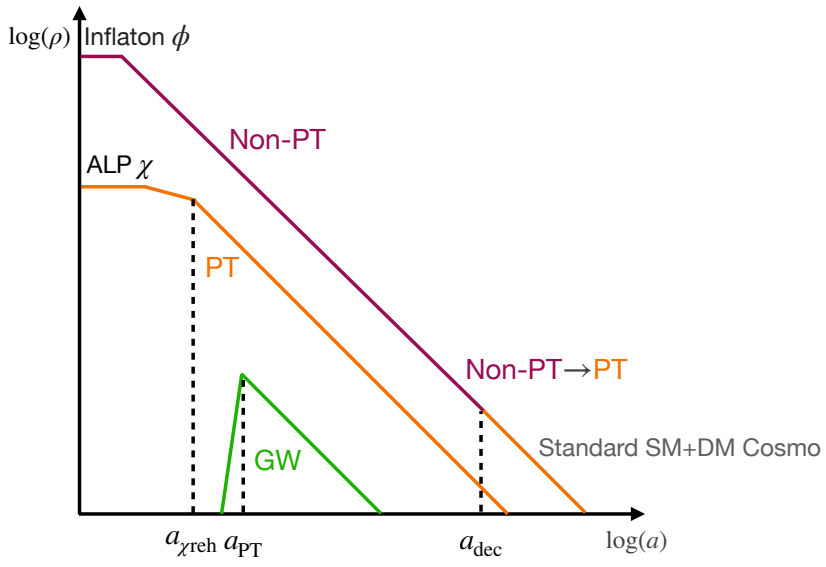

Figure 3.1: A schematic of the model with modified post-inflationary history showing energy densities in various sectors as a function of the scale factor (time).

3.3.1 A simple model of isocurvature GWB

We now illustrate how the primordial fluctuations of χ, including sizeable PC, may be probed by a potentially observable GWB. In this section, we review the model proposed in ref [1] that produces isocurvature GWB. Consider an additional light scalar field χ during inflation. It is taken to be initially misaligned from its minimum (taken to be at $\chi = 0$) to $\chi_0 \gg H_{\rm inf}$, where $H_{\rm inf}$ denotes the inflationary Hubble constant. Such a misalignment is robust as the field remains stuck due to the inflationary Hubble friction if its mass $m_\chi < H_{\rm inf}$. A well-motivated example of such a light field is an axion-like particle (ALP), which is a generic prediction of many BSM theories (see [90, 91]). During inflation, the energy density in χ, $V(\chi_0) \sim m_\chi^2 \chi_0^2$ is subdominant to that of the inflaton ϕ, which primarily drives inflation. After inflation, when the dropping Hubble constant matches m_χ, the χ field starts oscillating around its minimum and reheats some extension of the standard model (SM), including dark matter (DM), at $t_{\chi\rm reh}$. We

will assume that this extension of the SM undergoes a first-order phase transition (PT) in the multi-TeV range, capable of producing an observable GWB, as is known to take place in many explicit SM extensions (see [92, 93]). If the reheat temperature from χ decay is higher than the PT temperature, the decay products of χ will undergo this phase transition. We will therefore refer to this sector emerging from χ decay as the "PT sector".

The inflaton on the other hand is taken to reheat another sector that interacts very weakly with the PT sector and does not participate in the phase transition, henceforth referred to as the "non-PT sector". The non-PT sector is taken to decay to the SM + DM at $t_{\rm dec}$ sometime after the phase transition but before DM decoupling. In this way, after the decay there is a single SM+DM sector which dominantly originates from inflaton ϕ reheating, assuming that the PT sector is subdominant to the non-PT sector as depicted in figure 3.1. On the other hand, the GWB dominantly originates from χ reheating. Therefore it is possible for the fluctuations in GWB to be distinct from those in the SM+DM. The constraints from isocurvature and $N_{\rm eff}$ can be cast in terms of the ratio of energy density to critical density today as $\delta\Omega_{\rm GW}h^2 \lesssim 2\times10^{-11}$ and $\Omega_{\rm GW}h^2 \lesssim 2\times10^{-6}$, respectively. We will later show that our benchmarks easily satisfy these constraints.

The GW are sourced by sub-horizon physics at the time of PT, and hence the energy density fluctuations $\delta\rho_{\rm GW}$ on super-horizon scales are directly related to the initial fluctuations in the PT sector after it is reheated by χ (but before the non-PT sector decays into it),

$$\delta_{\rm GW} \sim \delta_{\rm PT} \sim \frac{\delta\chi}{\chi_0}\,, \tag{3.11}$$

where $\delta \equiv \delta\rho/\rho$. More precisely, the GW anisotropy can be written as [9, 67]

$$\delta_{\rm GW} = -\frac{4}{3}\zeta_\phi + 4\mathcal{S}_\chi\left(1 - \frac{4}{3}f_{\rm PT}\right) \approx 4\mathcal{S}_\chi\,, \tag{3.12}$$

where we consider $f_{\rm PT} \equiv \rho_{\rm PT}/\rho_{\rm total} \ll 1$ and $\mathcal{S}_\chi \gtrsim \zeta_\phi$.

The CMB anisotropies receive two independent contributions since the final fluctuations in the SM+DM are a combination of the decay products of the non-PT sector and the PT sector,

$$\delta_\gamma \sim \delta_{\rm npT} + f_{\rm PT}\delta_{\rm PT}\,, \tag{3.13}$$

where $\delta_{\rm nPT}$ is the fractional density perturbation in the non-PT sector. In terms of the independent gauge-invariant fluctuations,

$$\delta_\gamma \approx -\frac{4}{5}\zeta_\phi - \frac{4}{5}f_{\rm PT}\mathcal{S}_\chi. \tag{3.14}$$

We then see that GW map will be (mostly) uncorrelated with the CMB if $f_{\rm PT} \ll 1$. However, in addition to eqs. (3.6) and (3.8), $\mathcal{S}_\chi$ in Eq. (3.14) induces a small PC feature into adiabatic perturbations,

$$\frac{(\Delta\mathcal{P}_\gamma)_{\rm ind}}{\mathcal{P}_\gamma^{(0)}} \approx f_{\rm PT}^2\left(\frac{A_\chi}{A_\phi}\right)\left(\frac{\Delta\mathcal{P}_{\mathcal{S}_\chi}}{\mathcal{P}_{\mathcal{S}_\chi}^{(0)}}\right)\,, \tag{3.15}$$

where $\mathcal{P}_j^{(0)}(k) = 2\pi^2 A_j k^{-3}$ and $A_\phi \approx 2\times 10^{-9}$ is fixed by the CMB. Note that in the above expression, the cross term proportional to $\langle\,\zeta_\phi\,\mathcal{S}_\chi\,\rangle = \langle\,\zeta_\phi\,\rangle\langle\,\mathcal{S}_\chi\,\rangle = 0$ as ζ_ϕ and $\mathcal{S}_\chi$ are independent random variables with zero mean. Hence the contribution is only at second order in $f_{\rm PT}$. An

analogous relation holds for PC in LSS.

An important subtlety of the multi-field reheating is that the early Sachs-Wolfe (SW) effect suppresses CMB anisotropies but not the GW anisotropies, $(\delta_{\rm GW}/\delta_\gamma) \approx 5(\mathcal{S}_\chi/\zeta_\phi)$, as can be seen from eqs. (3.12) and (3.14). This is because the SW effect is *anti-correlated* with the dominant adiabatic density fluctuations from ϕ, leading to reduced anisotropy in the observed CMB [94]. On the other hand, the SW contribution, which is predominantly sourced by the energy density in the non-PT sector, $\rho_{\rm nPT}$, is *uncorrelated* with χ fluctuations, and hence there is no analogous cancellation in GW anisotropies.

3.4 Observational aspects of primordial clocks in gravitational waves

The anisotropies for a 2D map (CMB or PT-GWB) are expressed in the multipole basis,

$$\langle \delta(\hat{n})\delta(\hat{n}')\rangle = \sum_\ell \frac{(2\ell+1)}{4\pi} C_\ell P_\ell(\cos\theta)\,, \tag{3.16}$$

where $\hat{n}\cdot\hat{n}' = \cos\theta$ and P_ℓ are the Legendre polynomials. For higher multipoles $\ell \gtrsim O(100)$ (which will be of interest to us later), the expression for C_ℓ can be simplified using flat-sky approximation (see for example [16]):

$$C_\ell \approx \frac{1}{r^2}\int \frac{dk_\parallel}{2\pi}\mathcal{P}_\delta\left(k_\parallel, k_\perp \sim \frac{\ell}{r}\right)\,, \tag{3.17}$$

where $\mathcal{P}_\delta$ is the power spectrum of the density perturbations, $k_{\parallel(\perp)}$ is the component of $\vec{k}$ parallel (perpendicular) to the line-of-sight, and r is the co-moving radius from us to the surface of the map that we see today. The correlation can be separated into a nearly scale-invariant part and a

small PC correction, $C_\ell = C_\ell^{(0)} + \Delta C_\ell$, where $C_\ell^{(0)}[\ell(\ell+1)] \equiv A$ is approximately constant. From eqs. (3.12) and (3.17), $A_{\rm GW} \simeq 32\pi A_\chi$. The PC feature in GWB can be computed using eqs. (3.10) and (3.17),

$$\frac{\Delta C_\ell^{\rm GW}}{C_\ell^{(0)\rm GW}} \approx \theta(\ell - \ell_d)\,\tilde{\alpha}\left(\frac{\ell}{\ell_d}\right)^{-3/2} \cos\left[\frac{M}{H_{\rm inf}}\log\frac{\ell}{\ell_d}\right], \tag{3.18}$$

where the amplitude of the PC feature in the multipole basis, $\tilde{\alpha} = \sqrt{2\pi H_{\rm inf}/M}\,\alpha$, is smaller than α due to the 2-dimensional nature the map. $\ell_d \approx k_d r_{\rm GW}$ corresponds to the multipole where the PC feature appears in the GW map. We can similarly evaluate the amplitude of PCs in CMB using eqs. (3.6), (3.9), and (3.15) instead.

With sufficient experimental sensitivity, the detection of the PC feature is ultimately limited by cosmic variance. If we search in the parameter regime $H_{\rm inf}\ell_d/M \gg 1$, then our signal oscillates slowly as a function of ℓ, in which case we can mitigate cosmic variance by averaging the data over a bin of size $1 < \Delta\ell < \pi H_{\rm inf}\ell_d/M$ around each ℓ. Thus the signal adds coherently while the binned cosmic variance is

$$\frac{\delta C_\ell^{bin}}{C_\ell} \approx \sqrt{\frac{2}{(2\ell+1)\Delta\ell}}\,. \tag{3.19}$$

We determine the observability of the PC feature by comparing its largest amplitude (at ℓ_d) with the smallest compatible binned cosmic variance,

$$\tilde{\alpha} > \sqrt{\frac{2(M/H_{\rm inf})}{\pi(2\ell_d+1)\ell_d}}\,. \tag{3.20}$$

PCs with smaller amplitudes can be observable if they appear at larger ℓ_d, as the cosmic variance

drops. It is however experimentally challenging to probe high ℓ anisotropies. Keeping these issues in mind, we will consider $\ell_d \sim O(10-100)$ in this work.

We also want to estimate the strength of GW signal in our model. During PT, processes like bubble collisions, sounds waves, and turbulence give rise to GW [92]. Conservatively, we will just keep the best understood of these effects, from bubble collisions. (Sound waves and turbulence can give larger contributions at higher β, but are less well-understood.) After production, GW decouple and redshift as radiation until today. An estimate for the peak energy density today as a fraction of critical energy density [95] is

$$\Omega_{\rm GW}h^2 \sim 1.3\times 10^{-6}\left(\frac{H_{\rm PT}}{\beta}\right)^2 f_{\rm PT}^2\,. \tag{3.21}$$

Here β is the rate of bubble nucleation, $H_{\rm PT}$ is the Hubble expansion rate during PT, and we are considering a strong PT where most of the latent heat goes into accelerating the bubble walls. The factor of $f_{\rm PT}$ appears since the PT is occurring in the PT sector that is subdominant in the energy density during PT. The energy density fluctuation in the ℓ^{th} multipole is given by

$$\delta\Omega_{\rm GW}h^2(\ell) \sim \Omega_{\rm GW}h^2 \times \frac{\sqrt{A_{\rm GW}}}{\ell} \tag{3.22}$$

The factor of $1/\ell$ appears because $C_\ell^{(0)} \propto [\ell(\ell+1)]^{-1}$ by scale-invariance. The quantity of interest to us is the deviation from this scale-invariant spectrum due to the PC feature, $\Delta C_\ell^{\rm GW}$. From Eq. (3.18),

$$\delta\Omega_{\rm GW}^{\rm PC}h^2(\ell_d) \sim 1.3\times 10^{-6}\left(\frac{H_{\rm PT}}{\beta}\right)^2 f_{\rm PT}^2\frac{\sqrt{A_{\rm GW}}}{\ell_d}\left(\frac{\tilde{\alpha}}{2}\right). \tag{3.23}$$

3.4.1 Benchmarks

We now present two benchmarks illustrating our mechanism and competing considerations. Consider the following set of parameters for the first benchmark,

$$(1) \quad \sigma_0 \simeq 2H_{\rm inf}, \quad \Lambda_\chi \simeq 40H_{\rm inf}, \quad M = 10H_{\rm inf}, \quad \ell_d = 100 \tag{3.24}$$

$$f_{\rm PT} = 0.1, \ \frac{A_\chi}{A_\phi} = 3, \ \frac{\beta}{H_{\rm PT}} = 5\,. \tag{3.25}$$

From eqs. (3.10) and (3.18), the amplitude of the PC feature in GWB is $\tilde{\alpha} = 0.31$. This easily satisfies the condition of observability over cosmic variance, $\tilde{\alpha} > 0.018$, given in Eq. (3.20). A realization of GWB map containing this PC feature and a random sample of cosmic variance is shown in figure 3.2 (a) without binning and (b) with binning using $\Delta\ell = 6$. We see that the feature is detectable even without any binning, and the observability only improves with binning. Even a modest bin size of $\Delta\ell = 6$ gives a signal-to-noise ratio ~ 7.6. Note that the free-streaming nature of GW implies that such a feature must be a result of super-horizon physics from inflation.

There are also irreducible PC corrections to the maps of adiabatic perturbations as discussed before. Currently, the strongest constraints on these corrections come from the CMB [31], constraining the strength of our PC signal. The PC corrections in CMB also appear around ℓ_d and ℓ_g, as the co-moving radii to the surface of recombination and PT are approximately the same. We take $\Lambda_\phi \gg H$ such that the contribution in Eq. (3.9) is negligible. Eq. (3.6) along with $\dot{\phi}_0 \simeq (60H_{\rm inf})^2$ [7] gives a correction $\left(\Delta C^\gamma_{\ell_g}\right)_{\Delta H_{\rm osc}} / C^{(0)\gamma}_{\ell_g} \simeq 6 \times 10^{-5}$, and Eq. (3.15) gives $\left(\Delta C^\gamma_{\ell_d}\right)_{\rm ind} / C^{(0)\gamma}_{\ell_d} \simeq 0.01$. This is below the cosmic variance as can be checked with Eq. (3.20)

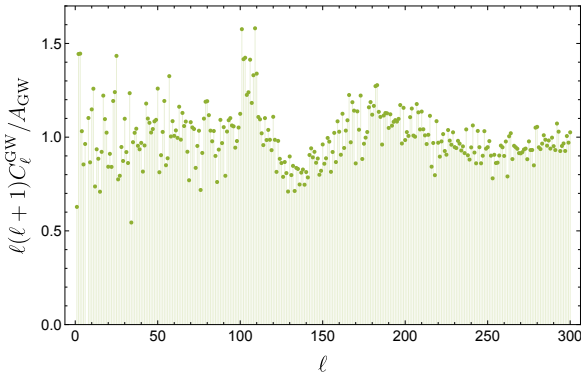

(a) Benchmark (1): Unbinned

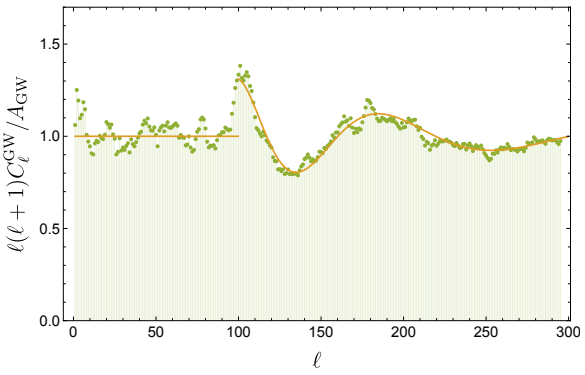

(b) Benchmark (1): Binned, $\Delta\ell = 6$

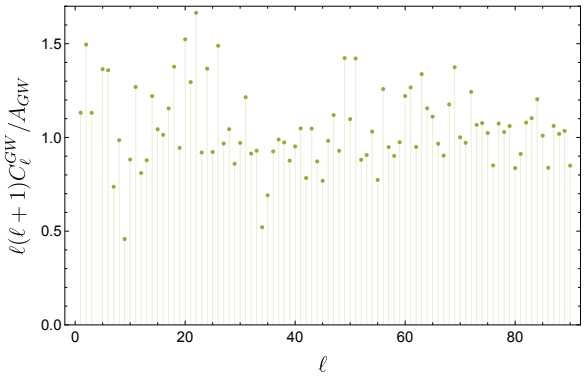

(c) Benchmark (2): Unbinned

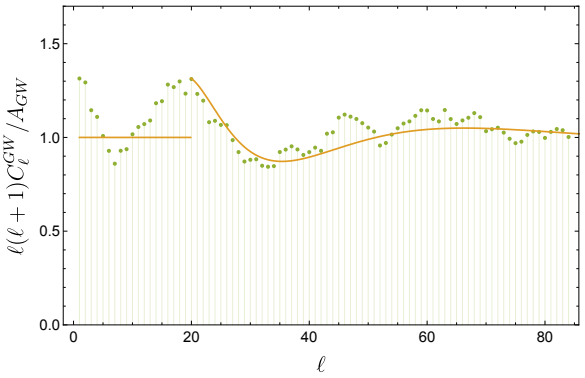

(d) Benchmark (2): Binned, $\Delta\ell = 7$

Figure 3.2: Primordial spectrum $C_\ell^{\rm GW}$ with the PC feature using two sets of benchmark parameters from section 3.4.1. Figures (a) and (b) correspond to benchmark (1) with $\tilde{\alpha} = 0.31$, $M = 10H_{\rm inf}$, $\ell_d = 100$, while figures (c) and (d) correspond to benchmark (2) with $\tilde{\alpha} = 0.31$, $M = 5H_{\rm inf}$, $\ell_d = 20$. The yellow line shows the expected signal and the green dots incorporate a realization of cosmic variance. Figures (a) and (c) show unbinned GW power spectra, while figures (b) and (d) show corresponding binned values with $\Delta\ell = 6$ and $\Delta\ell = 7$, respectively.

(even after accounting for a smaller cosmic variance at $\ell_g \approx 200$). This benchmark is actually conservative in that the current constraints on the PC features from Planck data are even weaker [31], only constraining the amplitudes of PC features to be $\lesssim 0.08$. Access to higher multipoles $\ell \sim \mathcal{O}(1000)$ in the CMB is not really an advantage as the $\ell^{-3/2}$ (or ℓ^{-3}) dependence in the PC features makes them fairly localised near ℓ_d (or ℓ_g). The imparted NG is $f_{\rm NL}^{\rm PC} \sim 5\times10^{-3}$, which is also well below the CMB constraint $f_{\rm NL} < \mathcal{O}(5-50)$ (the exact constraint depends on the shape) [52].

We now estimate the experimental sensitivity required to probe this PC in GWB. The strength of GWB depends on the details of the PT. Here, we consider a relatively strong PT (see [92] for models that could undergo strong PTs). From Eqs. (3.21) and (3.23), we get the isotropic component, $\Omega_{\rm GW}h^2 \simeq 5\times10^{-10}$, and the small PC variation in anisotropies, $\delta\Omega^{\rm PC}_{\rm GW}h^2(\ell_d)\simeq 4\times10^{-15}$. Note that the isocurvature and $N_{\rm eff}$ bounds mentioned earlier are easily satisfied. While the isotropic GWB could be within LISA sensitivity, $\Omega^{\rm LISA}_{\rm GW}h^2 \gtrsim 10^{-14}$ [92], the anisotropies require more advanced future space-based detectors. For reference, the projected sensitivity of the proposed BBO mission for large angular scales is $\Omega^{\rm BBO}_{\rm GW}h^2 \gtrsim 10^{-17}$ [4, 80] and that of ultimate-DECIGO is $\Omega^{\rm DECI}_{\rm GW}h^2 \gtrsim 10^{-19}$ [81]. Detection of the PC will require a detector that maintains such a high sensitivity out to $\ell\sim O(100)$.

In the future, 3D maps such as LSS and 21-cm are expected to achieve higher sensitivity as they can access more modes than a 2D map, and hence have lower cosmic variance. It is then interesting to ask whether there are PCs which can not be detected even in a perfect 3D map of adiabatic perturbations, but detectable with future GW experiments, making isocurvature GWB possibly the only channel of discovery. We demonstrate this possibility in the second benchmark:

$$\begin{aligned}(2)\quad &\sigma_0\simeq 2H_{\rm inf},\quad \Lambda_\chi\simeq 40H_{\rm inf},\quad M=5H_{\rm inf},\quad \ell_d=20,\\ &f_{\rm PT}=0.06,\quad \frac{A_\chi}{A_\phi}=3,\quad \frac{\beta}{H_{\rm PT}}=5\,.\end{aligned}\tag{3.26}$$

From eqs. (3.10) and (3.18), the amplitude of the PC feature in GWB is again $\tilde{\alpha}=0.31$, which satisfies the criterion of observability at $\ell_d=20$, $\tilde{\alpha}>0.06$, given by Eq. (3.20). Figure 3.2 (c) and (d) show a realization of GWB map containing this benchmark and cosmic variance, without binning and with binning, respectively. Due to higher cosmic variance at lower multipoles, the

PC feature is harder to discern in the unbinned map, although small binning, $\Delta\ell = 7$, makes the pattern apparent. While this benchmark requires more rigorous data analysis to separate the PC feature from cosmic variance noise, we will later show that it could be within reach of future space-based GW detectors like ultimate-DECIGO, which are expected to maintain moderate sensitivity out to $\ell \sim \mathcal{O}(10)$.

The PC corrections in the adiabatic perturbations for this case are $\left(\Delta\mathcal{P}_{k_g}\right)_{\Delta H_{\rm osc}}/\mathcal{P}^{(0)}_{k_g} \simeq 2\times10^{-5}$ and $\left(\Delta\mathcal{P}_{k_d}\right)_{\rm ind}/\mathcal{P}^{(0)}_{k_d} \simeq 3\times10^{-3}$, as given by eqs. (3.6) and (3.15), respectively. Cosmic variance for an idealised 3D map is $\left(\delta\mathcal{P}/\mathcal{P}^{(0)}\right) \sim \sqrt{(2k^3_{\rm min})/(4\pi k^2\Delta k)}$, where $k_{\rm min}$ in the largest co-moving mode that can be probes today. Then, using the largest possible bin size, $\Delta k \sim \pi k H_{\rm inf}/M$, the cosmic variance at $k_g \approx 40k_{\rm min}$ is $\left(\delta\mathcal{P}/\mathcal{P}^{(0)}\right) \sim 2\times10^{-3}$, and at $k_d \approx 20k_{\rm min}$ is $\left(\delta\mathcal{P}/\mathcal{P}^{(0)}\right) \sim 6\times10^{-3}$. We see that the PC corrections to the power spectrum of adiabatic perturbations are below cosmic variance even for an idealised 3D map[5]. The imparted NG from Eq. (3.8) is $f^{\rm PC}_{\rm NL} \sim 2\times10^{-4}$, which is certainly below the CMB constraint. A conservative estimate of the cosmic variance in NG for a 3D map gives $\delta f^{\rm PC}_{\rm NL} \sim 1/(\sqrt{N_{k_g}}\zeta_\phi) \sim 10^{-2}$, where N_{k_g} is the number of 3-point configurations satisfying $k_1+k_2+k_3 = 2k_g$ and $\vec{k_1}+\vec{k_2}+\vec{k_3} = 0$, and the anisotropy $\zeta_\phi \sim 10^{-5}$. We see that all PC corrections in this benchmark are undetectably small even for an ideal 3D map.

The GWB in this benchmark has a monopole, $\Omega_{\rm GW}h^2 \simeq 2\times10^{-10}$, and the PC feature, $\delta\Omega^{\rm PC}_{\rm GW}h^2(\ell_d) \simeq 2\times10^{-15}$. The change in the power spectrum of $\delta\Omega_{\rm GW}$ due to the PC feature is then $\Delta C^{\rm GW}_\ell \ell(\ell+1)|_{\ell>\ell_d} \simeq 6.5\times10^{-27}$. Figure (7) of [5] shows the projected noise angular power spectrum of various future GW experiments, based on the code schNell given in [96].

[5]The cosmic variance for any realistic 3D map is larger than the idealised case considered here due to the finite width of the map.

Comparing to these projections, we see that the change in GW power spectrum due to our PC feature ($\sim 6.5 \times 10^{-27}$) is within the sensitivity of the ultimate-DECIGO configuration (for even multipoles).

In summary, these benchmarks show us that there could be PC excitations during inflation whose imprints are undetectable in *any* adiabatic map as the signal could be below the fundamental cosmic-variance uncertainty. On the other hand, the imprints of the same PC in GWB could be much large that the cosmic variance. While the detection GWB (and any features within) is generally challenging, we envision that the improvements in our understanding of foregrounds, detector sensitivity, and angular resolution can bring these exciting features within the reach of future GW experiments.

3.4.2 Broader analysis of the parameter space

Let us now broaden the exploration of the parameter space of PC in GWBs beyond the specific benchmarks above. We fix ℓ_d and analyze observability of the PC feature in $\alpha - M$ space, taking both of these as our independent variables. The requirement of $\alpha < 1$ and $M > H$ ensures $(\sigma_0/\Lambda_\chi) < 1$, satisfying the EFT perturbativity constraint.

Figure 3.3 shows the parameter space (white) of PCs that could be probed by the isocurvature GWB, through the mechanism discussed above. In figure 3.3 (a), we have set $\ell_d = 100$ as in benchmark (1), while in figure 3.3 (b), we set $\ell_d = 20$ corresponding to benchmark (2). Requiring that the (envelope) of the PC feature is larger than the binned cosmic variance excludes the blue regions. Requiring eqs. (3.6) and (3.8) to lie below current CMB sensitivity, $(\Delta\mathcal{P}/\mathcal{P}^{(0)})_\gamma < 0.01$ and $f_{\rm NL} < 10$, along with the restriction $M < \Lambda_\chi$ needed for EFT control, exclude the yellow

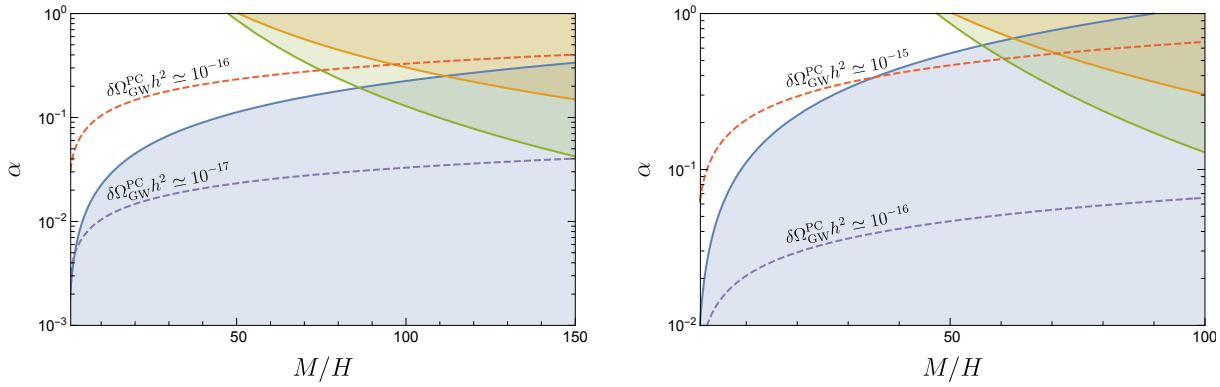

(a) $\ell_d = 100$ (b) $\ell_d = 20$

Figure 3.3: Analysis of the $\alpha - M$ parameter space showing excluded regions from following considerations: binned cosmic variance (blue), CMB constraints from contribution to $\Delta\mathcal{P}_\gamma$ (yellow) and $f_{\rm NL}$ (green). The dashed lines show contours of PC signal strength $\delta\Omega_{\rm GW}^{PC}h^2(\ell_d)$ as given in Eq. (3.23) such that the parameter regions above these lines can be probed with corresponding experimental sensitivities. The analysis is carried out for (a) $\ell_d = 100$, as in the benchmark (1), and (b) $\ell_d = 20$, as in benchamark (2). See the text for more details.

and green regions respectively. The PC feature induced by the PT sector into the adiabatic perturbations, given in Eq. (3.15), can be kept below CMB exclusion with a conservative choice of $f_{\rm PT} = 0.055$ (for $A_\chi/A_\phi = 3$)[6]. The contours of different signal strengths, $\delta\Omega_{\rm GW}^{\rm PC}h^2$, at given ℓ_d are also shown in figure 3.3 with dashed lines. We have fixed $(\beta/H_{\rm PT}) = 5$ here, similar to the benchmark cases. The contours should guide the reader in assessing the experimental sensitivity required to probe PCs that lie above the contour line at a given ℓ_d.

We have assumed that the decay rate $\Gamma(\sigma \to \delta\chi\,\delta\chi) < 3H_{\rm inf}$ such that the dilution of the classical σ field is primarily due to the Hubble expansion, producing $\propto k^{-3/2}$ dependence in the PC signal. For the interaction considered, $\Gamma(\sigma \to \delta\chi\delta\chi) \approx \frac{M^3}{32\pi\Lambda_\chi^2}$ [56]. For the largest mass $M \simeq \Lambda_\chi$, we see that $\Gamma < 3H_{\rm inf}$ for $M \lesssim 300H_{\rm inf}$. Also, the PC oscillation would be unobservable if it is faster than the integer discretization of ℓ. Since the oscillation frequency is fastest near ℓ_d, we require $(M/H_{\rm inf}) < \pi\ell_d$. For $\ell_d = 100$, we again get a similar upper limit

[6] $f_{\rm PT}$ here can in principle be larger for smaller values of α.

$M \lesssim 300 H_{\rm inf}$, and for $\ell_d = 20$, we get $M \lesssim 60 H_{\rm inf}$. The CMB constraints become dominant well before reaching this limit as can be seen in figure 3.3.

Figure 3.3 also illustrates that at least in principle, PC features with smaller amplitudes can be observable if they appear at larger ℓ_d, as the cosmic variance becomes smaller at higher multipoles. This highlights the gains that can be achieved with higher angular resolution and sensitivity in GW experiments.

3.5 Primordial clocks from a polynomial potential

The above analysis considered an unspecified "sharp feature" in the potential [31, 68] to excite the heavy field, leading to the simplest form for the PC features. Here we construct a smoother, more familiar polynomial potential for σ, ϕ, inspired by Hybrid Inflation [97, 98]. In this model, the rolling of the inflaton field triggers a "waterfall" for the σ field. The waterfall however does not end inflation, but leads to a second phase of inflation.

$$V(\phi, \sigma) = V_{\rm inf}(\phi) - \kappa\sigma + \frac{1}{2}(g\phi^2 - \mu^2)\sigma^2 + \frac{\lambda}{4}\sigma^4 \,. \tag{3.27}$$

We will take $V_{\rm inf}(\phi)$ to dominate the energy density and hence drive inflation. σ has a time-dependent mass as ϕ rolls towards 0,

$$M_\sigma^2(t) = g\phi^2(t) - \mu^2 + 3\lambda \langle\, \sigma \,\rangle^2 \,. \tag{3.28}$$

Initially, $g\phi^2 \gg \mu^2$ and $\langle\,\sigma\,\rangle \approx 0$, $V \approx V_{\rm inf}$. As ϕ rolls, σ becomes tachyonic as $g\phi^2 < \mu^2$. The transition occurs at t_0 where $\phi(t_0) = \phi_c$ and

$$g\phi_c^2 = \mu^2\,. \tag{3.29}$$

From here, σ starts rolling rapidly towards the new minimum in about $\Delta t \sim H_{\rm inf}^{-1}$ when the kinetic energy is large enough to overcome Hubble friction. When σ becomes large enough, the last term of Eq. (3.28) ensures σ is non-tachyonic again and oscillates around the adiabatic minimum $M_\sigma(t)/\sqrt{2\lambda}$, which approaches a maximum value $\mu/\sqrt{\lambda}$ at late time. Here we are taking κ to be small such that its role in the σ dynamics after t_0 is subdominant. Earlier, it breaks the degeneracy of the two σ minima when σ becomes tachyonic. This ensures selection of a unique vacuum ($\langle\,\sigma\,\rangle > 0$ for $\kappa > 0$) in the entire observable universe, avoiding the domain wall problem [97][7].

Consider the following model parameters: $\mu = 50H_{\rm inf}$, $g = 1.9\times10^{-8}$, $\phi_c = 3.6\times10^5 H_{\rm inf}$, $\lambda = 0.1$, and $\kappa = 0.1H_{\rm inf}^3$ (with $H_{\rm inf}/M_{\rm pl} = 10^{-5}$ and $\dot\phi_0 \simeq 3.6\times10^3 H_{\rm inf}^2$ [7]). Let us first check that the back-reaction of σ dynamics on ϕ is small. The maximum energy density in σ is subdominant to the inflationary potential energy, $\mu^4/\lambda \sim 10^7 H_{\rm inf}^4 \ll V_{\rm inf} \simeq 3H_{\rm inf}^2 M_{\rm pl}^2 \sim 10^{10}H_{\rm inf}^4$. The kinetic energy of ϕ is given by $3H_{\rm inf}\dot\phi_0 \approx -\partial_\phi V(\phi,\sigma) = -\partial_\phi V_{\rm inf} - g\langle\,\sigma\,\rangle^2\phi$. The correction $g\langle\,\sigma\,\rangle^2\phi \lesssim O(10)H_{\rm inf}^3 \ll \partial_\phi V_{\rm inf} \sim 10^4 H_{\rm inf}^3$. This ensures slow roll of the inflaton even after the tachyonic transition in σ.

In figure 3.4, the full $\langle\,\sigma(t)\,\rangle$ dynamics is shown in blue along with the expected minimum at $M_\sigma(t)/\sqrt{2\lambda}$ shown in yellow. We can see that the dynamics is given by an oscillatory component

[7] In [98], this is done by considering σ to be the radial direction in the quasi-single field model of inflation. Then the centrifugal force due to the turning trajectory acts as the source of explicit symmetry breaking.

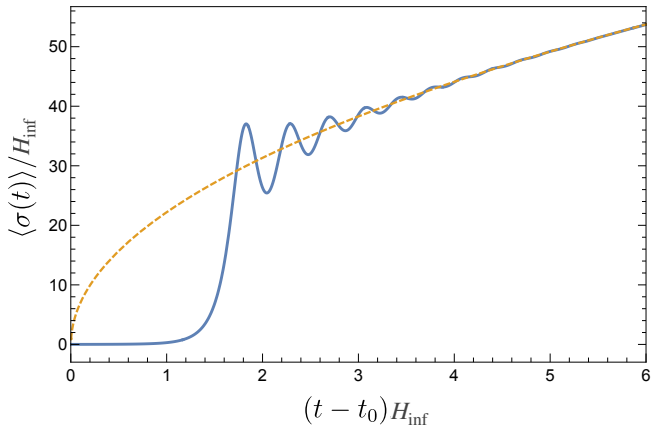

Figure 3.4: The classical dynamics of σ field after the tachyonic transition at t_0 (blue) and the minimum $M_\sigma(t)/\sqrt{2\lambda}$ (yellow). The full dynamics shows oscillations about the minimum.

superimposed on a slowly shifting minimum. We consider the same direct coupling to χ as before, $\mathcal{L}_{\rm int} \sim (\sigma\,\partial_\mu\chi\partial^\mu\chi)/\Lambda_\chi$. The slowly shifting minimum induces a tilt in the otherwise scale-invariant spectrum, while the oscillatory component adds a PC feature. We take $\Lambda_\chi \sim 300H_{\rm inf}$ so as to ensure $(\langle\,\sigma\,\rangle/\Lambda_\chi) < 0.5$.

Figure 3.5 shows the fractional correction to $\mathcal{P}_{\mathcal{S}_\chi}$ evaluated numerically (blue) and a matching signal (yellow) of the type considered in the previous sections arising from a more sharply featured potential with $\alpha \approx 0.125$ and $M \approx 14.8H_{\rm inf}$. The overall shift in $\mathcal{P}_{\mathcal{S}_\chi}$ is the result of $\langle\,\sigma(t)\,\rangle \neq 0$. The largest amplitude of PC feature is around $k_d \sim 100k_{\rm min}$, corresponding to $\ell_d \sim 100$ as expected. The PC is within the observable parameter space, as can be seen from figure 3.3. In this model, the irreducible PC contributions to the CMB from eqs. (3.6) and (3.8) are $(\Delta\mathcal{P}/\mathcal{P}^{(0)})_\gamma \simeq 0.001$ and $f_{\rm NL} \simeq 0.1$ respectively, which are below CMB sensitivity. Comparing to the yellow signal due to sudden excitation of the σ field, we see that our waterfall model gives a PC that dilutes slightly slower and oscillates with higher frequency as M_σ increases with time.

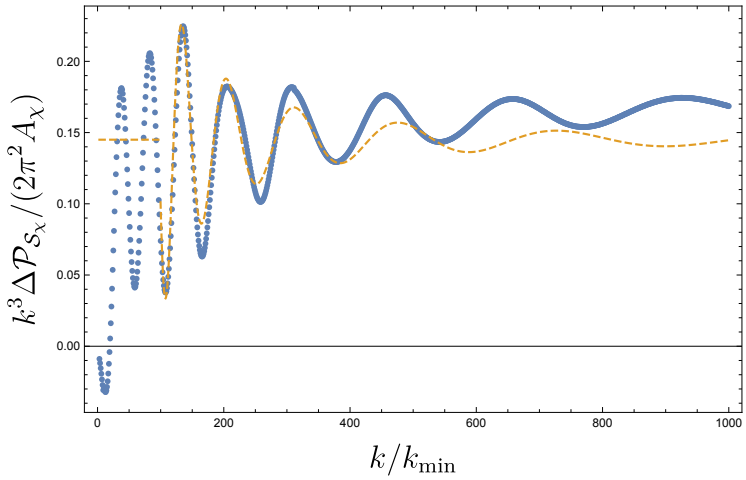

Figure 3.5: The PC feature in $\mathcal{P}_{\mathcal{S}_\chi}$ in the model with polynomial potential. The blue dots correspond to the numerical evaluation of $\Delta\mathcal{P}_{\mathcal{S}_\chi}$, where the overall shift is the result of $\langle\,\sigma\,\rangle \neq 0$. For reference, the yellow dashed line shows a matching signal from a simplified scenario where σ is instead excited suddenly, resulting in a PC with constant amplitude $\alpha \approx 0.125$ and mass $M \approx 14.8 H_{\rm inf}$.

3.6 Conclusion

We have shown that the power spectrum of GWB superhorizon anisotropies could reveal striking oscillations (see figure (3.2)), which could only arise from extremely heavy fields during inflation. However, any such new physics introduces irreducible (gravitational) corrections to the spectrum of adiabatic perturbations. Remarkably, it is possible for the GWB oscillations to be clearly visible while the CMB and LSS remain insensitive to the irreducible corrections, despite their high precision and statistics. While we have considered specific PC features, the mechanism can be extended to other localised features and to non-Gaussian correlators. We have illustrated a model in which the oscillations in anisotropy appeared at $\ell \sim \mathcal{O}(10-100)$ in order to maintain better theoretical control and minimize cosmic variance. At $\ell \sim \mathcal{O}(100)$, any features are more discernible against cosmic variance, but experimentally challenging in terms of angular resolution and signal strength. On the other hand, at $\ell \sim \mathcal{O}(10)$, the experimental

measurements are less challenging, but any features are harder to separate from cosmic variance and would require a more rigorous data analysis. We have also constructed a model of PC field with a smoother potential, which is polynomial in the fields. We find this potential to be more plausible within effective field theory considerations. In this case of the polynomial potential, the primordial clock "beats" irregularly, but its non-trivial frequency $M(k)$ seen in figure 3.5 sheds light on the smooth potential and mechanism exciting σ.

Chapter 4: Large Primordial Fluctuations in Gravitational Waves from Phase Transitions

4.1 Introduction

In the previous chapter, we explored the potential of gravitational wave backgrounds from first order phase transitions as novel maps of density perturbations. We saw that the fluctuations of the GWB could be predominantly isocurvature in nature, that is they could be uncorrelated with the adiabatic perturbations seen within CMB. Such an isocurvature in GWB would imply the existence of another light quantum field during inflation. Isocurvature GWB are therefore portals into the dynamics of new fields and their interactions which are beyond our reach of adiabatic maps. However, to be readily distinguished and interpreted the isocurvature should be larger than the CMB anisotropy. This is because any GWB would receive an irreducible contribution from the adiabatic perturbations through the gravitational Sachs-Wolfe effect $\sim 10^{-5}$. Therefore, large fractional anisotropies $> 10^{-5}$ in the GWB would be ideal for revealing new inflationary physics.

For example, take the ALP field χ that was considered in Chapter 3 as the origin of isocurvature perturbations. The fractional perturbations in the energy density of the ALP field compared to its average are then given by the ratio of the inflationary Hubble scale to the initial field misalignment, $\delta_\chi \sim (H_{\rm inf}/\chi_0)$. In high-scale inflation where the Hubble constant is taken to

be $\sim 10^{-5}$ times the Planck scale [7], the ALP fluctuations are likely to be $\gg 10^{-5}$ if the ALP misalignment is constrained to being sub-Planckian. Also, if the Hubble constant during inflation can be inferred independently, through the detection of primordial tensor modes for example [6], then the measurement of GWB isocurvature would give us the initial misalignment of the ALP field. Therefore, large isocurvature GWB sourced by this ALP field will be an ideal target for gravitational wave experiments.

Unfortunately, there is a significant challenge for large GWB anisotropies to even be detectable. A distinct isocurvature GWB requires that there be two mostly decoupled sectors at the time of the phase transition: one sector with adiabatic perturbation reheated by the inflaton, and another undergoing the phase transition reheated by a separate light field, in our case an ALP. The phase-transitioning sector in such a case must be significantly subdominant at recombination to avoid its impact on the CMB, which is highly constrained from observations. In the case of standard radiation dominance in the early universe, this subdominance implies a strong suppression in the overall strength of the GWB signal [1], making detection of large anisotropies extremely difficult at upcoming or proposed detectors.

In this work, we will show that the trade-off between large fractional anisotropy and detectability of GW signals can be evaded if there is a period of early matter dominance (eMD)[1] in the cosmological history. In this scenario, the phase-transitioning sector can be dominant at the time of the phase transition, avoiding suppression in GW signal at its production time. A later stage of eMD in the adiabatic sector will dilute the phase-transitioning sector such that its contribution to CMB anisotropies is subdominant. It would necessarily also dilute the overall GWB, but we will show that this dilution is less severe. Importantly, the anisotropic component is left

[1]Early in this context means before Big Bang Nucleosynthesis.

unsuppressed in absolute size, which brings a larger range of anisotropies within the sensitivity of upcoming detectors.

The rest of the chapter is organized as follows. In section 4.2, we recap the original model of isocurvature GWB from a phase transition from [1], also reviewed in section 3.3.1 of Chapter 3. We re-examine why, with radiation dominance, consistency with CMB constraints predicts that large fractional anisotropies in the GWB must come at the expense of suppressed signal strength, both in the isotropic and anisotropic components. In section 4.3, we introduce our new eMD model and show how a large fractional anisotropy in the GWB is consistent with CMB constraints, along the lines sketched above. We also show that the eMD dilution of the GWB results in only a modest redshift of the GW frequency spectrum relative to the original model. In section 4.4, we consider the gravitational interactions between the phase transition and adiabatic sectors prior to their merging to see that they do no affect our conclusions in section 4.3 on large scales, but also to consider new constraints on small scales from primordial black hole production, small-scale structure formation, and scalar-induced gravitational wave production at second order. In section 4.5, we present plausible benchmarks in our model with different fractional GWB anisotropies and the associated isotropic and anisotropic signal strengths. We compare with the analogous benchmarks in the original radiation-dominated model to illustrate the significant gains in signal strength, in both the isotropic and anisotropic components. We conclude in section 4.6 with a short discussion of the significance of our results.

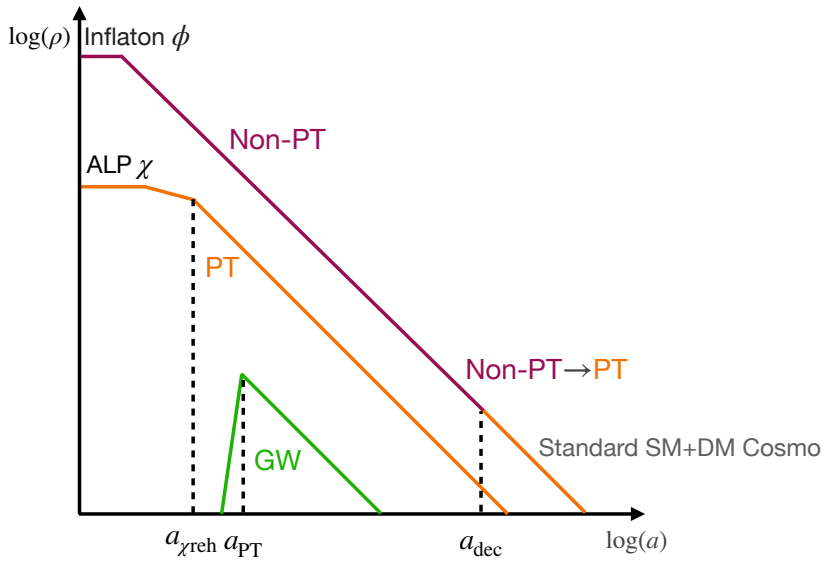

Figure 3.1 showing the simple model of isocurvature GWB from Ref. [1] has been repeated here for the ease of understanding.

4.2 Recap: isocurvature GWB in the radiation-dominated model

Let us recap the model of isocuravtrue GWB proposed in Ref. [1], in which the phase transition and adiabatic sectors of the very early universe are always radiation-dominated, prior to merging into a single sector via (late) particle decays. This model is reviewed in greater detail in section 3.3.1 of Chapter 3. We have also repeated figure 3.1 above for the ease of comparison with the modification that we will propose shortly in section 4.3. The ALP field χ that is subdominant during inflation reheats some extension of the SM at $t_{\chi\mathrm{reh}}$ when $m_\chi \sim H$ after the end of inflation. This extension of SM then undergoes a first-order phase transition (PT), and is therefore referred to as the "PT sector". The inflaton on the other hand is taken to reheat another sector that is weakly interacting with the PT sector, and therefore, does not participate in the phase transition. This sector is referred to as the "non-PT" sector. The non-PT sector decays to the SM + DM at t_{dec} after the phase transition, but before the decoupling of DM. After t_{dec}, a

single SM+DM plasma remains such that there is no additional isocurvature introduced from the non-PT sector.

Following Eq. (3.12), the anisotropies of the GWB can be written as

$$\delta_{\rm GW} = 4\zeta_\chi \left(1 - \frac{4}{3} f_{\rm PT}\right) - \frac{16}{3}\zeta_\phi \,, \tag{4.1}$$

where

$$f_{\rm PT} \equiv \frac{\rho_{\rm PT}}{\rho_{\rm total}}, \tag{4.2}$$

and the gauge-invariant fluctuations are

$$\zeta_\phi(k) = \frac{H_{\rm inf}\delta\phi(k)}{\dot{\phi}_0}, \quad \zeta_\chi(k) = \frac{2\delta\chi(k)}{3\chi_0} \,. \tag{4.3}$$

The field fluctuations $\delta\phi \sim \delta\chi \sim H_{\rm inf}$.

In Eq. (4.1), $\zeta_\phi \sim 10^{-5}$ sets the minimum $\delta_{\rm GW}$. This comes from the Sachs-Wolfe (SW) effect, which is dominated by the fluctuations of the non-PT sector. A small $\zeta_\chi < 10^{-5}$ would be swamped by the SW contribution, leaving the GWB to be predominantly adiabatic. On the other hand, large isocurvature in GWB coming from $\zeta_\chi > 10^{-5}$, would clearly imply the existence of a new light quantum field during inflation. Hence, we will focus on the range $\zeta_\chi > 10^{-5}$.

Following Eq. (3.14), the fluctuations in the SM plasma (and hence in the CMB and matter

distribution) after $t_{\rm dec}$ are given by

$$\delta_\gamma \approx -\frac{4}{5}\zeta_\phi - \frac{4}{5} f_{\rm PT}\zeta_\chi. \tag{4.4}$$

As expected, the contribution of ζ_χ to CMB can be kept small by choosing sufficiently small $f_{\rm PT}$. From the CMB observations [99], $\delta_\gamma \simeq 3.6 \times 10^{-5}$, giving a constraint

$$f_{\rm PT}\,\zeta_\chi \leq 4.5 \times 10^{-5}\,. \tag{4.5}$$

Therefore, since we are interested in $\zeta_\chi \gg 10^{-5}$, the PT sector must be sufficiently subdominant, $f_{\rm PT} \ll 1$. This leads to the simplification of Eq. (4.1),

$$\delta_{\rm GW} \approx 4\zeta_\chi. \tag{4.6}$$

Additionally, if ζ_χ contains qualitative features which are not observed in CMB, such as those discussed in Chapter 3, the constraint on $f_{\rm PT}\,\zeta_\chi$ will be even stronger, requiring yet smaller $f_{\rm PT}$.

4.2.1 Strength of GWB and its anisotropies

During a first-order phase transition, gravitational waves are dominantly produced through bubble dynamics. It has been noted that the GW production is suppressed when the PT sector constitutes a smaller fraction of the total energy density at the time of the phase transition, i.e. $f_{\rm PT} < 1$ [100, 101]. This can also be seen through Eq. (3.21). In terms of the fraction of energy density in gravitational waves compared to the critical energy density at the time of production

($t_{\rm PT}$), the suppression goes as

$$\Omega_{\rm GW}(t_{\rm PT}) \equiv \frac{\rho_{\rm GW}(t_{\rm PT})}{\rho_{\rm total}(t_{\rm PT})} \approx f_{\rm PT}^2 \overline{\Omega}_{\rm GW}(t_{\rm PT}), \tag{4.7}$$

where $\overline{\Omega}_{\rm GW}$ represents GWB for a single sector system with $f_{\rm PT} = 1$. Intuitively, the amplitude of the gravitational wave must be $\mathcal{O}(f_{\rm PT})$, so that it vanishes in the absence of the PT plasma. Since GW energy density goes as the square of this amplitude, we expect $f_{\rm PT}^2$ scaling of the right hand side of Eq. (4.7). We elaborate on this scaling in Appendix B.1.

To estimate the strength of the GWB, we specialize to the plausible and relatively tractable scenario in which the gravitational waves are produced dominantly from bubble wall collisions in the envelope approximation[2]. Using Eq. (4.7) and taking the expression for $\overline{\Omega}_{\rm GW}$ from [92], the GWB spectrum today can be given as[3]

$$\Omega_{\rm GW}^{(0)} h^2 \approx 1.67 \times 10^{-5} \tilde{\beta}^{-2} f_{\rm PT}^2 \left(\frac{\kappa \alpha_{\rm PT}}{1+\alpha_{\rm PT}}\right)^2 \left(\frac{100}{g_*(t_{\rm PT})}\right)^{1/3} \left(\frac{0.11 v_w^3}{0.42 + v_w^2}\right) S_{\rm bub}(\omega), \tag{4.8}$$

where the frequency dependence is

$$S_{\rm bub}(\omega) = \frac{3.8(\omega/\omega_{\rm peak})^{2.8}}{1 + 2.8(\omega/\omega_{\rm peak})^{3.8}}\,. \tag{4.9}$$

[2]In the case of significant coupling between the PT plasma and bubble walls, the majority of latent heat can be transferred to the plasma making sound waves the dominant source of gravitational waves. However, it turns out that for the parameters that we choose as the benchmark, i.e. $\alpha_{\rm PT} \sim 1$ and $\tilde{\beta} \sim 10$, the sound wave contribution will be similar in strength to the estimate in Eq. (4.10) even if all the latent heat is transferred to the kinetic energy of the plasma [102].

[3]Ref. [103] has pointed out that the peak energy density of the gravitational wave background from a phase transition can be enhanced if the small scale inhomogeneities ($H(t_{\rm PT}) < k < \beta$) in the PT plasma are large, i.e. $(\delta T/T) \gtrsim \tilde{\beta}^{-1}$. Since we consider relatively low $\tilde{\beta} = 10$ in all of our benchmarks, this effect is subdominant even for the biggest $\zeta_\chi \sim 10^{-2}$ on small scales that we will consider later. It will be important while considering more generic values of $\tilde{\beta} \sim \mathcal{O}(100)$. Also, note that this effect modifies the frequency spectrum, but does not affect the angular power spectrum which is the main focus of our work.

Here, $\alpha_{\rm PT}$ is the ratio of the latent heat released compared to the energy density of the PT plasma before the phase transition, and κ is the efficiency of the latent heat transfer to bubble walls. We will take $\alpha_{\rm PT} \approx 1$, such that the efficiency $\kappa \approx 1$, and the bubble wall velocity $v_w \approx 1$. The peak frequency today $\omega_{\rm peak}$ can be estimated by redshifting the typical frequency at the time of phase transition ω_*, given by $\omega_* \approx 0.23\, H(t_{\rm PT})\, \tilde{\beta}$. We choose $\tilde{\beta} = 10$ for all our benchmarks. g_* corresponds to the effective number of relativistic degrees of freedom, and we take $g_*(t_{\rm PT}) \sim 100$ [4]. Note that the envelope approximation is relatively crude and specific phase transitions may exhibit significant deviations[5]. However, it suffices for our purpose here since our main focus will be the angular power spectrum.

With the choice of parameters described above, the expression in Eq. (4.8) at the peak frequency is simplified to

$$\Omega^{(0)}_{\rm GW} h^2 \approx 3.2 \times 10^{-9} f^2_{\rm PT}\,. \tag{4.10}$$

Following Eq. (4.6), the size of the fluctuations in the GWB, which is relevant for detection, is

$$\delta\Omega^{(0)}_{\rm GW} h^2 \approx \Omega^{(0)}_{\rm GW} h^2 \times 4\zeta_\chi \approx 1.3 \times 10^{-8} f^2_{\rm PT} \zeta_\chi\,. \tag{4.11}$$

The constraint of Eq. (4.5) gives us an upper bound on the inhomogeneities of the GWB,

$$\delta\Omega^{(0)}_{\rm GW} h^2 \leq 5.8 \times 10^{-13} f_{\rm PT}\,. \tag{4.12}$$

Note that despite relative anisotropy $\delta\rho_{\rm GW}/\rho_{\rm GW} \sim \zeta_\chi$ being large $> 10^{-5}$, the absolute signal

[4] In reality, $g_*(t_{\rm PT}) > 100$ depending on the exact extension of the SM undergoing the phase transition. However, this is a small effect considering the $g_*^{-1/3}$ dependence in Eq. (4.8).

[5] See for example [104] for an updated numerical study of the phase transition in an abelian gauge theory with a comparison to the envelope approximation.

strength of the fluctuations is suppressed by one power of $f_{\rm PT}$, making it more difficult to detect.

4.3 Isocurvature GWB with an era of early matter dominance (eMD)

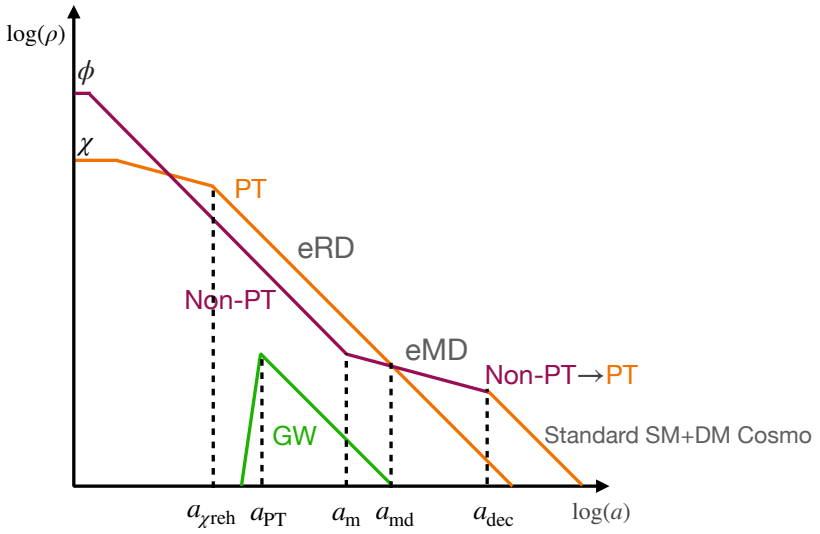

Figure 4.1: A schematic of the modified eMD model discussed in section 4.3 showing energy densities in various sectors as a function of the scale factor (time). While the decay products of the ALP χ are always radiation dominated, one of the massive particles (reheaton) in the decay products of the inflaton leads to a period of early matter domination.

Smaller $f_{\rm PT}$ at $t_{\rm dec}$ allows for larger ζ_χ while evading constraints from CMB summarized in Eq. (4.5). If both PT and non-PT sectors are radiation-dominated throughout, then this also constrains the PT sector to be subdominant by the same factor $f_{\rm PT}$ at the time of the phase transition, heavily suppressing the strength of GW produced, as seen in eqs. (4.10) and (4.12). This, however, will not be the case if there is a deviation from standard radiation dominance, for example, a period of early matter domination (eMD). In such modified cosmological histories, $f_{\rm PT}$ is effectively a function of time, and can be such that the PT sector is dominant during the phase transition and only becomes subdominant by $t_{\rm dec}$. We will show that this significantly enhances the strength of GWB compared to the purely-radiation-dominance scenario of [1], while still be-

ing consistent with constraints from CMB. For clarity, we define this time-dependent fraction as $\hat{f}(t)$, and its late time value at $t_{\rm dec}$ will continue to be denoted by $f_{\rm PT}$.

Here we describe such a modified cosmological history with eMD, shown schematically in figure 4.1. As in the minimal model, the inflaton reheats the non-PT sector at the end of inflation, which dilutes like radiation, $\rho_{\rm nPT} \propto a^{-4}$. On the other hand, ρ_χ acts like matter while oscillating around its minimum, which dilutes slower than radiation. If the oscillations persist for a sufficiently long time, ρ_χ can dominate the energy density (as well as the curvature perturbations) of the universe before decaying to the PT sector, which subsequently undergoes the phase transition. Notice that unlike the radiation-dominated model described previously, the PT sector dominates the energy density during the phase transition, and therefore $\rho_{\rm GW}$ is not suppressed at production by $f_{\rm PT}$. We will call this period of $\rho_{\rm PT}$ domination the era of early radiation dominance (eRD).

Now we take the non-PT sector to be dominated by massive particles which become non-relativistic around $t_{\rm m}$, sometime after the phase transition, redshifting slower than the radiation in the PT sector. The eRD of the PT sector is thereby replaced by eMD in the non-PT sector at $t_{\rm md}$. The period of eMD ends at $t_{\rm dec}$ when the non-PT massive particles decay, reheating the SM+DM. We will therefore refer to these massive non-PT particles as "reheatons". The reheaton decays are taken to occur before DM decoupling, which allows thermalization with the SM and the remnants of the phase transition in the PT sector, matching onto the standard cosmological history from then on. In this way, we arrive at the following time-dependence of $\hat{f}_{\rm PT}$ from the

$1/a^3$ redshifting of non-relativistic matter and the $1/a^4$ redshifting of relativistic radiation:

$$\hat{f}_{\rm PT}(t) = \begin{cases} (1+\epsilon)^{-1} & t_{\chi\rm reh} \leq t \leq t_m \\ \left(1+\epsilon\frac{a}{a_m}\right)^{-1} = \left(1+\frac{a}{a_{\rm md}}\right)^{-1} & t_m < t \leq t_{\rm dec}\,, \end{cases} \tag{4.13}$$

where $\epsilon \equiv \left(\frac{\rho_{\rm nPT}}{\rho_{\rm PT}}\right)\Big|_{t_{\chi\rm reh}}$ and we have used $\epsilon(a_{\rm md}/a_m) = 1$. Therefore, $f_{\rm PT} \equiv \hat{f}_{\rm PT}(t_{\rm dec}) = (1 + a_{\rm dec}/a_{\rm md})^{-1} \approx (a_{\rm md}/a_{\rm dec})$.

4.3.1 Strength of GW and anisotropies

In this model with eMD, the PT sector dominates the energy density at the phase transition, $\rho_{\rm total}(t_{\rm PT}) \approx \rho_{\rm PT}(t_{\rm PT})$ and $\hat{f}_{\rm PT}(t_{\rm PT}) \approx 1$. Hence, in Eq. (4.8) for GW production at the time of the transition, $f_{\rm PT}^2$ is not a suppression.

However, the period of eMD dilutes GW radiation because of the differential redshifting of matter and GW radiation, such that

$$\frac{\rho_{\rm GW}(t_{\rm dec})}{\rho_{\rm total}(t_{\rm dec})} = \hat{f}_{\rm PT}(t_{\rm dec})\frac{\rho_{\rm GW}(t_{\rm PT})}{\rho_{\rm total}(t_{\rm PT})}\,. \tag{4.14}$$

This, along with the same microphysical parameters as in section 4.2.1 for the phase transition, gives the fractional energy density in GWB today as

$$\Omega_{\rm GW}^{(0)}h^2 \approx 3.2\times10^{-9} f_{\rm PT}\,. \tag{4.15}$$

Note that the GW signal in this model, despite the dilution from eMD, has only one power of $f_{\rm PT}$

suppression, compared to the quadratic suppression in Eq. (4.7).

The anisotropy of the GWB can again be related to the fluctuations of χ,

$$\delta_{\rm GW} \approx -\frac{4}{3}\zeta_\chi \,. \tag{4.16}$$

The factor in front of ζ_χ is smaller compared to Eq. (4.6) because the SW contribution, in this case, comes from the PT sector itself, and is therefore anti-correlated with the inherent inhomogeneities of the GWB. The expression for the anisotropies of the CMB for all relevant scales (i.e., the scales that re-enter much after $t_{\rm dec}$) remains the same as Eq. (4.4),

$$\delta_\gamma \approx -\frac{4}{5}\zeta_\phi - \frac{4}{5} f_{\rm PT}\zeta_\chi \,. \tag{4.17}$$

This is shown explicitly in section 4.4.1. The inhomogeneity in the GWB is then

$$\delta\Omega^{(0)}_{\rm GW}h^2 \approx \Omega^{(0)}_{\rm GW}h^2 \times \frac{4}{3}\zeta_\chi \approx 4.3\times 10^{-9} f_{\rm PT}\zeta_\chi \,. \tag{4.18}$$

We must still satisfy the constraint in Eq. (4.5). Saturating it gives

$$\delta\Omega^{(0)}_{\rm GW}h^2 \leq 1.9\times 10^{-13} \,, \tag{4.19}$$

which is now independent of $f_{\rm PT}$, as opposed to Eq. (4.12). The possibility that the relative anisotropies in the GWB are large while the absolute size of the anisotropic signal is unsuppressed by $f_{\rm PT}$, is the main result of this chapter.

4.3.2 Peak frequency of GWB

The frequency spectrum of the GWB will be slightly shifted compared to the single-sector scenario ($f_{\rm PT} = 1$) due to the modified cosmological history. At production, the typical frequency of GWB for the choice of parameters given in section 4.2.1 is [92]

$$\omega_* \approx 0.23\tilde{\beta} H(t_{\rm PT}). \tag{4.20}$$

Red-shifting this frequency gives the peak frequency of the spectrum today

$$\begin{aligned}\omega_{\rm peak} &= \omega_* \left(\frac{a_{\rm PT}}{a_0}\right) \\ &\approx 0.23\tilde{\beta} \left(\frac{a_{\rm PT}}{a_0}\right) \left(\frac{H(t_{\rm PT})}{H(t_{\rm md})}\right) \left(\frac{H(t_{\rm md})}{H(t_{\rm dec})}\right) \left(\frac{H(t_{\rm dec})}{H(t_{eq})}\right) \left(\frac{H(t_{eq})}{H(t_0)}\right) H(t_0).\end{aligned} \tag{4.21}$$

Using $H \propto a^{-3/2}$ during matter dominance, while $H \propto a^{-2}$ during radiation dominance,

$$\begin{aligned}\omega_{\rm peak} &\approx 0.23\tilde{\beta} \left(\frac{a_{\rm PT}}{a_0}\right) \left(\frac{a_{\rm md}}{a_{\rm PT}}\right)^2 \left(\frac{a_{\rm dec}}{a_{\rm md}}\right)^{3/2} \left(\frac{a_{eq}}{a_{\rm dec}}\right)^2 \left(\frac{a_0}{a_{eq}}\right)^{3/2} H(t_0) \\ &\approx 2.8 \times 10^{-17} \tilde{\beta} \left(\frac{a_{eq}}{a_{\rm PT}}\right) f_{\rm PT}^{1/2} \text{ Hz},\end{aligned} \tag{4.22}$$

where we have used the fact that the redshift at matter-radiation equality in the standard cosmological history $z_{eq} \approx a_{eq}^{-1} \approx 3100$, $H(t_0) \approx 2.2 \times 10^{-18}$ Hz, and $a_{\rm md}/a_{\rm dec} \approx f_{\rm PT}$ from Eq. (4.13). Now,

$$\frac{a_{eq}}{a_{\rm PT}} = \frac{T_{\rm PT}(t_{\rm PT})}{T_{\rm SM}(t_{eq}))} f_{\rm PT}^{-1/4} \left(\frac{g_*(t_{\rm md})}{g_*(t_{\rm dec})}\right)^{1/4}. \tag{4.23}$$

Then with $T_{\rm SM}(t_{eq}) \sim 1$ eV, $g_*(t_{\rm md}) \sim g_*(t_{\rm dec}) \sim 100$, and setting $\tilde{\beta} = 10$, we get

$$\omega_{\rm peak} \approx 2.8 \times 10^{-4} f_{\rm PT}^{1/4} \left(\frac{T_{\rm PT}(t_{\rm PT})}{\rm TeV} \right) \text{ Hz}. \tag{4.24}$$

The dependence on $f_{\rm PT}$ is very mild, less than an order of magnitude in the range of $f_{\rm PT}$ that we will be led to consider. For a single sector ($f_{\rm PT} = 1$), a phase transition occurring at $T_{\rm PT}(t_{\rm PT}) \sim 100$ TeV gives $\omega_{\rm peak} \sim 28$ mHZ, falling within the sensitivity of LISA [37], BBO [40], and DECIGO [41]. As we lower the fraction of the PT sector to the smallest $f_{\rm PT} \sim 4.5 \times 10^{-4}$ of interest to us (see the last benchmark in Table 4.1), the peak frequency shifts to $\omega_{\rm peak} \sim 4$ mHZ, remaining within the sensitivity of the above-mentioned detectors. In this case, an eMD starting shortly after the phase transition when $T_{\rm PT}(t_{\rm md}) \sim 32$ TeV ensures $T_{\rm SM}(t_{\rm dec}) \sim 100$ GeV and $f_{\rm PT} \sim 4.5 \times 10^{-4}$.

4.4 Gravitational crosstalk

The PT and non-PT sectors can influence each other gravitationally even though they are otherwise only weakly coupled. We want to ensure that the CMB scales are unaffected despite large perturbations in the PT sector during eRD era. We also want to identify other constraints on our eMD model which may arise from the evolution of perturbations after horizon re-entry. We address these two concerns here.

4.4.1 Modes that are superhorizon prior to $t_{\rm dec}$

Our modified early cosmology reverts to standard cosmology at $t_{\rm dec}$, where we will take $T_{\rm SM}(t_{\rm dec}) \gtrsim 100$ GeV. We want to ensure that the observed fluctuation modes of the CMB and

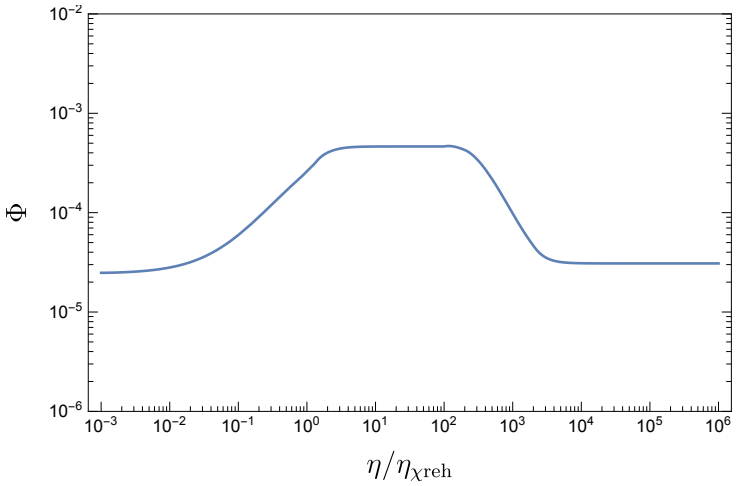

Figure 4.2: $\Phi(k)$ as a function of the conformal time η for a co-moving mode k that re-enters sufficiently after the end of eMD. We have taken a benchmark, $\zeta_\chi \approx 10^{-3}$, $\zeta_\phi \approx 3.5\times10^{-5}$, $f_{\rm PT} \approx 10^{-2}$, and $\epsilon = 1/2$. Conformal times denoting boundaries of different eras are $(\eta_{\rm m}/\eta_{\chi\rm reh}) \sim (\eta_{\rm md}/\eta_{\chi\rm reh}) \sim 100$ and $(\eta_{\rm dec}/\eta_{\chi\rm reh}) \sim 2000$.

LSS would be unaffected by the modified cosmology before $t_{\rm dec}$, and this is relatively straightforward to analyze because they are all superhorizon prior to $t_{\rm dec}$, given the high $T_{\rm SM}(t_{\rm dec})$.

We use the convention where the perturbed FLRW metric is given by [105],

$$g_{00} = -1 - 2\Psi, \quad g_{ij} = a^2(t)\delta_{ij}[1 + 2\Phi], \quad g_{0i} = 0\,. \tag{4.25}$$

In the absence of anisotropic stress, $\Phi = -\Psi$, and the relevant Einstein equation is

$$\eta\Phi' + \Phi + \frac{k^2\eta^2}{3}\Phi = \frac{1}{2}\sum_i f_i\delta_i\,, \tag{4.26}$$

where $'$ denotes partial derivative with respect to the conformal time η and k is the co-moving momentum. $f_i \equiv \rho_i/\rho_{\rm total}$ is the fraction of the energy density in the $i^{\rm th}$ sector and $\delta_i \equiv \delta\rho_i/\rho_i$ is the fractional density perturbation. When a certain mode is superhorizon, the k^2-term in Eq. (4.26)

can be neglected, giving

$$\eta\Phi' + \Phi = \frac{1}{2}\sum_i f_i\delta_i\,. \tag{4.27}$$

The gauge invariant fluctuation of a non-interacting fluid is conserved on superhorizon scales. For fluid i, it is given by

$$\zeta_i = \Phi + \frac{\delta_i}{3(1+w_i)}\,, \tag{4.28}$$

where w_i is its equation of state. Then $\zeta_{\rm nPT} = \zeta_\phi$ and $\zeta_{\rm PT} = \zeta_\chi$ remain constant until horizon re-entry. This also dictates the superhorizon evolution of radiation and matter density perturbations,

$$\delta'_{\rm rad} = -4\Phi', \quad \delta'_{\rm mat} = -3\Phi'\,. \tag{4.29}$$

Using eqs. (4.27) and (4.29), we numerically evaluated the evolution of Φ for $\zeta_\chi \approx 10^{-3}$, $\zeta_\phi \approx 3.5\times10^{-5}$, $f_{\rm PT} \approx 10^{-2}$, and $\epsilon = 1/2$, as shown in figure 4.2. While Φ is larger during eRD when the total curvature perturbation is dominated by ζ_χ, it becomes small again after eMD[6]. Let us do a few consistency checks. Eqs. 4.27 and 4.28 can be simplified to give $\Phi \approx \frac{2}{3}\zeta_{\rm total}$ during radiation dominance. Then we expect $\Phi \approx \frac{2}{3}\left(\frac{2}{3}\zeta_\chi + \frac{1}{3}\zeta_\phi\right) \approx 4.6\times10^{-4}$ (using $\epsilon = 1/2$) during eRD, while $\Phi \approx \frac{2}{3}\left(f_{\rm PT}\zeta_\chi + \zeta_\phi\right) \approx 3\times10^{-5}$ during radiation dominance after eMD. This is exactly what we find in figure 4.2. Therefore, the anisotropy in CMB (and in other late-time maps of adiabatic perturbations) remains small at 10^{-5} even in our modified scenario with PT

[6] A similar conclusion was found in [106]. They consider a model with two curvatons where one of the curvatons with larger perturbations dominates the energy density during an earlier era of radiation domination.

sector domination during eRD.

4.4.2 Modes that have re-entered the horizon prior to $t_{\rm dec}$

In this section, we focus on the evolution of density perturbations in the non-PT sector and Φ for the modes that re-enter the horizon during eRD and eMD. This will be relevant for the constraints on ζ_χ on small scales, which can indirectly affect CMB or LSS.

The gradient terms that we neglected for superhorizon evolution become important as the mode becomes subhorizon. The coupled evolution of perturbations is given by

$$\begin{aligned}
\eta\Phi' + \Phi + \frac{k^2\eta^2}{3}\Phi &= \frac{1}{2}\sum_i f_i\delta_i \\
\delta''_{\rm rad} + \frac{k^3}{3}\delta_{\rm rad} &= -4\Phi'' + \frac{4k^2}{3}\Phi \\
\delta''_{\rm mat} + \frac{1}{\eta}\delta'_{\rm mat} &= -3\Phi'' + k^2\Phi - \frac{3}{\eta}\Phi' \,.
\end{aligned} \tag{4.30}$$

Let us start by analyzing the evolution of a co-moving mode that re-enters the horizon during eRD, generically labeled $k_{\rm eRD}$. Just before its re-entry, $\Phi(k_{\rm eRD}\eta \lesssim 1) \approx (2/3)\zeta_\chi$ as the PT sector is dominant. Since $\zeta_\phi = \Phi + \delta_{\rm nPT}/4 \sim 10^{-5}$ is conserved on superhorizon scales, we get $\delta_{\rm nPT}(k_{\rm eRD}\eta \lesssim 1) \approx -4(\Phi - \zeta_{\rm nPT}) \approx -(8/3)\zeta_\chi$ for $\zeta_\chi \gg \zeta_\phi$.

After the horizon re-entry at $\eta_{\rm eRD} \sim 1/k_{\rm eRD}$, perturbations follow eqs. 4.30. Below, we describe their qualitative behavior. Fluctuations in the radiation of the PT sector, $\delta_{\rm PT}$, oscillate in time with a constant amplitude throughout eRD and eMD. The behaviour of Φ and $\delta_{\rm nPT}$, however, changes significantly. During eRD, $|\Phi| \propto \eta^{-2}$ drops rapidly, while the amplitude of $\delta_{\rm nPT}$ remains constant when the non-PT sector is radiation-dominated and increases logarithmically $\sim \log(a)$ when it becomes matter-dominated. This logarithmic growth is insignificant if ϵ is close to 1,

which we take to be the case. The linear growth during eMD, however, is significant when $\delta_{\rm nPT} \propto a$, and consequently Φ becomes constant. In summary,

$$|\delta_{\rm nPT}(k_{\rm eRD})| \approx \begin{cases} \frac{8}{3}\zeta_\chi & \eta_{\rm eRD} \leq \eta < \eta_{\rm md} \\ 2\frac{\eta^2}{\eta_{\rm md}^2}\zeta_\chi & \eta_{\rm md} \leq \eta < \eta_{\rm dec} \\ \frac{8}{3}\frac{\eta_{\rm dec}^2}{\eta_{\rm md}^2}\zeta_\chi & \eta_{\rm dec} \leq \eta\,, \end{cases} \tag{4.31}$$

where we have used the adiabatic relation $\delta_{\rm rad}/4 = \delta_{\rm mat}/3$ at the transitions between radiation and matter dominance, and $a \propto \eta^2$ during MD. Similarly, the behaviour of Φ can be given as

$$|\Phi(k_{\rm eRD})| \approx \begin{cases} \frac{2}{3}\frac{\eta_{\rm eRD}^2}{\eta^2}\zeta_\chi & \eta_{\rm eRD} \leq \eta < \eta_{\rm md} \\ \frac{3}{5}\frac{\eta_{\rm eRD}^2}{\eta_{\rm md}^2}\zeta_\chi & \eta_{\rm md} \leq \eta < \eta_{\rm dec} \\ \frac{2}{3}\frac{\eta_{\rm eRD}^2\eta_{\rm dec}^2}{\eta_{\rm md}^2\eta^2}\zeta_\chi & \eta_{\rm dec} \leq \eta\,, \end{cases} \tag{4.32}$$

where we have used the fact that Φ decreases by a factor of $(9/10)$ during a transition from RD to MD, and increases by $(10/9)$ during a transition from MD to RD.

Now let us similarly analyze the evolution of perturbations for a co-moving mode $k_{\rm eMD}$ that re-enters during eMD. As $\hat{f}_{\rm PT}$ drops during eMD, the total density perturbation decreases, leading to a decreasing $\Phi(k_{\rm eMD})$ even on superhorizon scales. This can also be seen in figure 4.2. Using superhorizon conservation of $\zeta_{\rm nPT} = \zeta_\phi$, we see that the density perturbation $\delta_{\rm nPT} \sim -\Phi$ also decreases. After horizon re-entry, however, $\delta_{\rm nPT} \propto a$ increases while Φ remains constant till

the end of the eMD era. Then

$$|\delta_{\rm nPT}(k_{\rm eMD})| \approx \begin{cases} 2\dfrac{(\eta_{\rm md}\eta)^2}{\eta_{\rm eMD}^4}\zeta_\chi & \eta_{\rm eMD} \le \eta < \eta_{\rm dec} \\ \dfrac{8}{3}\dfrac{(\eta_{\rm md}\eta_{\rm dec})^2}{\eta_{\rm eMD}^4}\zeta_\chi & \eta_{\rm dec} \le \eta\,, \end{cases} \tag{4.33}$$

and the evolution of Φ is

$$|\Phi(k_{\rm eMD})| \approx \begin{cases} \dfrac{4\hat{f}_{\rm PT}}{5+\hat{f}_{\rm PT}}\zeta_\chi + \dfrac{3(1-\hat{f}_{\rm PT})}{5+\hat{f}_{\rm PT}}\zeta_\phi \approx \dfrac{4\eta_{\rm md}^2}{5\eta_{\rm eMD}^2}\zeta_\chi + \dfrac{3}{5}\zeta_\phi & \eta_{\rm eMD} \le \eta < \eta_{\rm dec} \\ \dfrac{\eta_{\rm dec}^2}{\eta^2}\left[\dfrac{4f_{\rm PT}}{5}\zeta_\chi + \dfrac{4}{5}\zeta_\phi\right] \approx \dfrac{\eta_{\rm dec}^2}{\eta^2}\left(\dfrac{4}{5}\dfrac{\eta_{\rm md}^2}{\eta_{\rm eMD}^2}\zeta_\chi + \dfrac{4}{5}\zeta_\phi\right) & \eta_{\rm dec} \le \eta\,. \end{cases} \tag{4.34}$$

Here, we have used $f_{\rm PT} \ll 1$. The results of this section will be useful while analyzing constraints on our eMD model, which we discuss next.

4.4.2.1 Structure on small scales

The density perturbations in the non-PT sector grow during eMD as seen in eqs. (4.31) and (4.33). These overdensities will be retained and transferred to the SM+DM plasma after the reheaton decay. This poses the danger of overabundance of small-scale structures like compact mini-halos in the late universe. In reality, however, various processes at play during the decay of reheaton and DM decoupling suppress these small-scale fluctuations, effectively erasing any accumulated growth from the eMD era. We list the relevant processes below:

1. Refs. [107,108] showed that the perturbative decay of the reheaton into radiation suppresses the amplitude of radiation perturbations by as much as $\sim 10^{-3}$ for subhorizon modes $k \gtrsim 20k_{\rm dec}$.

2. Frictional damping and acoustic oscillations during kinetic decoupling and free-streaming of DM afterwards erase DM fluctuations on all length scales smaller than the maximum of the horizon size at decoupling and the free-streaming length-scale [109, 110]. These effects erase enhancement in DM perturbations for all modes $k \gtrsim k_{\rm dec}$ that re-entered during eRD and eMD.

3. Finally, large perturbations in the baryon and photon plasma are erased by Silk damping [61, 62], and thus do not contribute to additional small-scale structure.

These mechanisms that erase DM perturbations on small scales require DM to be in thermal equilibrium with the SM at the time of reheaton decay. Our choice of $T_{\rm SM}(t_{\rm dec}) \gtrsim 100$ GeV ensures that a standard WIMP-like DM candidate would satisfy this criterion. In summary, enhanced structure formation on small scales can be easily avoided in our eMD model by taking appropriately high reheat temperature for the SM at $t_{\rm dec}$.

4.4.2.2 Primordial Black Holes

Horizon patches with sufficient overdensity can collapse to form primordial black holes (PBH) in the early universe, which cannot be erased by the mechanisms discussed above. PBH production from adiabatic perturbations $\sim 10^{-5}$ is negligible. However, in our modified model, larger density perturbations during eRD and eMD era will enhance PBH production, giving a constraint on the power spectrum of χ on small scales.

During radiation dominance, the Hubble patches exceeding a certain critical overdensity (δ_c) collapse to form PBH. At a given time, the fraction of such collapsing patches can then be

given as [111]

$$\beta_{\rm rad} = \int_{\delta_c}^{\infty} P(\delta) d\delta \approx \frac{\sigma}{\delta_c} \exp\left(-\frac{\delta_c^2}{2\sigma^2(M_H)}\right) . \tag{4.35}$$

Here M_H is the horizon mass and $\sigma^2(M_H)$ is the variance of the mass overdensities of Hubble patches, which is related to the power spectrum of the curvature perturbations $\mathcal{P}_\mathcal{R}$[7],

$$\sigma^2(M_H) \equiv \langle (\delta M/M_H)^2 \rangle = \frac{16}{81} \int_0^\infty (q/k)^2 j_1^2(q/(\sqrt{3}k)) \tilde{W}^2(q/k) \mathcal{P}_\mathcal{R} \frac{dq}{q} . \tag{4.36}$$

Here, j_1 is the spherical Bessel function, and $\tilde{W}(q/k)$ is the Fourier transform of a window function used to smooth density contrast over the length scale $k^{-1} \sim (aH)^{-1}$. During eRD, $\mathcal{P}_\mathcal{R} \approx \mathcal{P}_\chi$. A real-space top hat window function in Eq. (4.36) gives $\sigma^2(M_H) \sim 1.1\mathcal{P}_\chi$ [112]. The value of δ_c can vary between $0.4 - 0.7$ depending on the density distribution within the collapsing patch [113], but we take $\delta_c \approx 0.4$ for a conservative estimate. PBH formation during the radiation era is thought to follow the phenomenon of critical collapse, which produces a distribution of PBH up to arbitrary low masses [111, 114–116],

$$M_{\rm PBH} = M_H(\delta - \delta_c)^\gamma . \tag{4.37}$$

The most stringent constraint in the low mass region comes from CMB distortions caused by the evaporation of light PBH. This puts a constraint on their formation probability $\beta_{\rm eRD} \lesssim 10^{-25}$

[7] The power spectrum for any gauge-invariant perturbation 'i' is defined as

$$\langle\, \zeta_i(\vec{k}) \zeta_i(\vec{k}')\, \rangle \equiv \delta(\vec{k} + \vec{k}') \frac{(2\pi)^3}{k^3} \mathcal{P}_i(k) ,$$

For a scale-invariant spectrum, $\mathcal{P}(k)$ is constant.

[2, 3]. From eqs. (4.35) and (4.36), this translates to a bound $\zeta_\chi \lesssim 0.04$ on small scales (high k). A more significant enhancement of PBH formation occurs during the eMD era. This gives a stronger bound on small-scale ζ_χ, which we discuss below.

Density perturbations in the non-PT sector would grow linearly during MD, $\delta_{\rm nPT} \propto a(t)$, as discussed in section 4.4.2. Thus, even small perturbations can lead to significant PBH formation. When the perturbation becomes non-linear $\delta_{\rm nPT} \gtrsim \mathcal{O}(1)$, the corresponding Hubble patch separates from the background expansion and eventually collapses. A conservative bound on small-scale ζ_χ can then be obtained by simply requiring that the perturbations never become nonlinear during eMD, i.e.,

$$\delta_{\rm PT}\left(\frac{a_{\rm dec}}{a_{\rm md}}\right) \approx 4\zeta_\chi f_{\rm PT}^{-1} < 1. \tag{4.38}$$

Taking $\zeta_\chi f_{\rm PT} \lesssim 4 \times 10^{-5}$ from Eq. (4.5), we get an upper bound on *small-scale* $\zeta_\chi < 3 \times 10^{-3}$. Note that this upper bound becomes tighter if the eMD lasts longer. However, this simple bound is too restrictive and a more careful analysis gives a fairly $f_{\rm PT}$-independent bound $\zeta_\chi < 10^{-2}$ on small scales. We elaborate on this below.

It was shown in [117, 118] that despite over-densities becoming nonlinear, only patches with sufficient spherical symmetry and homogeneity can collapse to form PBH[8]. The probability of PBH formation on the co-moving scale k^{-1} is then

$$\beta_{\rm mat}(k) \approx 0.2\left(\frac{r_{\rm sch}}{r_k}\right)^{13/2}, \tag{4.39}$$

[8]The patches that do not satisfy these criteria form pancake/cigar-shaped structures instead. These are later dispersed due to the radiation pressure when the non-PT sector decays to SM.

where $r_k \sim a/k$ is the physical wavelength of the mode and $r_{\rm sch}$ is the Schwarzschild radius corresponding to the typical overdense region on length scale r_k. The ratio $(r_{\rm sch}/r_k) \approx \delta_{\rm nPT}(k,t)(aH/k)^2$ remains constant during eMD due to the linear growth of $\delta_{\rm nPT}$. Hence, the ratio can be evaluated at horizon re-entry for the modes re-entering during eMD, while for the modes that have re-entered before eMD, the ratio is evaluated at the start of eMD. From eqs. (4.31) and (4.33), we get

$$\frac{r_{\rm sch}}{r_k} \approx \begin{cases} \delta_{\rm nPT}(k, a_{\rm md}) \left(\dfrac{a_k}{a_{\rm md}}\right)^2 \approx 2\zeta_\chi \left(\dfrac{a_k}{a_{\rm md}}\right)^2 & k \geq k_{\rm md} \\ \delta_{\rm nPT}(k, a_k) \approx 2\zeta_\chi \left(\dfrac{a_{\rm md}}{a_k}\right) & k_{\rm md} > k > k_{\rm dec}, \end{cases} \tag{4.40}$$

where a_k corresponds to the scale factor (time) at the horizon re-entry of the co-moving mode k, and we have used $H \propto a^{-2}$ during RD while $H \propto a^{-3/2}$ during MD. Clearly, the largest β corresponds to the mode re-entering at the start of eMD, $k_{\rm md}$, with $\beta_{\rm mat}(k_{\rm md}) \approx 18\zeta_\chi^{13/2}$.

The mass of PBH formed from a certain comoving mode k during the matter domination era is roughly the horizon mass at reentry. Unlike radiation, pressureless matter does not seem to follow critical collapse [119–121]. For the modes that re-enter during eRD but form PBH during eMD, the PBH mass is instead the mass within a patch of radius $\sim a_{\rm md}\, k^{-1}$ at the start of eMD. Thus

$$M_{\rm PBH}|_{\rm eMD} \approx \begin{cases} M_H(a_k) \left(\frac{a_k}{a_{\rm md}}\right) & k \geq k_{\rm md} \\ M_H(a_k) & k_{\rm md} > k > k_{\rm dec}. \end{cases} \tag{4.41}$$

Modes re-entering after eMD have curvature perturbation $\sim 10^{-5}$ as shown in section 4.4.1,

and produce negligible amount of PBH following Eq. (4.35). However, the modes that re-entered earlier during eRD and eMD retain larger perturbations even in the standard radiation-dominated era (sRD) after eMD, until they are erased by mechanisms discussed in section 4.4.2.1. We will show that despite large perturbations, there is no additional enhancement in PBH formation from these modes in the sRD. The collapse probability of a subhorizon mode in sRD can be estimated by performing Jeans mass analysis [122]. Balancing kinetic and gravitational potential energy gives the Jeans mass $M_J = 2r/G$ for a spherical region of radius r. (Here, G is the gravitational constant.) The condition for instability $M > M_J$ then gives the critical overdensity for subhorizon modes,

$$\delta_c = \frac{1}{2G\rho r^2} = \frac{1}{2\pi^2 G\rho}\frac{k^2}{a^2}\,, \tag{4.42}$$

where we have taken $r = \pi a/k$. Using $8\pi G\rho = 3H^2$, the critical overdensity at some time t during sRD is

$$\delta_c = \frac{4}{3\pi}\left(\frac{k^2}{(aH)^2}\right) = \frac{4}{3\pi}\left(\frac{(a_k H_k)^2}{(aH)^2}\right) = 0.43\left(\frac{a_{\rm dec}}{a_k}\right)\left(\frac{a}{a_{\rm dec}}\right)^2\,, \tag{4.43}$$

Note that the critical overdensity is bigger for subhorizon modes than the constant ≈ 0.4 we had taken before. Now, $\delta_{\rm nPT}(k,t) = \delta_{\rm nPT}(k,t_k)(a_{\rm dec}/a_k)$ due to the linear growth during eMD. Thus the ratio

$$\frac{\delta_c(t)}{\delta_{\rm nPT}(k,t)} \approx \frac{0.43}{\delta_{\rm nPT}(k,t_k)}\left(\frac{a}{a_{\rm dec}}\right)^2 \geq \frac{0.43}{\delta_{\rm nPT}(k_{\rm md},t_{\rm md})} \tag{4.44}$$

is smallest at $t \approx t_{\rm dec}$ and for the co-moving mode $k_{\rm md}$. Using eqs. (4.35) and (4.36), the

probability of collapse of the subhorizon modes during sRD is then

$$\beta_{\rm sRD} \lesssim \exp\left(-\frac{0.43^2}{2(1.1\mathcal{P}_\chi)}\right) . \tag{4.45}$$

Following the analysis at the beginning of this section, we see that this production probability is much smaller than that from the eMD era.

Having analyzed PBH production, let us connect it to the experimental bounds on the fraction of PBH today,

$$f_{\rm PBH} \equiv \frac{\Omega^{(0)}_{\rm PBH}}{\Omega^{(0)}_{\rm DM}} = \int dM \psi(M). \tag{4.46}$$

Here $\Omega^{(0)}_{\rm DM} \approx 0.26$ and the mass function $\psi(M)$ is defined as

$$\psi(M) = \frac{1}{\Omega^{(0)}_{\rm DM}} \frac{dn}{d\ln M} = \frac{1}{\Omega^{(0)}_{\rm DM}\, M}\, \beta(M) \left(\frac{a_{\rm eq}}{a_{\rm dec}}\right). \tag{4.47}$$

The factor of $(a_{\rm eq}/a_{\rm dec})$ in the above equation accounts for the relative enhancement of PBH abundance during the radiation dominated era since PBH dilute slower like pressure-less matter. The mass of PBH can be evaluated using Eq. (4.41) along with the relation $\rho_{\rm total} \approx 3H^2 M_{\rm Pl}^2$, giving

$$M_{\rm PBH}(k) \sim \begin{cases} 10^{-6} M_\odot \left(\dfrac{a_k}{a_{\rm md}}\right)^3 f_{\rm PT}^{3/2} \left(\dfrac{100{\rm GeV}}{T_{\rm SM}(t_{\rm dec})}\right)^2 & k \geq k_{\rm md} \\ 10^{-6} M_\odot \left(\dfrac{a_k}{a_{\rm dec}}\right)^{3/2} \left(\dfrac{100{\rm GeV}}{T_{\rm SM}(t_{\rm dec})}\right)^2 & k_{\rm md} > k > k_{\rm dec}\,. \end{cases} \tag{4.48}$$

Here, $M_\odot$ corresponds to the solar mass and we have used $M_{\rm Pl} \sim 10^{-39} M_\odot$.

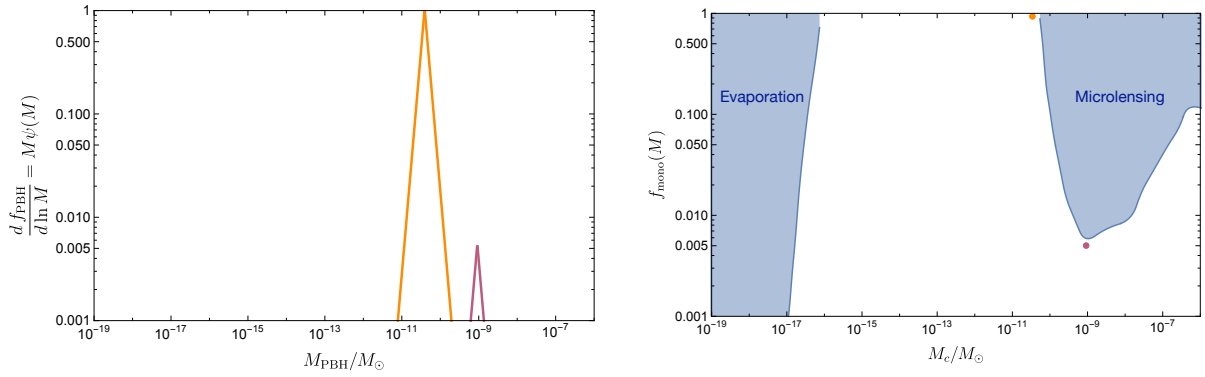

a) b)

Figure 4.3: (a) Fraction of DM energy density in PBH per logarithmic interval as a function of PBH mass in units of solar mass $M_\odot$. (b) Relevant constraints on monochromatic PBH mass functions from CMB distortions and microlensing (taken from [2, 3]). In (a), we show PBH mass distributions for two benchmarks in our eMD model: $\zeta_\chi \approx 5 \times 10^{-3}$, $f_{\rm PT} \approx 9 \times 10^{-3}$, $T_{\rm SM}(t_{\rm dec}) = 100$ GeV in purple, and $\zeta_\chi \approx 10^{-2}$, $f_{\rm PT} \approx 4.5 \times 10^{-3}$, $T_{\rm SM}(t_{\rm dec}) = 300$ GeV in orange. Noting the roughly monochromatic shape of these distributions, we have also shown their monochromatic best fits in (b) for an intuitive comparison with the constraints.

Constraints on PBH are typically given for a monochromatic mass function, [2, 3]

$$\psi_{\rm mono} = f_{\rm PBH}\, \delta(M - M_c). \tag{4.49}$$

Figure (4.3) (b) shows these constraints as blue regions. The same constraints can also be used to check the viability of an extended mass function following the method of [123], which translates to the following condition

$$\int dM \frac{\psi(M)}{f_{\rm mono}(M)} \leq 1. \tag{4.50}$$

Here, $f_{\rm mono}$ is the maximum allowed fraction for a monochromatic mass function.

To evaluate the largest allowed ζ_χ on small scales, we have chosen two benchmarks saturating the limit in Eq. (4.5) and assuming a scale-invariant spectrum:

1. $\zeta_\chi \approx 5 \times 10^{-3}$, $f_{\rm PT} \approx 9 \times 10^{-3}$, and $T_{\rm SM}(t_{\rm dec}) = 100$ GeV (purple).

2. $\zeta_\chi \approx 10^{-2}$, $f_{\rm PT} \approx 4.5 \times 10^{-3}$, and $T_{\rm SM}(t_{\rm dec}) = 300$ GeV (orange).

The mass function for these benchmarks is shown in figure 4.3 (a). For a quick and more intuitive comparison with the constraints, we can take advantage of the roughly monochromatic appearance of our mass functions. In figure 4.3 (b), we therefore indicate where their monochromatic best fits would lie. The figure makes it clear that the most relevant constraints are from microlensing. However, since our benchmarks lie close to the microlensing constraints, we have also used the more refined criterion of Eq. (4.50) to check that they are not excluded. It is then clear that PBH production constraints $\zeta_\chi \lesssim 10^{-2}$ on small scales.

Interestingly, our eMD model produces a sharply peaked PBH mass function without any sharp peaks in either $\mathcal{P}_{\zeta_\chi}$ or $\mathcal{P}_{\zeta_\phi}$. The peak corresponds to PBH produced from $k_{\rm md}$ (i.e. the comoving mode that re-enters right at the start of eMD). Such a spectrum is typically achieved by introducing a scale-invariance-breaking feature in the inflationary potential that can significantly enhance power at a specific k. In our model, the same can be achieved simply by the interplay of energy densities of two sectors, where both have scale-invariant fluctuations albeit of different amplitudes. Also note that for the second benchmark, PBH can make up the entirety of DM. A larger PBH fraction can be obtained at lower $T_{\rm SM}(t_{\rm dec})$ by taking smaller $f_{\rm PT}$ (and not saturating Eq. (4.5)). Generally, $\zeta_\chi \lesssim 10^{-2}$ is required to avoid overproduction of PBH. The exact bound depends on the values of $T_{\rm SM}(t_{\rm dec})$ and $f_{\rm PT}$ as they can shift the location of the peak, exposing it to stricter constraints. However, eqs. (4.39) and (4.40) suggest that even moderately smaller ζ_χ will be sufficient to evade these constraints.

In conclusion, we require $\zeta_\chi \lesssim 10^{-2}$ on *small scales* to avoid overproduction of PBH. If

the power spectrum of χ is nearly scale-invariant, as we have considered in this work for simplicity, this also constrains ζ_χ and $\delta_{\rm GW}$ on the *large scales* relevant for GW detectors. However, $\zeta_\chi \gtrsim 10^{-2}$ on large scales can be made consistent with PBH constraints if the power spectrum is significantly red-tilted. This would require special model-building for the χ potential, which we do not consider in this work.

4.4.2.3 Scalar-induced gravitational waves

A weaker gravitational wave background can be induced by curvature perturbations at second order in perturbation theory (see [124] for a recent review). Larger curvature perturbations and the presence of eMD can enhance its production[9]. Here, we estimate the strength of such induced-GWB and compare it to the gravitational waves from the phase transition.

The fraction of energy density in the induced-GWB per logarithmic k is

$$\Omega_{\rm GW}^{\rm ind}(\eta, k) = \frac{1}{24}\left(\frac{k}{a(\eta)H(\eta)}\right)^2 \overline{\mathcal{P}_h(\eta, k)} \tag{4.51}$$

where $\overline{\mathcal{P}_h(\eta, k)}$ is the time-averaged tensor power spectrum. It is related to the power spectrum of curvature perturbations as

$$\mathcal{P}_h(\eta, k) = 4\int_0^\infty dv \int_{|1-v|}^{|1+v|} du \left[\frac{4v^2 - (1+v^2-u^2)^2}{4vu}\right]^2 [I(v,u,x)]^2 \mathcal{P}_\mathcal{R}(kv)\mathcal{P}_\mathcal{R}(ku) \tag{4.52}$$

where $u = |\vec{k} - \vec{k'}|/k$, $v = k'/k$, and $x \equiv k\eta$. $I(v,u,x)$ contains information about the dynamics of scalar and tensor perturbations and is given in Ref. [126]. The curvature perturbations can be

[9] Enhancement of primordial GWB in the presence of eMD generated by $f(R)$ gravity has been studied in [125].

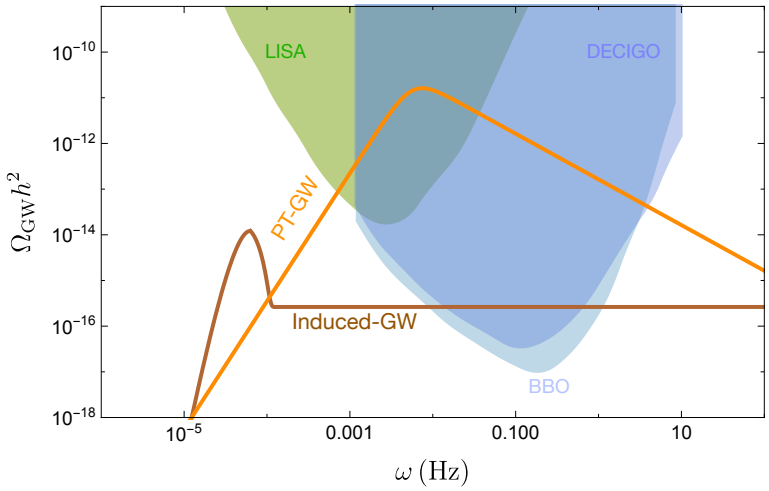

Figure 4.4: Strength of the GWB from phase transition (orange) occurring at $T_{\rm PT}(t_{\rm PT}) \sim 100$ TeV and that induced from curvature perturbations at second order (brown), compared with the power-law integrated sensitivities of LISA, BBO, and DECIGO (taken from [4]). The GWBs are computed for the benchmark that saturates PBH constraint (see discussion in section 4.4.2.2) with $\zeta_\chi = 10^{-2}$, $f_{\rm PT} = 4.5 \times 10^{-3}$, and $T_{\rm SM}(t_{\rm dec}) = 300$ GeV.

related to (first-order) Φ as

$$\mathcal{P}_\mathcal{R} = \left(\frac{5+3w}{3+3w}\right)^2 \mathcal{P}_\Phi \tag{4.53}$$

Thus, the magnitude of $\mathcal{P}_h \propto \mathcal{P}_\Phi^2$.

During radiation dominance, $\Phi(\eta, k) \propto 1/\eta^2$ decays quickly inside the horizon. Thus, induced gravitational waves are dominantly produced at horizon re-entry for modes that re-enter deep in the eRD era. This is not the case for modes re-entering during eMD, since Φ remains constant even after horizon re-entry during eMD. The result is a relative enhancement of induced-GWB during eMD compared to the case of pure radiation dominance.

Refs. [126–128] have analysed production of induced-GWB in matter dominance era for a scale-invariant $\mathcal{P}_\Phi$ that remains constant on super-horizon scales[10]. We borrow results of [126]

[10]It was pointed out in [129] and [130] that the strength of the induced GW from eMD sensitively depends on the exact model for the decay of the matter at the end of eMD. It was observed that a slow decay process suppresses

with appropriate rescaling as explained below. While $\Phi(k) \sim \zeta_\chi$ remains constant for a super-horizon mode during eRD, it decreases during eMD till horizon re-entry as the PT sector becomes subdominant (see figure 4.2). After horizon re-entry, $\Phi(k)$ becomes constant again till the end of eMD, and this value depends on the time of re-entry for each mode. The dominant effect of this evolution of Φ on the strength of induced-GWB is the k-dependent rescaling of the results in [126] by a factor $\lambda(k)$. This rescaling factor $\lambda(k)$ can be obtained by noting that $\mathcal{P}_h \propto \mathcal{P}_\Phi^2$, and using Eq. (4.34),

$$\lambda(k) \approx \left[\frac{3}{2}\left(\frac{4\hat{f}_{\rm PT}(t_k)}{5+\hat{f}_{\rm PT}(t_k)}\right)\right]^4 \tag{4.54}$$

Then the strength of the induced-GWB is given as

$$\frac{\Omega_{\rm GW}^{\rm sec(0)}(k)}{\mathcal{P}_\chi^2 \Omega_{\rm rad}^{(0)}} \approx \begin{cases} 0.8 f_{\rm PT} & k > 2k_{\rm md} \\ 0.8 f_{\rm PT} + \left(\frac{\lambda(k)}{14000}\left(\frac{k}{k_{\rm dec}}\right)^2 (1-2\tilde{k}^{-1})^4 \right. & \\ \qquad \left. \times \left[105\tilde{k}^2 + 72\tilde{k} + 16 - 32\tilde{k}^{-1} - 16\tilde{k}^{-2}\right]\right) & 2k_{\rm md} \geq k > k_{\rm md} \\ \frac{\lambda(k)}{14000}\left(\frac{k}{k_{\rm dec}}\right)^2 \left[1792\tilde{k}^{-1} - 2520 + 768\tilde{k} - 105\tilde{k}^2\right] & k_{\rm md} \geq k > k_{\rm dec} \end{cases} \tag{4.55}$$

where $\tilde{k} \equiv k/k_{\rm md}$. The frequency of the GW today can be related to the co-moving mode k as

$$\omega = \frac{k}{2\pi} \sim 1.5 \times 10^{-15}\left(\frac{k}{1{\rm Mpc}^{-1}}\right) {\rm Hz} \tag{4.56}$$

the induced GW signal compared to Eq. (4.55), while a quick decay enhances the signal. We suspect that a typical perturbative decay of the reheaton will fall under 'slow decay', suppressing induced GW signal. However, we have taken a conservative estimate following [126].

Figure 4.4 shows $\Omega_{\rm GW}$ from phase transition (orange) and that induced from curvature perturbations (brown) as a function of frequency. We have taken the largest $\zeta_\chi \approx 10^{-2}$ allowed on small scales from PBH consideration (see benchmark 2 from section 4.4.2.2). We see that the GWB signal from phase transition is much larger than induced-GWB. Decreasing ζ_χ will quickly make induced-GWB signal undetectably small given its sensitive dependence on the curvature perturbations seen in Eq. (4.55). Interestingly, while a small $f_{\rm PT}$ suppresses GWB signal from the phase transition, it enhances induced-GWB. We will explore this aspect of induced-GWB in future work.

4.5 Benchmarks and Observability

The energy density in any GWB is bounded by two considerations. Firstly, it contributes to $N_{\rm eff}$ as a species of dark radiation, but the $N_{\rm eff}$ constraint is relatively mild:

$$\rho_{\rm GW} < 0.1\rho_\gamma. \tag{4.57}$$

Since we are interested in the possibility of $\delta_{\rm GW} \gg 10^{-5}$, it necessitates an isocurvature origin for the GWB. The stronger bounds on isocurvature from CMB give

$$\delta\rho_{\rm GW} < 0.1\delta\rho_\gamma. \tag{4.58}$$

This can be translated to

$$\delta\Omega^{(0)}_{\rm GW}h^2 < 10^{-5}\Omega^{(0)}_\gamma h^2 \sim 2.5\times 10^{-10}, \tag{4.59}$$

where $\Omega_\gamma^{(0)} h^2 \approx 2.5 \times 10^{-5}$. We choose benchmarks that satisfy this constraint and also show that our modified eMD scenario brings $\delta\Omega_{\rm GW}^{(0)}$ of the signal closer to this upper bound over a large range of anisotropies.

In table 4.1, we consider benchmarks that saturate Eq. (4.5), i.e. $\zeta_\chi f_{\rm PT} = 4.5 \times 10^{-5}$. Corresponding GWB signals and their inhomogeneities are computed for the radiation-dominated model of [1] using eqs. (4.10) and (4.12). The same quantities are also computed for our eMD scenario using eqs. (4.15) and (4.19). We see that both the isotropic GWB signal and the absolute inhomogeneities are comparable or larger in the eMD model for $\zeta_\chi \gtrsim 10^{-4}$.

	Benchmarks		**Radiation-dominance**		**eMD**	
	ζ_χ	$f_{\rm PT}$	$\Omega_{\rm GW}^{(0)} h^2$	$\delta\Omega_{\rm GW}^{(0)} h^2$	$\Omega_{\rm GW}^{(0)} h^2$	$\delta\Omega_{\rm GW}^{(0)} h^2$
1)	10^{-4}	4.5×10^{-1}	6.5×10^{-10}	2.6×10^{-13}	1.5×10^{-9}	1.9×10^{-13}
2)	10^{-3}	4.5×10^{-2}	6.5×10^{-12}	2.6×10^{-14}	1.5×10^{-10}	1.9×10^{-13}
3)	10^{-2}	4.5×10^{-3}	6.5×10^{-14}	2.6×10^{-15}	1.5×10^{-11}	1.9×10^{-13}
4)	10^{-1}	4.5×10^{-4}	6.5×10^{-16}	2.6×10^{-16}	1.5×10^{-12}	1.9×10^{-13}

Table 4.1: Benchmarks showing the strength of GWB and its inhomogeneities in the pure radiation-dominance model of [1] and our eMD model. We take them to saturate the CMB bound in Eq. (4.5) (that is, $\zeta_\chi f_{\rm PT} = 4.5 \times 10^{-5}$). For a scale-invariant spectrum, they are consistent with the constraints from PBH production discussed in section 4.4.2.2, except for benchmark 4, which would require significantly red-tilted spectrum for χ to evade constraints on small scales (high-k).

Note that benchmark 4 in table 4.1 above apparently violates PBH bounds discussed in section 4.4.2.2. However, that analysis assumed approximately scale-invariant ζ_χ up to high-k modes that are relevant for PBH production. This is indeed the case for the minimal model of a light χ with fixed mass during inflation that we have considered. It is however possible that with non-minimal couplings, ζ_χ has a suppressed power at high k so that the PBH bounds are evaded while still having large $\delta_{\rm GW}$ at observable small k modes.

If the power spectrum of χ contains features that are not seen in the CMB, $\zeta_\chi f_{\rm PT} < 4.5 \times 10^{-5}$ is required (see for example [131]). This means that for the same ζ_χ, the fraction $f_{\rm PT}$ must be even smaller. For example, consider a case where the PT sector only makes up about 1% of the final SM+DM density perturbations, i.e. $\zeta_\chi f_{\rm PT} \approx 4.5 \times 10^{-7}$. Consider $\zeta_\chi \sim 10^{-4}$ and $f_{\rm PT} \sim 4.5 \times 10^{-3}$. Then in the radiation-dominance scenario, we get $\Omega^{(0)}_{\rm GW} \sim 6.5 \times 10^{-14}$ and $\delta\Omega^{(0)}_{\rm GW} \sim 2.6 \times 10^{-17}$. In our eMD scenario, on the other hand, $\Omega^{(0)}_{\rm GW} \sim 1.5 \times 10^{-11}$ and $\delta\Omega^{(0)}_{\rm GW} \sim 1.9 \times 10^{-15}$. Comparing this to the first benchmark in table 4.1 makes the advantage of our eMD model even more apparent. Such scenarios with smaller $f_{\rm PT}$ would require longer periods of eMD, and possibly lower $T_{\rm SM}(t_{\rm dec})$ or higher PT temperature. A lower $T_{\rm SM}(t_{\rm dec})$ can be made compatible with our analysis by choosing an appropriate DM model that freezes out below this reheat temperature.

To access the improvement in the detection prospect of anisotropies with the eMD model, let us compare the angular power spectrum of GWB to the corresponding angular sensitivity of experiments. The anisotropies of PT-GWB can be conveniently expressed in the multipole basis analogous to the CMB,

$$\langle \delta\Omega^{(0)}_{\rm GW}(\hat{n}) \delta\Omega^{(0)}_{\rm GW}(\hat{n}') \rangle = \sum_\ell \frac{(2\ell+1)}{4\pi} C_\ell^{\rm GW} P_\ell(\cos\theta)\,, \tag{4.60}$$

where $\hat{n} \cdot \hat{n}' = \cos\theta$ and P_ℓ are the Legendre polynomials. The angular power spectrum $C_\ell^{\rm GW}$ can be related to the amplitude of GW fluctuations as,

$$C_\ell^{\rm GW} = \frac{2}{\pi} \int_0^\infty \frac{dk}{k} \mathcal{P}_{\delta\Omega_{\rm GW}}(k) j_\ell^2[k(\eta_{\rm PT} - \eta_{\rm today})], \tag{4.61}$$

where j_ℓ are spherical Bessel functions and $\mathcal{P}_{\delta\Omega_{\rm GW}}$ is given by

$$\langle \delta\Omega^{(0)}_{\rm GW}(\vec{k})\delta\Omega^{(0)}_{\rm GW}(\vec{k}')\rangle = \delta(\vec{k}+\vec{k}')\frac{(2\pi)^3}{k^3}\mathcal{P}_{\delta\Omega_{\rm GW}}(k). \tag{4.62}$$

For a scale-invariant spectrum, $\mathcal{P}_{\delta\Omega_{\rm GW}}(k)$ is constant. In this case, the integral in Eq. (4.61) can be simplified [105], giving

$$\ell(\ell+1)C_\ell^{\rm GW} \approx 14\mathcal{P}_{\delta\Omega_{\rm GW}} \tag{4.63}$$

$C_\ell^{\rm GW}$ can be directly compared to the noise power spectrum N_ℓ of a given experiment, which sets the lower limit for detectable GWB power spectra as a function of multipole ℓ. Figure 4.5 (b) shows $\ell(\ell+1)N_\ell$ as a function of multipole ℓ for relevant detectors like LISA, BBO, and ultimate-DECIGO, which were computed in ref. [5], and are based on the code of ref. [96]. The design of these space-based detectors gives higher sensitivity to even multipoles, resulting in the zigzag curves in the plot.

Figure 4.5 shows the strength of GWB signals for benchmarks 1 (red), 3 (orange), and 4 (yellow) from table 4.1 in the radiation-dominated (dotted lines) and eMD model (solid lines). Figure 4.5 (a) compares the strength of the GWB monopoles with the projected power-law integrated sensitivities for LISA, BBO, and DECIGO [4]. We have incorporated the shift in peak frequency following discussion in section 4.3.2 and Appendix B.1. Fig. 4.5 (b), on the other hand, illustrates the strength of the anisotropic GWB power spectrum (computed using Eq. (4.63)) in the radiation-dominated and eMD models, against projections of the noise power spectrum for LISA, BBO, and ultimate-DECIGO configurations [5]. As explained before, there is no addi-

tional $f_{\rm PT}$ suppression in the GWB inhomogeneities in the eMD model, and the power spectrum for all the benchmarks lies at the same position $\approx 5\times10^{-25}$ shown as a black line in figure 4.5 (b).

4.6 Discussion

LISA is the most sensitive GW detector already under development, with a baseline sensitivity of $\Omega_{\rm LISA}h^2 \sim 10^{-12}$ [37,92] and a power-law integrated sensitivity of $\Omega^{\rm int}_{\rm LISA}h^2 \sim 10^{-14}$ [4]. Clearly, it would be important to be able to see at least an isotropic GWB signal at LISA in order to motivate development of more futuristic proposed detectors, such as BBO or DECIGO, to measure the anisotropies. We see from figure 4.5 (a) that for larger fractional GWB anisotropies, even the isotropic component can be challenging at LISA for the radiation-domination models, whereas they can be readily detectable in our early-matter-domination (eMD) models.

Once an isotropic GWB is detected, there would be a *guaranteed* anisotropic component to be discovered. In fact we see in figure 4.5 (b) that with our eMD model, it is possible that the first few GWB multipoles might be visible already at LISA, above the instrumental noise anisotropy, for a much larger range of GWB anisotropies. Detection of a highly anisotropic GWB at LISA would make an even stronger case for more sensitive detectors to mine the physics of the isocurvature GWB map with higher multipoles. Figure. 4.5 (b) shows that such high resolution map-making would be possible within our eMD model. Finally, larger GWB signals in the eMD model will be significantly easier to distinguish from the various astrophysical foregrounds [132].

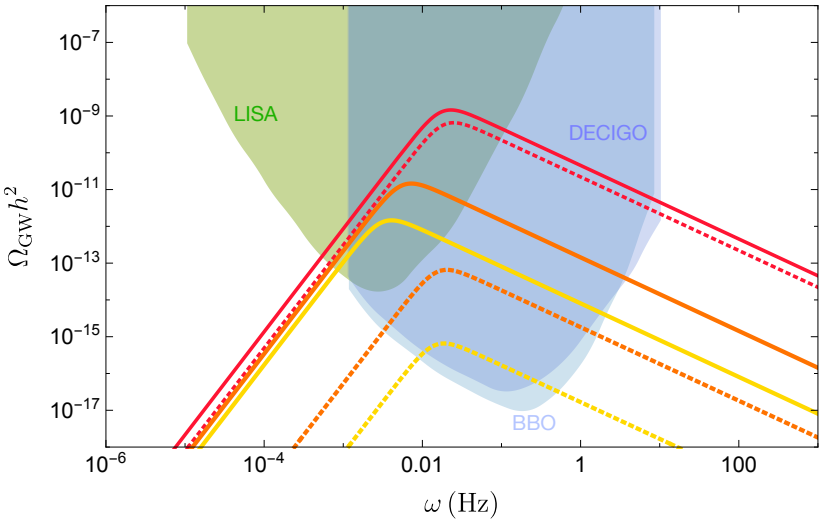

a) Isotropic part

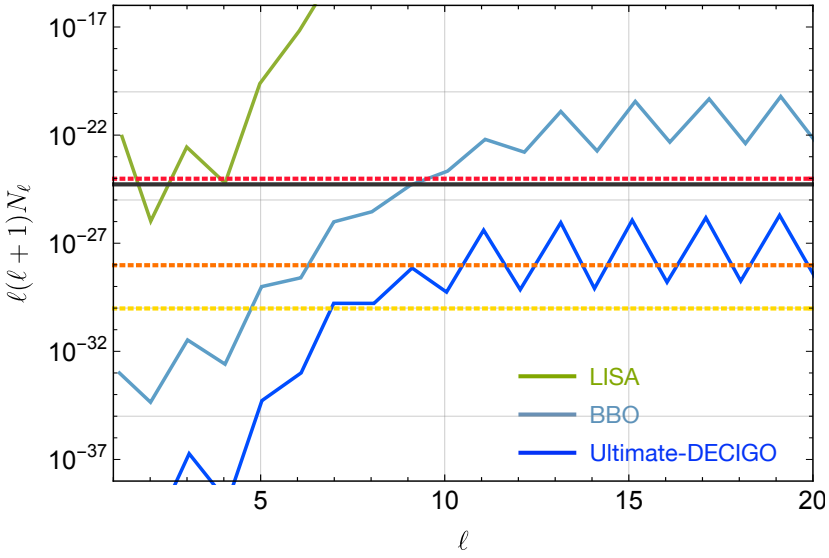

b) Anisotropies

Figure 4.5: Comparison of benchmarks 1 (red), 3 (orange), and 4 (yellow) from table. 4.1 with the (a) sensitivities of upcoming space-based experiments like LISA, BBO, and DECIGO, and (b) noise power spectra N_ℓ as computed in [5]. Solid lines correspond to our modified eMD model while the dotted lines correspond the radiation-dominance scenario of [1]. In (a), the GWB spectra are evaluated for a phase transition occurring at $T_{\rm PT}(t_{\rm PT}) \sim 100$ TeV in a single-sector scenario, and contribution from bubble collisions is taken to be the dominant source of gravitational waves. In (b), all benchmarks for the eMD model lie on the same line at $\approx 5\times10^{-25}$ and are together represented by a black line.

Chapter 5: Conclusion

5.1 Summary and future directions

Cosmological datasets are powerful probes of high energy physics that could be playing out in the early universe. In particular, perturbations in the energy density across space can contain valuable information about processes occurring at extremely high energies during inflation. In this thesis, we have explored several ways through which new inflationary physics can be discovered in cosmological datasets.

In Chapter 2, we describe the program of cosmological collider physics which studies signatures of heavy particles produced during inflation in the non-Gaussainity (NG) of density perturbations. In the vanilla scenario, masses of the particles with observable signatures are restricted to be very close to the inflationary Hubble scale. However, this restriction can be relaxed significantly with the mechanism of chemical potential, and we illustrate this for complex scalar fields. The natural next step is then to generalize this mechanism to particles with higher spins. Similar to the case of scalars, we expect the dominant NG to be at tree-level for particles with integer spins, which would make the analysis more tractable compared to the previous implementations of chemical potential. It is also be important to identify well-motivated candidates whose observability can be improved through chemical potential. Some important targets could be heavy vector fields from grand unified theories and Kaluza-Klein excitations of higher-dimensional

fields.

The second part of the thesis, which included Chapters 3 and 4, explores gravitational wave backgrounds (GWB) from first-order phase transitions as novel datasets of density perturbations. It is shown that GWB could contain new inflationary features that are absent in the current datasets such as the CMB and galaxy distribution. We also show that such GWB could be detectable with upcoming gravitational wave experiments like LISA if the cosmological history includes an earlier period of matter dominance prior to the Big Bang Nucleosynthesis. Apart from phase transitions, there may also be other sources of gravitational waves in the early universe. For example, in our model of early matter dominance in Chapter 4, another (weaker) GWB is sourced by the curvature perturbations at second order. Since gravitational waves start free-streaming right after production, each of these GWBs could be an independent dataset, which creates an exciting possibility of *multiple* GWB density maps. It would be important to estimate the GWB signal strength in each of these cases and study the properties of their fluctuations. Finally, similar to the GWB, we can also look for other possible independent datasets of inflationary fluctuations.

5.2 Final remarks

Precision cosmology has now become an integral part of the particle physics exploration. Conventional experiments such as particle colliders offer more controlled and reproducible environments, however within a limited range of energies and conditions. Our cosmic history, on the other hand, hosts an enormous span of energies and time scales, but it cannot be reproduced and manipulated. In this way, cosmology presents a very complementary approach to the study

of particle physics compared to terrestrial experiments. Each can however influence progress in the other. Observations of terrestrial experiments more often than not have implications for cosmology. In the other direction, cosmological observations can put strong constraints on possible new physics. This can guide designs of future terrestrial experiments, which can be optimised to search in specific parameter spaces with better control. In this way, a synergy of cosmological observations and collider/table-top experiments on Earth would be the best route to discovery.

Appendix A: Appendices to Chapter 2

A.1 Important integrals involving Hankel functions

In this section, we outline the derivation of some of the Hankel integrals that are useful for the calculation of NG. We need to evaluate integrals of the form,

$$\int_0^\infty dx\, x^n e^{\mp ipx}\, e^{\mp \pi\mu} H_{i\mu}^{(1/2)}(x)\ . \tag{A.1}$$

While the expressions for these Hankel integrals can be found for example in [133], the derivation is quite instructive (similar treatment can be found in [20]). We show that it is easily generalised to the imaginary values of n, which is relevant for us. We sketch the derivation for integrals with $H^{(2)}$, while a similar procedure can be used to get integrals involving $H^{(1)}$.

$$I_2(n,p) = \int_0^\infty dx\, x^n e^{ipx} e^{\pi\mu/2} H_{i\mu}^{(2)}(x) = \int_0^\infty dx\, x^{n-3/2} e^{ipx} f(x)\ , \tag{A.2}$$

where $f(x) = e^{\pi\mu/2}\, x^{3/2} H^{(2)}_{i\mu}(x)$ is a solution to the EOM for mode functions as seen in section 2.3.4. Then,

$$\begin{aligned} &\left[\partial_x^2 - \frac{2}{x}\partial_x + (1 + \frac{M^2}{x^2})\right] f(x) = 0 \\ \implies \quad &\int_0^\infty x^{2+n-3/2} e^{ipx} \left[\partial_x^2 - \frac{2}{x}\partial_x + (1 + \frac{M^2}{x^2})\right] f(x) = 0 \, . \end{aligned} \tag{A.3}$$

From here, we can systematically move the integration past the differential operator using integration by parts to get a differential equation for I_2 with respect to variable p. To clarify the point, consider the last term,

$$\begin{aligned} \int_0^\infty x^{2+n-3/2} e^{ipx} \left(1 + \frac{M^2}{x^2}\right) f(x) &= \int_0^\infty x^{2+n} e^{ipx} e^{\pi\mu/2} H^{(2)}_{i\mu}(x) + M^2 \int_0^\infty x^n e^{ipx} e^{\pi\mu/2} H^{(2)}_{i\mu}(x) \\ &= (-\partial_p^2 + M^2) I_2(n,p) \, . \end{aligned} \tag{A.4}$$

Similarly for the derivative terms, we integrate by parts. For example, the second term can be written as,

$$\begin{aligned} &\int_0^\infty x^{2+n-3/2} e^{ipx} \left(-\frac{2}{x}\partial_x\right) f(x) \\ =& -2 \left\{ \int \partial_x \left(x^{1+n-3/2} e^{ipx} f(x)\right) - \partial_x \left(x^{1+n-3/2} e^{ipx}\right) f(x) \right\} \, . \end{aligned} \tag{A.5}$$

The first term is the boundary term which can be dropped. Then we are left with,

$$\int_0^\infty x^{2+n-3/2} e^{ipx} \left(-\frac{2}{x}\partial_x\right) f(x) = \left[2(n-1/2) + 2ip(-i\partial_p)\right] I_2(n,p) \, . \tag{A.6}$$

Following this procedure, we get a differential equation for $I_2(n,p)$ as,

$$\left((p^2-1)\partial_p^2 + 2p\left(n+\frac{3}{2}\right)\partial_p + \left[M^2 + \left(n-\frac{1}{2}\right)\left(n+\frac{5}{2}\right)\right]\right)\ I_2(n,p) = 0\ . \tag{A.7}$$

We want the solution to be regular at $p=1$. This implies,

$$I_2(n,p) \propto\ {}_2F_1\left(n+1+i\mu, n+1-i\mu, n+3/2; \frac{(1-p)}{2}\right)\ . \tag{A.8}$$

The normalization is fixed by explicitly carrying out the integration in large p limit using small x expansion of the Hankel function, and then matching it to the large p expansion of hypergeometric function. We also note that this derivation holds even if n has an imaginary part.

In summary:

$$\begin{aligned} I_1(n,p) &= e^{-\pi\mu/2}\int_0^\infty dx\, x^n e^{+ipx} H^{(1)}_{i\mu}(x) \\ &= \frac{(i/2)^n}{\sqrt{\pi}\,\Gamma(n+3/2)}\Gamma(n+1+i\mu)\Gamma(n+1-i\mu)\ \times \\ &\qquad {}_2F_1(n+1-i\mu, n+1+i\mu, n+3/2, (1-p)/2)\ , \end{aligned} \tag{A.9}$$

$$\begin{aligned} I_2(n,p) &= e^{\pi\mu/2}\int_0^\infty dx\, x^n e^{-ipx} H^{(2)}_{i\mu}(x) \\ &= \frac{(-i/2)^n}{\sqrt{\pi}\,\Gamma(n+3/2)}\Gamma(n+1+i\mu)\Gamma(n+1-i\mu)\ \times \\ &\qquad {}_2F_1(n+1+i\mu, n+1-i\mu, n+3/2, (1-p)/2)\ . \end{aligned} \tag{A.10}$$

A.2 Full calculation of the bispectrum

Our interaction Hamiltonian of the following form,

$$\mathcal{H}_{\rm mix} \,=\, \sqrt{-g}\,(-\eta)^{i\lambda}\,\Big(\,\beta_1\,(\dot{\delta\phi})\,\tilde{\sigma}\,+\,\beta_2\,\delta\phi\,\tilde{\sigma}\,\Big)\,+\,\text{c.c.}\quad\text{and} \tag{A.11}$$

$$\mathcal{H}_3 \,=\, \sqrt{-g}\,(-\eta)^{i\lambda}\,\left(\,\rho_1\,(\partial\delta\phi)^2\,\tilde{\sigma}\,+\,\rho_2\,\delta\phi\,\delta\phi\,\tilde{\sigma}\,\right)\,+\,\text{c.c.}. \tag{A.12}$$

A.2.1 Full analytic calculation of $I_{+-/-+}$ diagrams

$$I_{+-}\sim\langle\,0|\int\mathcal{H}_{\rm mix}\;\;\delta\phi_0^3\int\mathcal{H}_3\,|0\,\rangle. \tag{A.13}$$

There are in all 8 different sub-diagrams contributing to I_{+-}: 2 different vertices in both $\mathcal{H}_{\rm mix}$ and $\mathcal{H}_{\rm int}$, and two possible contractions of the complex scalar, $\langle\,\tilde{\sigma}\tilde{\sigma}^\dagger\,\rangle$ and $\langle\,\tilde{\sigma}^\dagger\tilde{\sigma}\,\rangle$. The contribution from $\langle\,\tilde{\sigma}\tilde{\sigma}^\dagger\,\rangle$ sub-diagrams are related to those with $\langle\,\tilde{\sigma}^\dagger\tilde{\sigma}\,\rangle$ by a replacement $\lambda\to-\lambda$. Thus, it is enough to evaluate terms with contraction $\langle\,\tilde{\sigma}^\dagger\tilde{\sigma}\,\rangle$ explicitly.

$$\begin{aligned} I_{+-}\,\supset\,\int_{-\infty}^{0}\,\frac{d\eta_1}{\eta_1^4}\,\frac{d\eta_2}{\eta_2^4}\,\langle\,(\beta_1^*(\dot{\delta\phi})+\beta_2^*\delta\phi)\,\tilde{\sigma}^\dagger\,(-\eta_1)^{-i\lambda} \\ \times\;\delta\phi_0\delta\phi_0\delta\phi_0\;\times\;(\rho_1(\partial\delta\phi)^2+\rho_2(\delta\phi)^2)\,\tilde{\sigma}\,(-\eta_2)^{i\lambda}\,\rangle. \end{aligned} \tag{A.14}$$

Using

$$\langle\, (\dot{\delta\phi})(\eta,\vec{k})\delta\phi(\eta\to 0,-\vec{k})\,\rangle = -\frac{\eta^2 k^2}{2k^3}\, e^{-ik\eta}$$
$$\text{and} \qquad \langle\, \delta\phi(\eta,\vec{k})\delta\phi(\eta\to 0,-\vec{k})\,\rangle = \frac{(1+ik\eta)e^{-ik\eta}}{2k^3}, \tag{A.15}$$

we can write the anti-time ordered contribution at k_3 vertex (up to pure phase) as,

$$\begin{aligned} I^{(-)}_{k_3} &= (+i)\int_{-\infty}^{0}\frac{d\eta}{\eta^4}\left(-\beta_1^*\frac{\eta^2k_3^2\,e^{-ik_3\eta}}{2k_3^3}+\beta_2^*\frac{(1+ik_3\eta)e^{-ik_3\eta}}{2k_3^3}\right)(-\eta)^{-i\lambda} \\ &\qquad\qquad \times\underbrace{\left(N_f^*(-\eta)^{3/2}H^{(1)}_{i\mu}(-k_3\eta)\right)}_{\bar{f}_{k_3}(\eta)} \\ &= \frac{i\sqrt{\pi}}{4}\frac{1}{k_3^{3/2-i\lambda}}\left[-\beta_1^*I_1\left(-\frac{1}{2}-i\lambda,1\right)\right. \\ &\qquad\qquad \left.+\beta_2^*\left\{I_1\left(-\frac{5}{2}-i\lambda,1\right)-iI_1\left(-\frac{3}{2}-i\lambda,1\right)\right\}\right]. \end{aligned} \tag{A.16}$$

Similarly, we calculate time ordered contribution from k_{12} vertex as,

$$\begin{aligned} I^{(+)}_{k_{12}} &= \frac{-i}{4k_1^3k_2^3}\int_{-\infty}^{0}\frac{d\eta}{\eta^4}\left(\rho_1\eta^2\mathcal{D}_{12}+\rho_2(1-ik_1\eta)(1-ik_2\eta)\right)e^{ik_{12}\eta}(-\eta)^{+i\lambda} \\ &\qquad\qquad \times\underbrace{\left(N_f(-\eta)^{3/2}H^{(2)}_{i\mu}(-k_3\eta)\right)}_{f_{k_3}(\eta)} \\ &= \frac{-i\sqrt{\pi}}{8k_1^3k_2^3k_3^{1/2+i\lambda}}\left[\rho_1\mathcal{D}_{12}I_2\left(-\frac{1}{2}+i\lambda,p\right)+\rho_2k_3^2\left\{I_2\left(-\frac{5}{2}+i\lambda,p\right)\right.\right. \\ &\qquad\qquad \left.\left.+ipI_2\left(-\frac{3}{2}+i\lambda,p\right)-\frac{p^2}{4}I_2\left(-\frac{1}{2}+i\lambda,p\right)\right\}\right]. \end{aligned} \tag{A.17}$$

where the operator $\mathcal{D}_{12}$ is,

$$\mathcal{D}_{12} = k_1^2 k_2^2 \partial_{k_{12}}^2 + (-\vec{k}_1 \cdot \vec{k}_2)(1 - k_{12}\partial_{k_{12}} + k_1 k_2 \partial_{k_{12}}^2). \tag{A.18}$$

It can be simplified in the squeezed limit as,

$$\mathcal{D}_{12} k_{12}^{\alpha} = \frac{1}{8}(\alpha - 1)(\alpha - 2)\, k_{12}^{\alpha+2}. \tag{A.19}$$

We can now put together the full form of $I_{+-/-+}$ diagrams,

$$I_{+-} + I_{-+} = 2 \times \Big\{ I_{k_3}^{(-)}(\lambda, \beta_i^*) \times I_{k_{12}}^{(+)}(\lambda, \rho_i) + ((\lambda, \beta_i^*, \rho_i) \to (-\lambda, \beta_i, \rho_i^*)) \Big\} + \text{c.c.}\,, \tag{A.20}$$

where the integrals at k_3 and k_{12} vertices are evaluated in eqs. (A.16) and (A.17), and we have accounted for the symmetry factor.

A.2.2 Full analytic calculation of $I_{++/--}$ diagrams

As discussed in section 2.4.4, the integrals at k_3 gets contribution from earlier time which is well separated from the time period that contributes to the integral at k_{12}. This takes care of the time-ordering and lets us expand the range of integration to the entire domain.

$$\begin{aligned} I_{++} \supset \langle\, \delta\phi_0 \delta\phi_0 \delta\phi_0 \cdot \int_{-\infty}^{0} \frac{d\eta_2}{\eta_2^4} (\rho_1^* (\partial\delta\phi)^2 + \rho_2^* (\delta\phi)^2)\, \tilde{\sigma}^{\dagger}\, (-\eta_2)^{-i\lambda} \\ \times \int_{-\infty}^{0} \frac{d\eta_1}{\eta_1^4} (\beta_1 (\dot{\delta\phi}) + \beta_2 \delta\phi)\, \tilde{\sigma}\, (-\eta_1)^{i\lambda}\, \rangle. \end{aligned} \tag{A.21}$$

A closer look reveals that $I^{(+)}_{k_3}$ can be obtained by replacing $I_1 \to I_2$ and $\lambda \to -\lambda$ with an appropriate change in sign in a few places in Eq. (A.16).

$$I^{(+)}_{k_3} = \frac{-i\sqrt{\pi}}{4}\frac{1}{k_3^{3/2+i\lambda}}\left[-\beta_1 I_2\left(-\frac{1}{2}+i\lambda,1\right)\right.$$
$$\left.+\beta_2\left\{I_2\left(-\frac{5}{2}+i\lambda,1\right)+iI_2\left(-\frac{3}{2}+i\lambda,1\right)\right\}\right]. \tag{A.22}$$

Similarly, $I^{(+)}_{k_{12}}$ follows from Eq. (A.17) with the replacements $I_2 \to I_1$, $p \to -p$, $\lambda \to -\lambda$, and appropriate sign changes.

$$I^{(+)}_{k_{12}} = \frac{-i\sqrt{\pi}}{8k_1^3k_2^3k_3^{1/2-i\lambda}}\left[\rho_1^*\mathcal{D}_{12}I_1\left(-\frac{1}{2}-i\lambda,-p\right)+\rho_2^*k_3^2\left\{I_1\left(-\frac{5}{2}-i\lambda,-p\right)\right.\right.$$
$$\left.\left.+ipI_1\left(-\frac{3}{2}-i\lambda,-p\right)-\frac{p^2}{4}I_1\left(-\frac{1}{2}-i\lambda,-p\right)\right\}\right]. \tag{A.23}$$

Then the contribution from $I_{++/--}$ diagrams is

$$I_{++}+I_{--} = 2\times\left\{I^{(+)}_{k_3}(\lambda,\beta_i)\times I^{(+)}_{k_{12}}(\lambda,\rho_i^*)+((\lambda,\beta_i,\rho_i^*)\to(-\lambda,\beta_i^*,\rho_i))\right\}+\text{c.c.}, \tag{A.24}$$

where now we use expression in eqs. (A.22) and (A.23).

Appendix B: Appendix to Chapter 4

B.1 $f_{\rm PT}^2$ suppression in $\Omega_{\rm GW}$ in the radiation-dominated model

A first-order phase transition proceeds through the formation and expansion of bubbles of true vacuum. The rate of bubble formation per unit volume Γ can be given by

$$\Gamma \sim T_{\rm PT}^4 e^{-S(T_{\rm PT})}, \tag{B.1}$$

where $T_{\rm PT}$ is the temperature of the PT sector and $S(T_{\rm PT})$ is the Euclidean action of a critical bubble. The transition begins when the rate of bubble formation is comparable to the Hubble rate, $\Gamma \sim H^4$. Now, in the radiation-dominated model described in section 4.2, the Hubble rate can be written in terms of $T_{\rm PT}$ as

$$H^2 \sim \frac{\rho_{\rm total}}{M_{\rm Pl}^2} \sim \frac{f_{\rm PT}^{-1} T_{\rm PT}^4}{M_{\rm Pl}^2}. \tag{B.2}$$

Then the phase transition begins at temperature $T_* \equiv T_{\rm PT}(t_{\rm PT})$ such that

$$\begin{aligned} T_*^4 e^{-S(T_*)} &\sim \frac{f_{\rm PT}^{-2} T_*^8}{M_{\rm Pl}^4} \\ \implies \quad -S(T_*) &\sim 4 \log\left(\frac{T_*}{M_{\rm Pl}}\right) - 2\log\left(f_{\rm PT}\right). \end{aligned} \tag{B.3}$$

Since gravitational wave production in a single sector ($f_{\rm PT} = 1$) is well understood, we compare the multi-sector case of $f_{\rm PT} < 1$ with the single-sector case of $f_{\rm PT} = 1$. For this, we henceforth use '$^-$' to denote quantities corresponding to a single-sector system. Then $-S(\overline{T}_*) \sim 4\log\left(\frac{\overline{T}_*}{M_{\rm Pl}}\right)$. Now, let us expand $T_* = \overline{T}_* + \Delta T$. Then Eq. (B.3) gives

$$-\left(\overline{\tilde{\beta}}\,\frac{\Delta T}{\overline{T}_*} + \left(\left.\frac{d\tilde{\beta}}{d\log T}\right|_{\overline{T}_*} - \overline{\tilde{\beta}}\right)\left(\frac{\Delta T}{\overline{T}_*}\right)^2\right) \sim 4\log\left(1+\frac{\Delta T}{\overline{T}_*}\right) - 2\log f_{\rm PT}. \tag{B.4}$$

where,

$$\tilde{\beta} \equiv \left.\frac{\beta}{H}\right|_{t_{\rm PT}} = \left.\frac{dS}{d\log T}\right|_{T_*}. \tag{B.5}$$

$\tilde{\beta}$ is an important PT parameter as it determines the typical length/time scale of the bubble dynamics (and hence the typical frequency of gravitational waves at production) relative to H^{-1}. From Eq. (B.4), we see that the temperature shift depends on $\overline{\tilde{\beta}}$. Therefore, let us consider two cases:

1) **Typical $\overline{\tilde{\beta}} \sim \mathcal{O}(100)$:** For a TeV scale phase transition, the typical value of $\overline{\tilde{\beta}} \sim S(\overline{T}_*) \sim \mathcal{O}(100)$. In this case, the change in the PT temperature is small and Eq. (B.4) simplifies to

$$\frac{\Delta T}{\overline{T}_*} \approx \frac{2\log f_{\rm PT}}{\overline{\tilde{\beta}}+4}. \tag{B.6}$$

For the smallest $f_{\rm PT} \sim 10^{-5}$ of interest, we get $(\Delta T/\overline{T}_*) \sim -0.1$. Now, the going rate for the change in $\tilde{\beta}$ is also expected to be set by the action, i.e. $(d\tilde{\beta}/d\log T)|_{\overline{T}_*} \sim S(\overline{T}_*) \sim \mathcal{O}(100)$. So the expected change in $\tilde{\beta}$ due to the shift in the PT temperature is $\Delta\tilde{\beta} \sim 10 \ll \overline{\tilde{\beta}}$. Thus, we can

take

$$\tilde{\beta} \approx \overline{\tilde{\beta}}. \tag{B.7}$$

2) **"Tuned"** $\overline{\tilde{\beta}} \sim \mathcal{O}(\mathbf{10})$: From the observational perspective, gravitational waves from phase transitions with smaller $\tilde{\beta}$ are more likely to be observed first. Thus we have considered $\overline{\tilde{\beta}} = 10$ in this work. This requires tuning of parameters such that the rate of change of the action is an order of magnitude smaller than the action itself at $\overline{T}_*$. Despite the tuning in $\overline{\tilde{\beta}}$, we still expect $(d\tilde{\beta}/d\log T)|_{\overline{T}_*} \sim \mathcal{O}(100)$. In other words, a shift in the PT temperature due to $f_{\rm PT} < 1$ is likely to take the system away from the tuned point to a more typical value of $\tilde{\beta} \sim \mathcal{O}(100)$. Taking $f_{\rm PT} \sim 10^{-5}$ in Eq. (B.4) gives $(\Delta T/\overline{T}_*) \sim -0.4$ and $\Delta\tilde{\beta} \sim 40$. Now a larger $\tilde{\beta}$ will lead to an additional suppression in the GW signal on top of the expected $f_{\rm PT}^2$. This can be seen through the $\tilde{\beta}^{-2}$ dependence in Eq. (4.8). However, since the exact shift in $\tilde{\beta}$ is model dependent, we make a conservative choice of neglecting change $\tilde{\beta}$ and follow Eq. (B.7) even in the case of relatively small $\tilde{\beta}$. Note that correctly including the suppression due to larger $\tilde{\beta}$ will only strengthen the case for our eMD model described in section 4.3.

Let us now look at the gravitational wave emission, which is governed by the transverse traceless part of the linearized Einstein equations

$$\Box h_{\rm GW} \sim \frac{\mathcal{T}(x)}{M_{\rm Pl}^2}\,, \tag{B.8}$$

where $\Box \equiv (\partial_t^2 + 3H\partial_t - a^{-2}\nabla^2)$ and $\mathcal{T}$ is the transverse traceless part of the stress-energy

tensor of the PT sector. It is useful to change to dimensionless coordinates $\tilde{x} = Hx$ and the stress tensor $\tilde{\mathcal{T}} = \rho_{\rm PT}^{-1}\mathcal{T}$ [1] where $\tilde{\mathcal{T}}$ captures the dimensionless "shape" of the dominant quadrupole GW sources. Then

$$\widetilde{\Box} h_{\rm GW} \sim \frac{\rho_{\rm PT}\tilde{\mathcal{T}}(\tilde{x})}{H^2 M_{\rm Pl}^2} \sim f_{\rm PT}\tilde{\mathcal{T}}(\tilde{x})\,. \tag{B.9}$$

For the familiar case of $f_{\rm PT} = 1$, all the length/time scales of the dominant GW sources are set by β [**?**, 134, 135]. This means that the piece of $\tilde{\mathcal{T}}$ that is relevant for GW production is only parametrized by the dimensionless $\tilde{\beta}$. Given Eq. (B.7), we then have

$$\tilde{\mathcal{T}}(\tilde{x}) \simeq \overline{\tilde{\mathcal{T}}}(\tilde{x})\,. \tag{B.10}$$

Thus, Eq. (B.9) can be written as

$$\widetilde{\Box} h_{\rm GW} \sim f_{\rm PT}\overline{\tilde{\mathcal{T}}}(\tilde{x})\,, \tag{B.11}$$

giving

$$h_{\rm GW}(\tilde{x}) \simeq f_{\rm PT}\overline{h}_{\rm GW}(\tilde{x}) \tag{B.12}$$

[1] since we have taken $\alpha_{\rm PT} \approx 1$

Now,

$$\begin{aligned}\Omega_{\rm GW} \equiv \frac{\rho_{\rm GW}}{\rho_{\rm total}} &\sim \frac{M_{\rm Pl}^2 (\partial h_{\rm GW})^2}{H^2 M_{\rm Pl}^2} \\ &\sim (\tilde{\partial}\, h_{\rm GW})^2 \sim f_{\rm PT}^2 \left(\tilde{\partial}\, \overline{h}_{\rm GW}\right)^2 \\ \implies \Omega_{\rm GW} &\approx f_{\rm PT}^2 \overline{\Omega}_{\rm GW}\,, \end{aligned} \tag{B.13}$$

where we have used Eq. (B.12) in the second line.

The reader may wonder if the GW production from MHD turbulence shows different dependence on $f_{\rm PT}$ as the turbulence may cascade to smaller scales than β^{-1}. However, analytic calculations suggest that the dominant MHD contribution is still in frequencies $\sim \beta$ [134]. Thus, we expect the above analysis to hold also for MHD turbulence. The turbulence contribution is therefore expected to remain subdominant compared to the acoustic and bubble wall collision contributions even in the case $f_{\rm PT} < 1$.

Bibliography

[1] Michael Geller, Anson Hook, Raman Sundrum, and Yuhsin Tsai. Primordial Anisotropies in the Gravitational Wave Background from Cosmological Phase Transitions. *Phys. Rev. Lett.*, 121(20):201303, 2018, 1803.10780.

[2] Bernard Carr, Kazunori Kohri, Yuuiti Sendouda, and Jun'ichi Yokoyama. Constraints on primordial black holes. *Reports on Progress in Physics*, 84(11):116902, 2021.

[3] Bernard Carr and Florian Kühnel. Primordial black holes as dark matter candidates. *SciPost Physics Lecture Notes*, page 048, 2022.

[4] Kai Schmitz. New Sensitivity Curves for Gravitational-Wave Signals from Cosmological Phase Transitions. *JHEP*, 01:097, 2021, 2002.04615.

[5] Matteo Braglia and Sachiko Kuroyanagi. Probing prerecombination physics by the cross-correlation of stochastic gravitational waves and CMB anisotropies. *Phys. Rev. D*, 104(12):123547, 2021, 2106.03786.

[6] Daniel Baumann. TASI lectures on inflation. 2009, 0907.5424.

[7] Y. Akrami et al. Planck 2018 results. X. Constraints on inflation. *Astron. Astrophys.*, 641:A10, 2020, 1807.06211.

[8] Juan Martin Maldacena. Non-Gaussian features of primordial fluctuations in single field inflationary models. *JHEP*, 05:013, 2003, astro-ph/0210603.

[9] Karim A. Malik and David Wands. Cosmological perturbations. *Phys. Rept.*, 475:1–51, 2009, 0809.4944.

[10] Steven Weinberg. Quantum contributions to cosmological correlations. *Phys. Rev.*, D72:043514, 2005, hep-th/0506236.

[11] Xingang Chen, Mohammad Hossein Namjoo, and Yi Wang. Models of the Primordial Standard Clock. *JCAP*, 02:027, 2015, 1411.2349.

[12] Xingang Chen, Reza Ebadi, and Soubhik Kumar. Classical cosmological collider physics and primordial features. *arXiv preprint arXiv:2205.01107*, 2022.

[13] Marcelo Alvarez et al. Testing Inflation with Large Scale Structure: Connecting Hopes with Reality. 12 2014, 1412.4671.

[14] Licia Verde. Non-Gaussianity from Large-Scale Structure Surveys. *Advances in Astronomy*, 2010:768675, January 2010, 1001.5217.

[15] Abraham Loeb and Matias Zaldarriaga. Measuring the small - scale power spectrum of cosmic density fluctuations through 21 cm tomography prior to the epoch of structure formation. *Phys. Rev. Lett.*, 92:211301, 2004, astro-ph/0312134.

[16] Julian B. Muñoz, Yacine Ali-Haïmoud, and Marc Kamionkowski. Primordial non-gaussianity from the bispectrum of 21-cm fluctuations in the dark ages. *Phys. Rev. D*, 92(8):083508, 2015, 1506.04152.

[17] N.D. Birrell and P.C.W. Davies. *Quantum Fields in Curved Space*. Cambridge Monographs on Mathematical Physics. Cambridge Univ. Press, Cambridge, UK, 2 1984.

[18] Xingang Chen and Yi Wang. Quasi-Single Field Inflation and Non-Gaussianities. *JCAP*, 04:027, 2010, 0911.3380.

[19] Xingang Chen and Yi Wang. Quasi-Single Field Inflation with Large Mass. *JCAP*, 1209:021, 2012, 1205.0160.

[20] Nima Arkani-Hamed and Juan Maldacena. Cosmological Collider Physics. 3 2015, 1503.08043.

[21] W. Daniel Garretson, George B. Field, and Sean M. Carroll. Primordial magnetic fields from pseudo-Goldstone bosons. *Phys. Rev. D*, 46:5346–5351, 1992, hep-ph/9209238.

[22] Neil Barnaby and Marco Peloso. Large Nongaussianity in Axion Inflation. *Phys. Rev. Lett.*, 106:181301, 2011, 1011.1500.

[23] Lian-Tao Wang and Zhong-Zhi Xianyu. In Search of Large Signals at the Cosmological Collider. *JHEP*, 02:044, 2020, 1910.12876.

[24] Lian-Tao Wang and Zhong-Zhi Xianyu. Gauge Boson Signals at the Cosmological Collider. *JHEP*, 11:082, 2020, 2004.02887.

[25] Peter Adshead and Evangelos I. Sfakianakis. Fermion production during and after axion inflation. *JCAP*, 11:021, 2015, 1508.00891.

[26] Xingang Chen, Yi Wang, and Zhong-Zhi Xianyu. Neutrino Signatures in Primordial Non-Gaussianities. *JHEP*, 09:022, 2018, 1805.02656.

[27] Anson Hook, Junwu Huang, and Davide Racco. Searches for other vacua. Part II. A new Higgstory at the cosmological collider. *JHEP*, 01:105, 2020, 1907.10624.

[28] Anson Hook, Junwu Huang, and Davide Racco. Minimal signatures of the Standard Model in non-Gaussianities. *Phys. Rev. D*, 101(2):023519, 2020, 1908.00019.

[29] Xuce Niu, Moinul Hossain Rahat, Karthik Srinivasan, and Wei Xue. Gravitational wave probes of massive gauge bosons at the cosmological collider. *JCAP*, 02:013, 2023, 2211.14331.

[30] Xi Tong and Zhong-Zhi Xianyu. Large spin-2 signals at the cosmological collider. *JHEP*, 10:194, 2022, 2203.06349.

[31] Matteo Braglia, Xingang Chen, and Dhiraj Kumar Hazra. Primordial standard clock models and CMB residual anomalies. *arXiv preprint arXiv:2108.10110*, 2021.

[32] J. Aasi et al. Advanced LIGO. *Class. Quant. Grav.*, 32:074001, 2015, 1411.4547.

[33] F. Acernese et al. Advanced Virgo: a second-generation interferometric gravitational wave detector. *Class. Quant. Grav.*, 32(2):024001, 2015, 1408.3978.

[34] R. N. Manchester. The International Pulsar Timing Array. *Class. Quant. Grav.*, 30:224010, 2013, 1309.7392.

[35] Benjamin P Abbott et al. Exploring the Sensitivity of Next Generation Gravitational Wave Detectors. *Class. Quant. Grav.*, 34(4):044001, 2017, 1607.08697.

[36] M. Punturo et al. The Einstein Telescope: A third-generation gravitational wave observatory. *Class. Quant. Grav.*, 27:194002, 2010.

[37] Pau Amaro-Seoane, Heather Audley, Stanislav Babak, John Baker, Enrico Barausse, Peter Bender, Emanuele Berti, Pierre Binetruy, Michael Born, Daniele Bortoluzzi, et al. Laser Interferometer Space Antenna. *arXiv:1702.00786*, 2017.

[38] Jun Luo et al. TianQin: a space-borne gravitational wave detector. *Class. Quant. Grav.*, 33(3):035010, 2016, 1512.02076.

[39] Wen-Hong Ruan, Zong-Kuan Guo, Rong-Gen Cai, and Yuan-Zhong Zhang. Taiji program: Gravitational-wave sources. *Int. J. Mod. Phys. A*, 35(17):2050075, 2020, 1807.09495.

[40] G. M. Harry, P. Fritschel, D. A. Shaddock, W. Folkner, and E. S. Phinney. Laser interferometry for the Big Bang Observer. *Class. Quant. Grav.*, 23:4887–4894, 2006. [Erratum: Class.Quant.Grav. 23, 7361 (2006)].

[41] Seiji Kawamura et al. The Japanese space gravitational wave antenna: DECIGO. *Class. Quant. Grav.*, 28:094011, 2011.

[42] Gabriella Agazie et al. The NANOGrav 15 yr Data Set: Evidence for a Gravitational-wave Background. *Astrophys. J. Lett.*, 951(1):L8, 2023, 2306.16213.

[43] N. Bartolo, E. Komatsu, Sabino Matarrese, and A. Riotto. Non-Gaussianity from inflation: Theory and observations. *Phys. Rept.*, 402:103–266, 2004, astro-ph/0406398.

[44] Xingang Chen. Primordial Non-Gaussianities from Inflation Models. *Adv. Astron.*, 2010:638979, 2010, 1002.1416.

[45] Paolo Creminelli. On non-Gaussianities in single-field inflation. *JCAP*, 0310:003, 2003, astro-ph/0306122.

[46] Peter Adshead, Lauren Pearce, Marco Peloso, Michael A. Roberts, and Lorenzo Sorbo. Phenomenology of fermion production during axion inflation. *JCAP*, 06:020, 2018, 1803.04501.

[47] Azadeh Moradinezhad Dizgah and Cora Dvorkin. Scale-Dependent Galaxy Bias from Massive Particles with Spin during Inflation. *JCAP*, 1801(01):010, 2018, 1708.06473.

[48] Azadeh Moradinezhad Dizgah, Hayden Lee, Julian B. Muñoz, and Cora Dvorkin. Galaxy Bispectrum from Massive Spinning Particles. *JCAP*, 1805(05):013, 2018, 1801.07265.

[49] Kazuhiro Kogai, Kazuyuki Akitsu, Fabian Schmidt, and Yuko Urakawa. Galaxy imaging surveys as spin-sensitive detector for cosmological colliders. *JCAP*, 03:060, 2021, 2009.05517.

[50] P. Daniel Meerburg, Moritz Munchmeyer, Julian B. Muñoz, and Xingang Chen. Prospects for Cosmological Collider Physics. *JCAP*, 1703(03):050, 2017, 1610.06559.

[51] Raphael Flauger, Mehrdad Mirbabayi, Leonardo Senatore, and Eva Silverstein. Productive Interactions: heavy particles and non-Gaussianity. *JCAP*, 10:058, 2017, 1606.00513.

[52] Y Akrami, F Arroja, Mark Ashdown, J Aumont, C Baccigalupi, M Ballardini, AJ Banday, RB Barreiro, N Bartolo, S Basak, et al. Planck 2018 results-IX. constraints on primordial non-gaussianity. *Astronomy & Astrophysics*, 641:A9, 2020.

[53] Steven Weinberg. Quantum contributions to cosmological correlations. *Phys. Rev. D*, 72:043514, Aug 2005.

[54] Mikko Laine and Aleksi Vuorinen. *Basics of Thermal Field Theory: A Tutorial on Perturbative Computations*. Lecture Notes in Physics. Springer International Publishing AG, Switzerland, 2016.

[55] Yi Wang. Inflation, Cosmic Perturbations and Non-Gaussianities. *Commun. Theor. Phys.*, 62:109–166, 2014, 1303.1523.

[56] Lev Kofman, Andrei D. Linde, and Alexei A. Starobinsky. Towards the theory of reheating after inflation. *Phys. Rev. D*, 56:3258–3295, 1997, hep-ph/9704452.

[57] Nico M Temme. Large parameter cases of the gauss hypergeometric function. *Journal of computational and applied mathematics*, 153(1-2):441–462, 2003.

[58] Kari Enqvist and Martin S. Sloth. Adiabatic CMB perturbations in pre - big bang string cosmology. *Nucl. Phys. B*, 626:395–409, 2002, hep-ph/0109214.

[59] David H. Lyth and David Wands. Generating the curvature perturbation without an inflaton. *Phys. Lett. B*, 524:5–14, 2002, hep-ph/0110002.

[60] Takeo Moroi and Tomo Takahashi. Effects of cosmological moduli fields on cosmic microwave background. *Phys. Lett. B*, 522:215–221, 2001, hep-ph/0110096. [Erratum: Phys.Lett.B 539, 303–303 (2002)].

[61] Joseph Silk. Cosmic black-body radiation and galaxy formation. *The Astrophysical Journal*, 151:459, 1968.

[62] Wayne Hu and Naoshi Sugiyama. Small-scale cosmological perturbations: an analytic approach. *The Astrophysical Journal*, 471(2):542, 1996.

[63] Mahiro Abe et al. Matter-wave Atomic Gradiometer Interferometric Sensor (MAGIS-100). *Quantum Sci. Technol.*, 6(4):044003, 2021, 2104.02835.

[64] N. Bartolo, D. Bertacca, S. Matarrese, M. Peloso, A. Ricciardone, A. Riotto, and G. Tasinato. Anisotropies and non-Gaussianity of the Cosmological Gravitational Wave Background. *Phys. Rev. D*, 100(12):121501, 2019, 1908.00527.

[65] Nicola Bartolo, Daniele Bertacca, Sabino Matarrese, Marco Peloso, Angelo Ricciardone, Antonio Riotto, and Gianmassimo Tasinato. Characterizing the cosmological gravitational wave background: Anisotropies and non-Gaussianity. *Phys. Rev. D*, 102(2):023527, 2020, 1912.09433.

[66] L. Valbusa Dall'Armi, A. Ricciardone, Nicola Bartolo, D. Bertacca, and S. Matarrese. Imprint of relativistic particles on the anisotropies of the stochastic gravitational-wave background. *Phys. Rev. D*, 103(2):023522, 2021, 2007.01215.

[67] Soubhik Kumar, Raman Sundrum, and Yuhsin Tsai. Non-Gaussian stochastic gravitational waves from phase transitions. *JHEP*, 11:107, 2021, 2102.05665.

[68] Xingang Chen. Primordial Features as Evidence for Inflation. *JCAP*, 01:038, 2012, 1104.1323.

[69] Arushi Bodas, Soubhik Kumar, and Raman Sundrum. The Scalar Chemical Potential in Cosmological Collider Physics. *JHEP*, 02:079, 2021, 2010.04727.

[70] Xi Tong and Zhong-Zhi Xianyu. Large spin-2 signals at the cosmological collider. *arXiv preprint arXiv:2203.06349*, 2022.

[71] Soubhik Kumar and Raman Sundrum. Cosmological Collider Physics and the Curvaton. *JHEP*, 04:077, 2020, 1908.11378.

[72] Shiyun Lu, Yi Wang, and Zhong-Zhi Xianyu. A Cosmological Higgs Collider. *JHEP*, 02:011, 2020, 1907.07390.

[73] Wan Zhen Chua, Qianhang Ding, Yi Wang, and Siyi Zhou. Imprints of Schwinger Effect on Primordial Spectra. *JHEP*, 04:066, 2019, 1810.09815.

[74] Xi Tong, Yi Wang, and Siyi Zhou. Unsuppressed primordial standard clocks in warm quasi-single field inflation. *JCAP*, 06:013, 2018, 1801.05688.

[75] Xingang Chen and Mohammad Hossein Namjoo. Standard Clock in Primordial Density Perturbations and Cosmic Microwave Background. *Phys. Lett. B*, 739:285–292, 2014, 1404.1536.

[76] Xingang Chen, Cora Dvorkin, Zhiqi Huang, Mohammad Hossein Namjoo, and Licia Verde. The Future of Primordial Features with Large-Scale Structure Surveys. *JCAP*, 11:014, 2016, 1605.09365.

[77] Xingang Chen, P. Daniel Meerburg, and Moritz Münchmeyer. The Future of Primordial Features with 21 cm Tomography. *JCAP*, 09:023, 2016, 1605.09364.

[78] Neil J. Cornish. Mapping the gravitational wave background. *Class. Quant. Grav.*, 18:4277–4292, 2001, astro-ph/0105374.

[79] C. Cutler and J. Harms. BBO and the neutron-star-binary subtraction problem. *Phys. Rev. D*, 73:042001, 2006, gr-qc/0511092.

[80] Vincent Corbin and Neil J. Cornish. Detecting the cosmic gravitational wave background with the Big Bang Observer. *Class. Quant. Grav.*, 23:2435–2446, 2006, gr-qc/0512039.

[81] Hideaki Kudoh, Atsushi Taruya, Takashi Hiramatsu, and Yoshiaki Himemoto. Detecting a gravitational-wave background with next-generation space interferometers. *Phys. Rev. D*, 73:064006, 2006, gr-qc/0511145.

[82] Carlo R. Contaldi, Mauro Pieroni, Arianna I. Renzini, Giulia Cusin, Nikos Karnesis, Marco Peloso, Angelo Ricciardone, and Gianmassimo Tasinato. Maximum likelihood map-making with the Laser Interferometer Space Antenna. *Phys. Rev. D*, 102(4):043502, 2020, 2006.03313.

[83] Sylvia Biscoveanu, Colm Talbot, Eric Thrane, and Rory Smith. Measuring the primordial gravitational-wave background in the presence of astrophysical foregrounds. *Phys. Rev. Lett.*, 125:241101, 2020, 2009.04418.

[84] Sharan Banagiri, Alexander Criswell, Tommy Kuan, Vuk Mandic, Joseph D. Romano, and Stephen R. Taylor. Mapping the gravitational-wave sky with LISA: a Bayesian spherical harmonic approach. *Mon. Not. Roy. Astron. Soc.*, 507(4):5451–5462, 2021, 2103.00826.

[85] John Baker, Tessa Baker, Carmelita Carbone, Giuseppe Congedo, Carlo Contaldi, Irina Dvorkin, Jonathan Gair, Zoltan Haiman, David F Mota, Arianna Renzini, et al. High angular resolution gravitational wave astronomy. *Experimental Astronomy*, 51(3):1441–1470, 2021.

[86] Arianna I. Renzini, Boris Goncharov, Alexander C. Jenkins, and Pat M. Meyers. Stochastic Gravitational-Wave Backgrounds: Current Detection Efforts and Future Prospects. *Galaxies*, 10(1):34, 2022, 2202.00178.

[87] Nicola Bartolo, Daniele Bertacca, Robert Caldwell, Carlo R Contaldi, Giulia Cusin, Valerio De Luca, Emanuela Dimastrogiovanni, Matteo Fasiello, Daniel G Figueroa, Gabriele Franciolini, et al. Probing anisotropies of the stochastic gravitational wave background with lisa. *arXiv preprint arXiv:2201.08782*, 2022.

[88] Matteo Braglia, Xingang Chen, and Dhiraj Kumar Hazra. Probing Primordial Features with the Stochastic Gravitational Wave Background. *JCAP*, 03:005, 2021, 2012.05821.

[89] Jacopo Fumagalli, Sébastien Renaux-Petel, and Lukas T. Witkowski. Oscillations in the stochastic gravitational wave background from sharp features and particle production during inflation. *JCAP*, 08:030, 2021, 2012.02761.

[90] Andreas Ringwald. Axions and axion-like particles. *arXiv preprint arXiv:1407.0546*, 2014.

[91] David JE Marsh. Axion cosmology. *Physics Reports*, 643:1–79, 2016.

[92] Chiara Caprini et al. Science with the space-based interferometer eLISA. II: Gravitational waves from cosmological phase transitions. *JCAP*, 04:001, 2016, 1512.06239.

[93] Anupam Mazumdar and Graham White. Review of cosmic phase transitions: their significance and experimental signatures. *Rept. Prog. Phys.*, 82(7):076901, 2019, 1811.01948.

[94] Rainer K Sachs and Arthur M Wolfe. Perturbations of a cosmological model and angular variations of the microwave background. *The Astrophysical Journal*, 147:73, 1967.

[95] Mark Hindmarsh, Stephan J. Huber, Kari Rummukainen, and David J. Weir. Gravitational waves from the sound of a first order phase transition. *Phys. Rev. Lett.*, 112:041301, 2014, 1304.2433.

[96] David Alonso, Carlo R. Contaldi, Giulia Cusin, Pedro G. Ferreira, and Arianna I. Renzini. Noise angular power spectrum of gravitational wave background experiments. *Phys. Rev. D*, 101(12):124048, 2020, 2005.03001.

[97] Andrei D. Linde. Hybrid inflation. *Phys. Rev. D*, 49:748–754, 1994, astro-ph/9307002.

[98] Yi Wang, Yi-Peng Wu, Jun'ichi Yokoyama, and Siyi Zhou. Hybrid Quasi-Single Field Inflation. *JCAP*, 1807(07):068, 2018, 1804.07541.

[99] N. Aghanim et al. Planck 2018 results. VI. Cosmological parameters. *Astron. Astrophys.*, 641:A6, 2020, 1807.06209. [Erratum: Astron.Astrophys. 652, C4 (2021)].

[100] Moritz Breitbach, Joachim Kopp, Eric Madge, Toby Opferkuch, and Pedro Schwaller. Dark, Cold, and Noisy: Constraining Secluded Hidden Sectors with Gravitational Waves. *JCAP*, 07:007, 2019, 1811.11175.

[101] Malcolm Fairbairn, Edward Hardy, and Alastair Wickens. Hearing without seeing: gravitational waves from hot and cold hidden sectors. *JHEP*, 07:044, 2019, 1901.11038.

[102] Mark Hindmarsh, Stephan J. Huber, Kari Rummukainen, and David J. Weir. Shape of the acoustic gravitational wave power spectrum from a first order phase transition. *Phys. Rev. D*, 96(10):103520, 2017, 1704.05871. [Erratum: Phys.Rev.D 101, 089902 (2020)].

[103] Ryusuke Jinno, Thomas Konstandin, Henrique Rubira, and Jorinde van de Vis. Effect of density fluctuations on gravitational wave production in first-order phase transitions. *JCAP*, 12(12):019, 2021, 2108.11947.

[104] Marek Lewicki and Ville Vaskonen. Gravitational waves from colliding vacuum bubbles in gauge theories. *Eur. Phys. J. C*, 81(5):437, 2021, 2012.07826. [Erratum: Eur.Phys.J.C 81, 1077 (2021)].

[105] Scott Dodelson and Fabian Schmidt. *Modern cosmology*. Academic Press, 2020.

[106] Teruaki Suyama and Jun'ichi Yokoyama. Temporal enhancement of super-horizon curvature perturbations from decays of two curvatons and its cosmological consequences. *Phys. Rev. D*, 84:083511, 2011, 1106.5983.

[107] Adrienne L. Erickcek and Kris Sigurdson. Reheating Effects in the Matter Power Spectrum and Implications for Substructure. *Phys. Rev. D*, 84:083503, 2011, 1106.0536.

[108] JiJi Fan, Ogan Özsoy, and Scott Watson. Nonthermal histories and implications for structure formation. *Phys. Rev. D*, 90(4):043536, 2014, 1405.7373.

[109] Abraham Loeb and Matias Zaldarriaga. The Small-scale power spectrum of cold dark matter. *Phys. Rev. D*, 71:103520, 2005, astro-ph/0504112.

[110] Edmund Bertschinger. The Effects of Cold Dark Matter Decoupling and Pair Annihilation on Cosmological Perturbations. *Phys. Rev. D*, 74:063509, 2006, astro-ph/0607319.

[111] Anne M. Green and Bradley J. Kavanagh. Primordial Black Holes as a dark matter candidate. *J. Phys. G*, 48(4):043001, 2021, 2007.10722.

[112] Kenta Ando, Keisuke Inomata, and Masahiro Kawasaki. Primordial black holes and uncertainties in the choice of the window function. *Phys. Rev. D*, 97:103528, May 2018.

[113] Ilia Musco. Threshold for primordial black holes: Dependence on the shape of the cosmological perturbations. *Phys. Rev. D*, 100:123524, Dec 2019.

[114] Matthew W Choptuik. Universality and scaling in gravitational collapse of a massless scalar field. *Physical Review Letters*, 70(1):9, 1993.

[115] J. C. Niemeyer and K. Jedamzik. Near-critical gravitational collapse and the initial mass function of primordial black holes. *Phys. Rev. Lett.*, 80:5481–5484, Jun 1998.

[116] Ilia Musco, John C. Miller, and Alexander G. Polnarev. Primordial black hole formation in the radiative era: Investigation of the critical nature of the collapse. *Class. Quant. Grav.*, 26:235001, 2009, 0811.1452.

[117] M Yu Khlopov and AG Polnarev. Primordial black holes as a cosmological test of grand unification. *Physics Letters B*, 97(3-4):383–387, 1980.

[118] Tomohiro Harada, Chul-Moon Yoo, Kazunori Kohri, Ken-ichi Nakao, and Sanjay Jhingan. Primordial black hole formation in the matter-dominated phase of the Universe. *Astrophys. J.*, 833(1):61, 2016, 1609.01588.

[119] Gerhard Rein, Alan D Rendall, and Jack Schaeffer. Critical collapse of collisionless matter: A numerical investigation. *Physical Review D*, 58(4):044007, 1998.

[120] Carsten Gundlach and Jose M. Martin-Garcia. Critical phenomena in gravitational collapse. *Living Rev. Rel.*, 10:5, 2007, 0711.4620.

[121] Ilia Musco and John C. Miller. Primordial black hole formation in the early universe: critical behaviour and self-similarity. *Class. Quant. Grav.*, 30:145009, 2013, 1201.2379.

[122] Bernard J. Carr. The Primordial black hole mass spectrum. *Astrophys. J.*, 201:1–19, 1975.

[123] Bernard Carr, Martti Raidal, Tommi Tenkanen, Ville Vaskonen, and Hardi Veermäe. Primordial black hole constraints for extended mass functions. *Phys. Rev. D*, 96(2):023514, 2017, 1705.05567.

[124] Guillem Domènech. Scalar Induced Gravitational Waves Review. *Universe*, 7(11):398, 2021, 2109.01398.

[125] Vasilis K. Oikonomou. f(R)$f(R)$-Gravity Generated Post-Inflationary Eras and Their Effect on Primordial Gravitational Waves. *Annalen Phys.*, 534(8):2200134, 2022, 2205.15405.

[126] Kazunori Kohri and Takahiro Terada. Semianalytic calculation of gravitational wave spectrum nonlinearly induced from primordial curvature perturbations. *Phys. Rev. D*, 97(12):123532, 2018, 1804.08577.

[127] Daniel Baumann, Paul J. Steinhardt, Keitaro Takahashi, and Kiyotomo Ichiki. Gravitational Wave Spectrum Induced by Primordial Scalar Perturbations. *Phys. Rev. D*, 76:084019, 2007, hep-th/0703290.

[128] Hooshyar Assadullahi and David Wands. Gravitational waves from an early matter era. *Phys. Rev. D*, 79:083511, 2009, 0901.0989.

[129] Keisuke Inomata, Kazunori Kohri, Tomohiro Nakama, and Takahiro Terada. Enhancement of Gravitational Waves Induced by Scalar Perturbations due to a Sudden Transition from an Early Matter Era to the Radiation Era. *Phys. Rev. D*, 100(4):043532, 2019, 1904.12879.

[130] Keisuke Inomata, Kazunori Kohri, Tomohiro Nakama, and Takahiro Terada. Gravitational Waves Induced by Scalar Perturbations during a Gradual Transition from an Early Matter Era to the Radiation Era. *JCAP*, 10:071, 2019, 1904.12878.

[131] Arushi Bodas and Raman Sundrum. Primordial clocks within stochastic gravitational wave anisotropies. *JCAP*, 10:012, 2022, 2205.04482.

[132] Giulia Cusin, Irina Dvorkin, Cyril Pitrou, and Jean-Philippe Uzan. Stochastic gravitational wave background anisotropies in the mHz band: astrophysical dependencies. *Mon. Not. Roy. Astron. Soc.*, 493(1):L1–L5, 2020, 1904.07757.

[133] Soubhik Kumar and Raman Sundrum. Heavy-Lifting of Gauge Theories By Cosmic Inflation. *JHEP*, 05:011, 2018, 1711.03988.

[134] Chiara Caprini, Ruth Durrer, and Geraldine Servant. The stochastic gravitational wave background from turbulence and magnetic fields generated by a first-order phase transition. *JCAP*, 12:024, 2009, 0909.0622.

[135] Pierre Binetruy, Alejandro Bohe, Chiara Caprini, and Jean-Francois Dufaux. Cosmological Backgrounds of Gravitational Waves and eLISA/NGO: Phase Transitions, Cosmic Strings and Other Sources. *JCAP*, 06:027, 2012, 1201.0983.